Universiteit Leiden
The Netherlands

Biological model representation and analysis

Cao, L.

Citation
Cao, L. (2014, November 20). *Biological model representation and analysis*. Retrieved from https://hdl.handle.net/1887/29754

Version:	Corrected Publisher's Version
License:	Licence agreement concerning inclusion of doctoral thesis in the Institutional Repository of the University of Leiden
Downloaded from:	https://hdl.handle.net/1887/29754

Note: To cite this publication please use the final published version (if applicable).

Cover Page

Universiteit Leiden

Leiden University Repository

The handle http://hdl.handle.net/1887/29754 holds various files of this Leiden University dissertation

Author: Cao, Lu
Title: Biological model representation and analysis
Issue Date: 2014-11-20

Biological model representation and analysis

L. Cao

曹璐

Biological model representation and analysis

Proefschrift

ter verkrijging van

de graad van Doctor aan de Universiteit Leiden,

op gezag van Rector Magnificus Prof. Mr. C.J.J.M. Stolker,

volgens besluit van het College voor Promoties

te verdedigen op donderdag 20 November 2014

klokke 10:00 uur

door

Lu Cao

geboren te Zhejiang, China, in 1983

Promotiecommissie

Promotor
Prof. Dr. J.N. Kok

Co-promotor
Dr. Ir. F.J. Verbeek

Overige Leden
Prof. Dr. A.P.J.M. Siebes
Prof. Dr. T.H.W. Bäck
Prof. Dr. J. Legler

Contents

Contents **i**

1 Introduction **1**

1.1 2D and 3D microscopy images acquisition 2

1.2 Image processing and analysis 4

1.3 Phenotype measurement 5

1.4 Data analysis 7

1.4.1 Ground truth data 8

1.4.2 Feature selection/extraction 9

1.4.3 Classification 10

1.4.4 3D model representation 11

1.4.5 3D surface reconstruction 12

1.5 Structure of the thesis 12

2 Pattern Recognition in High-Content Cytomics Screens for Target Discovery: Case Studies in Endocytosis **17**

2.1 Introduction 19

2.2 Methodology 21

2.2.1 Image acquisition 21

2.2.2 Image analysis 22

2.2.2.1 High-content analysis 22

2.2.2.2 Phenotype measurement 23

2.2.3 Data analysis 23

2.2.3.1 Phenotypic sub categorization 24

2.3 Experimental results 33

2.3.1 Dynamic phenotype stage 33
2.3.2 Phenotype classification 33
2.4 Conclusions 34

3 Hierarchical classification strategy for Phenotype extraction from epidermal growth factor receptor endocytosis screening 37
3.1 Background 39
3.2 Methods 41
3.2.1 Cell material and preparation 41
3.2.2 Image acquisition and processing 41
3.2.3 Phenotype measurement 42
3.2.3.1 Texture measurement 43
3.2.3.2 Wavelet texture measurement 44
3.2.4 Production of ground truth data 45
3.2.5 Hierarchical classification strategy workflow 46
3.2.5.1 Feature normalization 47
3.2.5.2 Feature selection 48
3.2.5.3 Prior probability setting 49
3.2.5.4 Classifier 50
3.2.5.5 Analysis 51
3.3 Results and discussion 57
3.3.1 EGFR endocytosis regulator identification 57
3.3.2 Dynamic EGFR endocytosis stage 60
3.4 Conclusions 60

4 Evaluation of Algorithms for Point Cloud Surface Reconstruction through the Analysis of Shape Parameters 63
4.1 Introduction 65
4.2 Evaluation design 68
4.2.1 Generation of points and noise 69
4.2.2 Surface area calculation 70
4.2.3 Point distance calculation 71
4.2.4 Surface curvature calculation 72

4.3 Experimental results 73
4.3.1 Under/oversampling estimation 74
4.3.2 Local observation 75
4.3.2.1 Sphere model distance/area error estimation . . . 75
4.3.2.2 Ellipsoid model distance/area error estimation . . 79
4.3.2.3 Oval model distance/area error estimation 79
4.3.2.4 Sphere model curvature error estimation 82
4.3.2.5 Ellipsoid & oval model curvature error estimation 84
4.3.3 Global observation 86
4.4 Conclusion and future work 88

5 Optimizing 3D model representations for 3D phenotype analysis 91
5.1 Introduction 93
5.2 Methodology for model optimization 95
5.2.1 Contour interpolation 96
5.2.2 3D surface reconstruction 100
5.2.3 Phenotype measurement 101
5.3 Evaluation of the methodology 102
5.3.1 Evaluation of interpolation method 102
5.3.2 Evaluation of surface reconstruction method 104
5.4 Results 105
5.4.1 Zebrafish embryo, measurement verification 105
5.5 Discussion & conclusion 107

6 Phenotype analysis of arborized structures from 3D models 109
6.1 Introduction 111
6.2 Methodology for arborization structure analysis 114
6.2.1 Centerline extraction 114
6.2.2 Evaluation of centerline extraction method 115
6.3 L-system construction 117
6.4 Results 118
6.4.1 material and preparation 118

6.4.2 Prominent feature extraction 120
6.4.3 L-system modeling 123
6.5 Discussion & conclusion 125
6.6 Acknowledgement 126

7 Conclusion and Future Work 127
7.1 Image analysis and Pattern Recognition in High-throughput Screens 128
7.2 Hierarchical classification strategy for EGFR phenotype extraction 128
7.3 Analytical evaluation of point cloud surface reconstruction methods 129
7.4 3D model representation for phenotype analysis 130
7.5 Nature inspired phenotype analysis with 3D model representation 130
7.6 Conclusion and future work 131

Bibliography 133

Summary 153

Samenvatting 157

List of Publications 161

Curriculum Vitae 163

Chapter 1

Introduction

Microscopes have enabled mankind to increase the resolution of their vision in the micro and nano-scales. Fabulous visualizations can be achieved in this manner, but there are still patterns in these visualizations that need to be addressed. The technical developments in microscope instrumentation are incredible and have made it possible to observe biological structures at near molecular scale up to the tissue and organismal level (cf. Figure 1). The developments of digital instruments and computers have further boosted the area of microscope analysis. Microscopes are equipped with digital cameras and researchers can produce large amounts of high quality digital images. In these images there are patterns to be analyzed and thus we need to look for efficient and correct ways to extract information from these images and find patterns in this information. This particularly holds for the description of biological specimens that are observed in one way or the other by microscopy. The research of this thesis contributes to the efforts to find solutions in working with large amounts of images and extracting information in a correct and comprehensive way.

In this thesis, we discuss solutions of phenotype description based on the microscopy image analysis to deal with biological problems both in 2D and 3D space. Our description of patterns goes beyond conventional features and helps to visualize the unseen in feature dataset. These solutions share several common processes which are based on similar principles. Furthermore, we notice that advanced features and classifier strategies can help us improve the performance of the solutions. The biological problems that we have studied include the endocy-

tosis routing using high-throughput screening in 2D and time and 3D geometrical representation from biological structures.
In order to have a general view of the solutions, we would first introduce the generic workflow as shown in Figure 1.2 which is applicable for both 2D and 3D objects. For 3D images additional techniques are required.

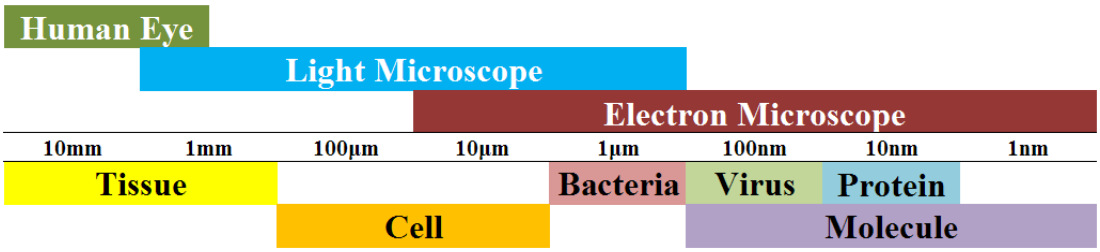

Figure 1.1. Resolution required for several objects (middle line) and the imaging equipment with which this resolution can be achieved (upper half) and the typical resolution of objects (lower half).

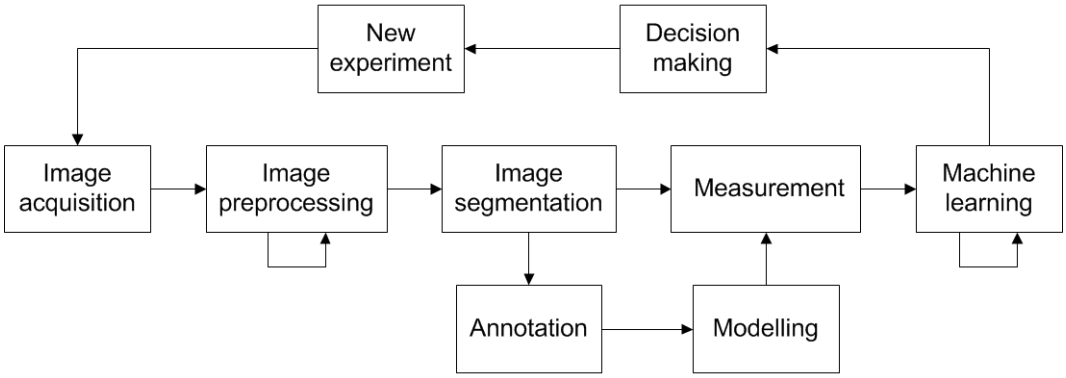

Figure 1.2. Image processing and image analysis pipeline. Image processing includes image preprocessing and image segmentation. Image analysis includes image annotation, modelling, measurement and machine leaning. The pipeline influences the decision making for a new experiment.

1.1 2D and 3D microscopy images acquisition

In the imaging pipeline, the first step is the image acquisition from microscopes. In this thesis our inputs come from different microscopes. We utilize the bright-field microscope for invasive sectioning of large structures in X,Y,Z space. For

non-invasive observation on cell level, we use confocal microscopy both for single slide screening in X,Y,T space and multiple slides sectioning in X, Y, Z space. Bright-field microscope is suitable for the imaging of stained tissue sections of specimens because the easiest way to deal with thicker specimens (3D images) is to slice the specimen into many consecutive thin sections. Given the resolution of the imaging system, they provide clear information in x and y axis (2D images), but limited information in z axis. This invasive sectioning enables the application of staining techniques so that molecular phenotype of the specimen under study can be revealed [Verbeek, 1999b]. This approach is useful for larger sections of tissue whose z-resolution is of the order of millimeters, but it will not work in the micro-nano range.

Confocal microscopy can be used in cellular high-throughput screening. It also enables observation of thick specimens by optical sectioning which eliminate the artifacts existed in specimen preparation by physical sectioning. However, optical penetration into the specimen has its limitations. The scope of confocal microscope is very good on the cellular level but less effective on the level of an organ or a tissue; concluded from Figure 1.1. Consequently, for 3D reconstruction of a larger embryo or a substantial part of it, confocal microscope is usually not always the most appropriate technique [Verbeek, 1999b].

Optical projection tomography (OPT) is another non-invasive sectioning technique for 3D biological specimens. It aims at producing high-resolution 3D images of both fluorescent and nonfluorescent biological material with a thickness of up to 15 millimeters. OPT microscopy allows the rapid mapping of the tissue distribution of RNA and protein expression in intact embryos or organ systems and can therefore be instrumental developmental biology studies for objective phenotype description. [Sharpe et al., 2002]

Subsequent to image acquisition, the process of image and data analysis starts. For both 2D and 3D microscopy images, the solutions for analysis are quite similar. In this thesis, the major focus is on the description of the phenotype measurement and data analysis. Therefore, we introduce a generalized solution for 2D and 3D images in the following sections.

1.2 Image processing and analysis

The aim of image processing and analysis is to accomplish image understanding and data reduction. The pipeline includes image enhancement or restoration and image segmentation. The first step of image processing and analysis for microscopy is to improve the quality of images by enhancing the foreground as well as suppressing the background. Image enhancement aims for improving the interpretability or perception of information in images for human viewers [Maini and Aggarwal, 2010]. We see it separated into two main categories: spatial domain filters and frequency domain filters. Spatial domain filters directly deal with the image pixels such as histogram enhancement. Frequency domain filters are performed using the Fourier transform of the image and include low-pass filters, bandpass filters and high-pass filters. Noise suppression algorithms often make a tradeoff between actual noise removal and preservation of real low-contrast detail. Most commonly used methods are linear filters such as *Gaussian filter*, *Wiener filer* [Wiener, 1964] and non-linear filters such as *median filter* and the filters based on the paradigm of its mathematical morphology [Serra, 1983].
Image segmentation is the technique dividing the image constituent parts most notably in foreground and background. So it results in a separation of foreground and background. In microscopy it is specifically used to detect objects, object regions or edges in an image. Basically the image segmentation is divided into two approaches: region-based segmentation and edge-based segmentation [Tripathi et al., 2012]. Region-based segmentation partitions an image into regions that are similar according to a set of predefined criteria [Gonzalez and Woods, 2001]. Some representative methods include *thresholding*, *clustering* and *region growing*. The thresholding operation converts a gray-scale image into a binary image by a set of thresholds. Popular methods include the *maximum entropy method* [Leung and Lam, 1994], *Bernsen's method* [Bernsen, 1986], *Niblack's method* [Niblack, 1985], *Isodata method* [Manakos et al., 2000], *Otsu's method* [Otsu, 1979]. Clustering partition the image into the sets or clusters of pixels which have similar feature space. Clustering methods can be further divided into *k-means clustering* [Kanungo et al., 2002] and *fuzzy clustering* [Naz et al., 2010]. Region growing extracts a region of the image that is connected based on predefined criteria [Chen

and Shen, 2010]. Region growing techniques are often used in noisy images where edges are extremely difficult to detect. Some well-known region based segmentation methods include *the level set method* [Qu et al., 2007], *watershed transformation* [Vincent and Soille, 1991] and *texture segmentation* [Ray et al., 2008]. In Edge-based segmentation, an image is partitioned based on abrupt changes in the intensity values [Gonzalez and Woods, 2001]. In Edge-based segmentation first the edges are identified. These are linked together to form consistent boundaries. Many edge operators are applied to locate edges in images such as *the Sobel operator*, *the Prewitt operator* and *the Canny operator* [Gonzalez and Woods, 2001]. The canny operator is used to find the edge pixels while eliminating the influence of noise. Other well-known edge-based segmentation method is *active contours* [Kass et al., 1988].
If the aim is to measure information on objects in the image then subsequent to segmentation a labeling operation is required. Each object from the segmentation process is attributed a label which can, if necessary, be given an annotation [Verbeek, 1999a] to provide biological context. An automatic annotation method can be regarded as a multi-class object classification which is based on image analysis to extract features and data analysis to train a proper classifier. In the next section, we introduce the necessary concepts and context for this thesis.

1.3 Phenotype measurement

In order to correctly annotate each object separated from the segmentation method, we need to quantify the object into all kinds of features describing the unique pattern of the object for further multi-class classification. This quantification step is, de facto, the measurement of the phenotype. Here we introduce two basic definition on phenotype measurement.

Definition 1.3.1. *"Phenotype is the set of observable characteristics of an individual resulting from the interaction of its genotype with the environment."*

Definition 1.3.2. *"Phenotype measurements imply the measurement of observ-*

able attributes, reflecting the biological function of gene variants as affected by the environment." [Paulus et al., 2013]

For biological specimens, phenotype measurement is the next important step in image analysis. The phenotype measurements will be used to classify objects obtained from the segmentation into different categories that are meaningful with respect to the biology. Thus, it is crucial to measure representative features for each object in the image. These features, often, represent the characteristics of shape, intensity and texture of the objects.
Generally in 2D space, we can categorize the phenotype measurements into two groups: basic measurements and localized measurements. Basic measurements of the phenotype cover shape descriptors, texture patterns and invariant features. Localized measurements of phenotype describe the assessment of the correlation between multiple information channels. The information channels in the context of the research presented in this thesis are the imaging channels. The reason for splitting the channels in different parts of the color spectrum is that each channel contains individual characteristics of the object under investigation due to a specific staining method resulting in biological meaning.
For 3D images and 3D geometrical models, we need to look at different features. One group concerns the feature-based measurements including both global shape, such as volume and surface area, and local features such as surface curvature. Another part of phenotype measurements is graph based indicating the use of the geometrical and topological shape properties such as skeleton and centerline; in such a way that faithful and intuitive features can be derived.
For each study that we will introduce in this thesis, we intend to find the advanced and representative phenotype measurements from the biological image dataset so as to facilitate the solution of a specific biological question. There is no general standard for the selection of phenotype measurements and it is unrealistic to use all the extracted features for pattern classification. Normally, related phenotype measurements are based on the biological descriptions and further use feature selection methods to distill the feature dimensions for classification training. In order to extract related features, the knowledge combined from biologists and computer scientists is required. The image features as described by the biologists, are based on biological principles. These features are observable. The

computer scientists need to translate the feature description into features that can be derived through computation. We call it hidden features. Hidden features are those that can not be derived other than through computation from the digitized image. These features intend to use some advanced and invariant features to represent the biologists' description. In addition, the computer scientists can detect the variance of some other advanced measurements which can be further introduced in the phenotype measurements process.

1.4 Data analysis

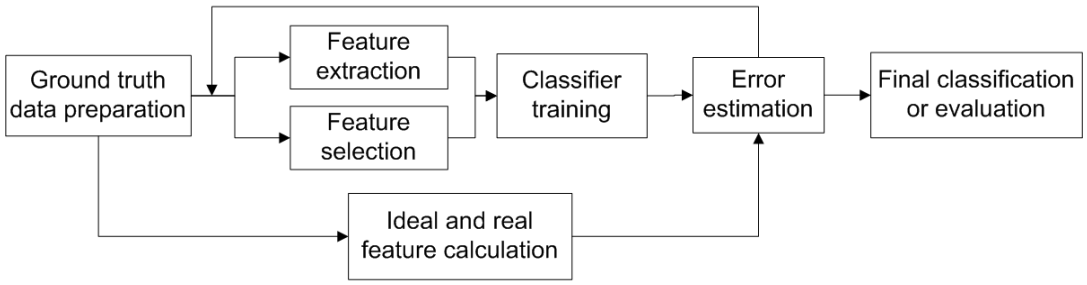

Figure 1.3. The model of phenotype data analysis.

Data analysis pipeline includes ground truth data preparation, feature reduction and classification as shown in Figure 1.3. For a description of phenotype we need ground truth data. For data analysis a good idea of ground truth is important; so for phenotype analysis we need good ground truth examples. But what is ground truth? Therefore we first give a definition.

Definition 1.4.1. *In machine learning, the term "ground truth" refers to the accuracy of the classification of the training for supervised learning techniques. This accuracy is used in statistical models to prove or disprove research hypotheses.*

In image processing, ground truth data could be derived from manual delineation by experts, synthetic images or analytical models based on mathematical expressions. These ground truth data set is used in both phenotype classification

and performance evaluation. Phenotype classification is discussed in 1.4.3.
In our workflow, after having ground truth data for reference, the next step is feature reduction including feature selection and feature extraction in the feature space. This step intends to find prominent features from the feature pool. Feature selection reduces the dimensionality of the feature set by selecting the subset of features from the original set. Feature extraction maps the original feature set into a new set with a reduced dimensionality. Next, classifier training tries different kinds of classifiers and uses an error estimation step to select the classifier with the lowest error.
We strive at using the best performing combination of feature reduction and classifier method for phenotype classification. For the process of performance evaluation, we start with preparing the ground truth data. Then, we measure the ideal features from the ground truth data and real features from the output of the methods. Next, we calculate the difference between ideal and real features by an error estimation.

1.4.1 Ground truth data

The verb "ground truthing" refers to the process of gathering the proper objective data for the test. Based on this ground truth, researchers train a suitable classification method to deliver probabilistic predictions for new observations [Kirchner et al., 2010]. For example, in next generation sequencing technology (NGS), ground truth data is used to train a standard supervised machine learning algorithm for the purpose of identifying somatic mutations from NGS data [Ding et al., 2011]. In classification of plant organs from laser scanned point clouds, the commercial software Geomagic Studio 12 is used to manually assign the ground truth data [Paulus et al., 2013].
Apart from classification training, ground truth is also used for performance evaluation of algorithms and methods. It checks whether the algorithm produces the right output or not. It is frequently used in the evaluation of image segmentation algorithms. The ground truth could be artificial or synthetic images which provide an unbiased ground-truth. Regarding a performance test with the microscopy images, the ground truth images are obtained by manual segmentation

performed by biologists through tracing on a digitizer surface. In order to reduce the observation bias during the manual segmentation, the experts need to repeat several times to obtain an idea of inter user variance [Yan and Verbeek, 2012b]. Similar ground truth production construction is used for algorithm evaluation including retinal vessel segmentation methods [Kaba et al., 2014], simultaneous recognition and segmentation (SRS) of cells [Qu et al., 2011] and microarray segmentation algorithms [Lehmussola et al., 2006]. The ground truth is also used in other methods evaluation discussed as follows: the study in [Lee et al., 2012] computes the distance between the reconstruction and the ground truth to analyze the accuracy of the 3D Neuronal Structure Reconstruction method; in next-generation sequencing, read mapping and genome-wide domain annotations are combined as the ground truth for evaluating the read classification sensitivity and specificity [Zhang et al., 2013]. For a better use of ground truth data, there are even further discussions on introducing a way to design ground-truthed data to compare and evaluate the performance of the real-world detectors [Vedaldi et al., 2010] and creating a ground truth database to evaluate algorithms in the field of mobile robots [Takeuchi et al., 2003].

1.4.2 Feature selection/extraction

In the pool of quantified features, some redundant or irrelevant features can occur within the feature set. Therefore, feature selection process is applied to select a subset of relevant features for further classification. Some popular feature selection methods include the *branch and bound procedure*, *sequential backward* and *forward selections*, *best individual feature selection*.
The branch and bound procedure is a top-down procedure without exhaustive search. It constructs a tree by deleting features successively based on the monotonicity property [Webb and Copsey, 2011].
Sequential forward selection is a bottom-up search procedure that starts with a null set and adds new features to the feature set one at a time until the final feature set is reached. An important disadvantage of the method is the lack of a mechanism of deleting features from the feature set once they have been added.

Sequential backward selection is the other way around. It is a top-down procedure starting with a complete feature set and deleting features one at a time until a predefined dimensionality of the set is reached. The disadvantage of the backward selection method is that it is computationally more demanding compared to forward selection during the criterion function evaluation.
The best individual feature selection [Webb and Copsey, 2011] is the simplest selection method, it might also be the one giving poorest performance; such occurs especially when the features are highly correlated [Webb and Copsey, 2011].
In addition, feature extraction is used to reduce the dimension of the feature set by combining the original features into reduced new features with functions.
Feature extraction is divided into supervised and unsupervised methods. *Principal component analysis* (PCA) is a typical unsupervised feature extraction method. This method aims at deriving new variables (in decreasing order of importance) that are linear combinations of the original variables and that are uncorrelated. *Principal component analysis* is a variable-directed technique and therefore is described as an unsupervised feature extraction technique [Webb and Copsey, 2011]. *Linear discriminant analysis* (LDA) is a supervised feature extraction method. It searches the directions for the maximum discrimination of classes in addition to the dimensional reduction. The criterion proposed by LDA is the ratio of between-class to within-class variances. It is generally believed that when it comes to solving pattern classification problems, LDA algorithms outperform PCA-based ones, since the former optimizes the low dimensional representation of the objects and focus on the most discriminant features, while the latter achieves simply object reconstruction [Youness and Hamid, 2013].
From analysis the microscopy images we can derive large amount of features. However, these features are not all prominently describing the phenotypical differences. Therefore we require a feature reduction method to control the redundancy and consistency that exist in our original feature set. If these two feature reduction process are carefully selected, the prominent information from original feature set could be extracted to perform a more efficient classification using this reduced feature set rather than using the complete original set of features.

1.4.3 Classification

Classification is a procedure in pattern recognition to identify objects in specific categories based on a training set of data containing labeled objects of known category. As for a supervised learning, the training set, in our case also regarded as ground truth data, is crucial for a correct classification. It needs to include a sufficiently large dataset with a variety of situations. Algorithms that implement classification schemes are called classifiers. Classifiers are divided into parametric and non-parametric categories. *The linear classifier* and *the quadratic classifier* belong to parametric category and *the k-nearest neighbor classifier* is in non-parametric category. Linear and quadratic discriminant functions are based on a normal distribution. The linear discriminant rule is quite robust and divides dataset from the normal distributions under the assumption of an equal covariance matrix. However, it is often better to use the quadratic rule if the sample distributions are not separated by the mean-difference but separated by the covariance-difference [Fukunaga, 1990; Webb and Copsey, 2011]. *The k-nearest neighbor classifier* assigns a point x to a particular class based on a majority vote among the classes of the k nearest training points to x. It is a simple and flexible classifier with a good classification performance. However, as the number of objects in the training set increases, it may lead to an excessive computational overhead [Fukunaga, 1990; Webb and Copsey, 2011].
After classification, the phenotypes in segmented objects from images are sorted into different categories. Subsequently we can analyze the changes of a specific category with different biological treatments or across a time line. These changes or trends are meaningful to proof a hypothesis in bio-medical research.

1.4.4 3D model representation

3D models can be represented in three ways: voxel, contour and surface [Verbeek et al., 1995]. voxel models use volume to represent the objects. These models are more realistic but more difficult to construct. The surface models use a surface element to represent the objects such as triangulated surface. These models are easier to deal with since the scale of the computing dataset is much smaller

than voxel models. Thus, surface models are often used to represent 3D models nowadays. Surface representation can contribute to the phenotype measurement considerably well. Many shape based features, such as surface area, volume, curvature, can be calculated well from a surface description. This requires a good surface description.

1.4.5 3D surface reconstruction

A large amount of research has been performed on surface reconstruction from a stack of 2D slices i.e. plan parallel sampled data. One direction is called contour based reconstruction methods. The existing approaches mostly fall into two categories: contour stitching and volumetric methods. Contour stitching directly connect the adjacent contours, while the volumetric methods need to interpolate intermediate gray-values firstly and extract the isosurface from the volumetric field.
The other, evenly popular direction is referred to as point cloud based reconstruction methods. In the literature, the proposed approaches are generally classified into two categories: explicit representation and implicit approximation. The major explicit representations include parametric surfaces and triangulated surfaces. Parametric surfaces attempt to represent all shapes with a set of elementary shapes such as super-quadratics, generalized cylinders, parametric patches, etc. In the explicit representation, all or most of the points are directly interpolated based on structures from computational geometry, such as *Delaunay triangulations* [Boissonnat, 1984], *alpha shapes* [Amenta et al., 2000], or *Voronoi diagrams* [Amenta et al., 1998]. The implicit approximation is based on a scheme which integrates characteristic of each point on the surface into a feature function, a.k.a. the implicit function such as *Fourier-based reconstruction scheme* [Kazhdan, 2005] and *Poisson reconstruction method*. The selection of a surface reconstruction method is important to precisely preserve the surface characteristics and show robustness in the presence of noise. This is addressed in this thesis to be able to come to good features derived from 3D images.

1.5 Structure of the thesis

The image data that are the basis of the phenotypical descriptions are the level of 2D dynamic images (x,y,t) and 3D images (x,y,z). Chapter 2 and Chapter 3 exemplify the image and data analysis of dynamic 2D image at cellular level as derived from high-throughput screening experiment. Chapter 4, Chapter 5 and Chapter 6 describe the 3D image representation and analysis at tissue/organ/organismal level.

The research in Chapter 2 illustrates the design and implementation of a system for automated high-throughput image and data analysis. The phenotypes are characterized according to a model that describes the process of endocytosis, i.e. the ability of cells to absorb molecules, in three characteristic stages. These stages are referred to as episodes and through image processing we try to establish these episodes and the vesicles involved in the ensocytosis are different for each episode. In the late process these vesicles are forming a cluster near the region of the nucleus. According to the model and the observations that it was conceived from, such cluster is larger, brighter and close to the nucleus. From the perspective of image processing, this requires to compuet the area, integrated intensisty of the vesicle and many more possible features derived from objects, i.e. vesicles, that are indentified in the image. From the computer scientists' point of view, it means to calculate the area, the intensity of the labeled object etc. Apart from standard phenotype measurements, we make use of the localized feature of phenotype such as closest object distance which is the distance between the object and the nuclei region so as to describe the correlation between two information channels. We obtained the ground truth data for classifier training by having the three characteristic episode groups manually delineated by biologists; this gives as binary mask. We make use of these binary masks for further phenotype measurements and derive the training set for the supervised classification procedure. Next, we use the model of phenotype data analysis for the classification of the three episodes (plasma-membrane, vesicle and cluster). We evaluate the performance of the combination of different feature selection and classification methods and select one with the lowest error estimation. The experimental results show that our analysis setup for high-throughput screening provides scalability and

robustness in the temporal analysis of an EGFR endocytosis model.
In Chapter 3, the results of Chapter 2 are further evaluated. Chapter 3 illustrates an integrated method employing a hierarchical classification strategy and wavelet-based texture measurements to further improve the recognition of phenotypic episodes of EGFR during endocytosis. During the previous single classifier training in Chapter 2, we find that the similarity between cluster and vesicle is higher than with plasma-membrane. As a result, we construct an advanced hierarchical classification strategy. This hierarchical classification strategy can construct the classes in a tree structure and train the classifier for each parent node to distinguish two child nodes that belong to the same parent node. We also introduced wavelet texture features to distinguish endosomes phenotype variation across timeline instead of the average intensity for each object, because a texture feature in a local patch is more discriminative than pixel intensities for candidate identification [Song et al., 2013]. The result of the hierarchical classifiers with wavelet-based texture measurements shows a noticeable improvement compared to the single classification strategy.
In Chapter 4, the work uses an analytical approach to evaluate four classical surface reconstruction methods. We make use of the ground truth concept for the evaluation of 3D surface reconstruction methods. In order to make an objective assessment of the surface quality, we utilize three synthetic objects for the error estimation. From mathematics, an analytical description of each synthetic objects is available. The three synthetic objects are the sphere, the ellipsoid and the ovoid. The parametrical mathematical representation of these synthetic surfaces helps us to compute the ideal surface features and provides a ground truth for the error estimation of surface. For the real surface feature calculation, we firstly deviate the ideal model by adding different levels of noise. Next, we use the noisy point cloud as our input for the reconstruction algorithms. Finally, we calculate the real surface feature from the reconstructed surface model. The aim of this evaluation study is to select the outstanding reconstruction method to improve reliability in surface reconstruction of biological models.
In order to apply the findings of Chapter 4, optimized 3D geometrical descriptions are requried. In Chapter 5, we therefore provide a pipeline to optimize the stack of biological images in 3D space and analyze the phenotypical difference by

extracting related shape features from the 3D biological model.
In Chapter 6 we applied the results from Chapter 4 and Chapter 5 for phenotype measurements; we extract centerline of the rodent newborn lactiferous duct to unfold the branch structure embedded in the duct rather than use standard surface descriptions. Next, we use the quantified features from the centerline to detect the morphological changes on the duct surface model. Furthermore, we extended the usage of ground truth for the simulation of mammary gland in Chapter 6. With the inspiration from the tree-like structure of mammary gland, we use a mathematical model: Lindenmayer systems (L-systems) which is a mathematical theory developed for the description of growth patterns in plants. We create a specified model for lactiferous duct of the new-born mouse from the L-system as our ground truth. With this mathematical model, we can simulate the phenotypical variation between various treatments by changing the parameters representing prominent features derived from phenotype measurements.
We conclude the discussion of this thesis in Chapter 7 with the insights that are obtained from the research describes in the Chapters 2-6.

Chapter 2

Pattern Recognition in High-Content Cytomics Screens for Target Discovery: Case Studies in Endocytosis

Based on:
L. Cao, K. Yan, L. Winkel, M. de Graauw, F.J. Verbeek. Pattern Recognition in High-Content Cytomics Screens for Target Discovery: Case Studies in Endocytosis. Pattern Recognition in Bioinformatics 2011, Delft, LNCS Springer, pages 330-342, 2011

Abstract: Finding patterns in time series of images requires dedicated approaches for the analysis, in the setup of the experiment, the image analysis as well as in the pattern recognition. The large volume of images that are used in the analysis necessitates an automated setup. In this paper, we illustrate the design and implementation of such a system for automated analysis from which phenotype measurements can be extracted for each object in the analysis. Using these measurements, objects are characterized into phenotypic groups through classification while each phenotypic group is analyzed individually. The strategy that is developed for the analysis of time series is illustrated by a case study on EGFR endocytosis. Endocytosis is regarded as a mechanism of attenuating epidermal growth factor receptor (EGFR) signaling and of receptor degradation. Increasingly, evidence becomes available showing that cancer progression is associated with a defect in EGFR endocytosis. Functional genomics technologies combine high-throughput RNA interference with automated fluorescence microscopy imaging and multi-parametric image analysis, thereby enabling detailed insight into complex biological processes, like EGFR endocytosis. The experiments produce over half a million images and analysis is performed by automated procedures. The experimental results show that our analysis setup for high-throughput screening provides scalability and robustness in the temporal analysis of an EGFR endocytosis model.

2.1 Introduction

In this paper we address the problem of deriving a phenotype of a cell in the context of time-lapse cytomics data; in particular we investigate the process of endocytosis and epidermal growth factor receptor (EGFR) signaling.
Enhanced epidermal growth factor receptor (EGFR) signaling triggers breast cancer cells to escape from the primary tumor and spread to the lung, resulting in poor disease prognosis. Moreover, it may result in resistance to anti-cancer therapy. In normal epithelial cells, EGFR signaling is regulated via endocytosis, a process that results in receptor degradation and thereby attenuation of EGFR signaling. However, in cancer cells the endocytosis pathway is often defective, resulting in uncontrolled EGFR signaling. Over the past years, RNA interference combined with fluorescence microscopy-based imaging has become a powerful tool to the better understanding of complex biological processes [Pelkmans et al., 2005]. Such combined experiment often produces over half a million multi-channel images; manual processing of such data volume is impractical and jeopardizes objective conclusions. Therefore, an automated image and data analysis solution is indispensable. To date, analysis was done with simple extraction of basic phenotypes from EGFR images using tools such as BioApplication [Ghosh et al., 2005], ImageXpress [Galvez et al., 2007] and QMPIA [Collinet et al., 2010]. However, these tools are not suitable for a profound study of the dynamics behind EGFR endocytosis which requires more attention. From the existing literature [Collinet et al., 2010; Galvez et al., 2007; Ghosh et al., 2005; Li et al., 2009; Roepstorff et al., 2008; Tarcic et al., 2009; Ung et al., 2011] a generic model, defining four major episodes of EGF-induced EGFR endocytosis, can be distilled. (1) Under control conditions, EGFR localizes at the plasma-membrane site for internalization, which is in our study defined as the "plasma-membrane" episode. (2) Upon binding of EGF to the receptor, EGFR is taken up into small vesicular structures and starts sorting in early endosomes, which is defined here as the "vesicle" episode. (3) Over time EGFR containing vesicles are transported to late endosomes localizing near the nuclear region and form into a larger complex multi-vesicular body, defined here as the "cluster" episode. (4) In final episode, EGFR is degraded in the lysosomes. In addition to this route, EGFR can also

partly be transported back to the plasma-membrane sites. Using this dynamic model as the major guideline, the analysis of EGFR-regulation-related gene pathway could be linked to each stage of EGFR endocytosis. Instead of looking at one fixed time point, our current experimental design includes a series of time points at which images are captured. An image potentially contains a ratio in the first three characteristic episodes in the EGFR endocytosis process. The image analysis solution should be able to extract basic phenotype measurements as well as to identify the stage of EGFR. In this paper, we illustrate the design and implementation of an automated setup for high-content image and data analysis which can properly capture EGFR dynamics and classify different EGFR phenotypes.

Our workflow for automated analysis solution is depicted in Figure 2.1. Each high throughput screening (HTS) experiment starts with the design of the experimental scheme, followed by the wet-lab experiment and high throughput microscopy-based imaging. Both experimental schemes and image data are organized and stored in a database. Subsequently, image analysis is used to extract phenotype measurements from these images and classifiers are introduced to recognize each phenotypic stage of EGFR. Finally, comprehensive conclusions are drawn based on comparisons of EGFR expression at each stage and time point.

In this paper, we limit the scope to image analysis and data analysis, some biology will be explained. Accordingly, the organization of this paper is divided into three major sections. In section 2.2, we introduce the methodology including image acquisition and image analysis; several innovative algorithms will be briefly introduced. After segmentation of the images, EGFR phenotype measurements are obtained. We will illustrate the categorization of phenotypic stages using feature selection and classification. The best combination pair is applied on image data to classify three phenotypic stages and construct a phenotype model. The experimental results are presented in section 2.3 with two case studies. The first case study tests our solution in identifying dynamic phenotype stages. The second study case examines robustness and scalability of our solution in analyzing a large number of phenotypes.

2.2 Methodology

Modern techniques in fluorescence microscopy allow visualizing various cell structures so that these can be specifically subject to analysis. Together with a computer-controlled microscope, a high-throughput image acquisition scheme, known as high-throughput screening (HTS), has become feasible. Depending on the biological question at hand, a HTS experiment may produce up to half million images. Such a volume of images is beyond the capacity of manual processing and therefore, image processing and machine learning are required to provide an automated analysis solution for HTS experiments. In this section, we will introduce the image acquisition protocol followed by approaches for image analysis and data analysis.

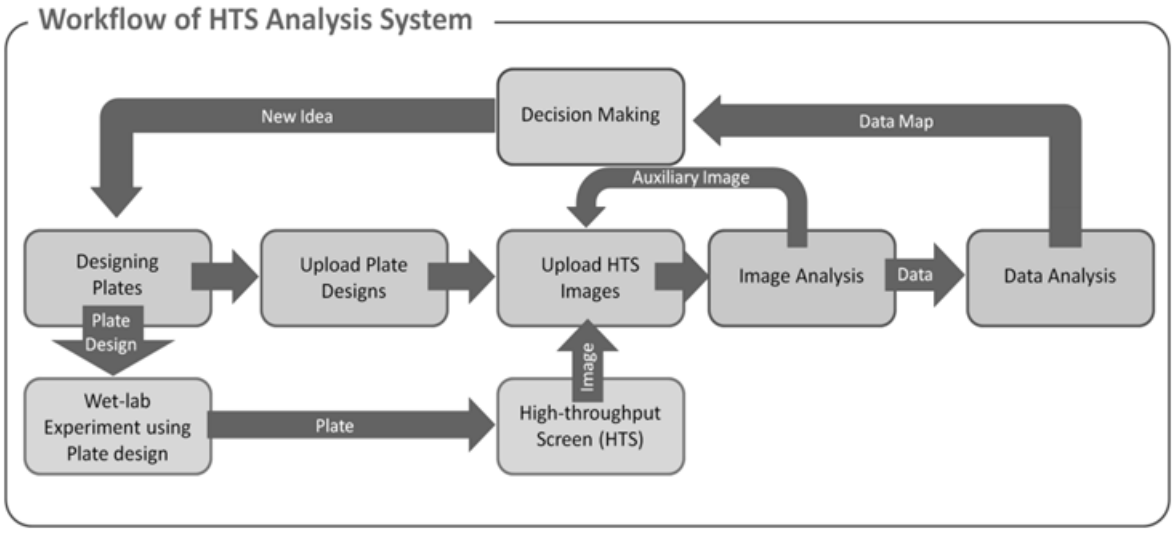

Figure 2.1. Workflow of our HTS Analysis System. The basic entity for processing cells is the 96 well culture plate. A virtual plate (layout) is designed before the experiment and the data are often kept together per "plate".

2.2.1 Image acquisition

The workflow for data preparation for the experiment discussed in this chapter here includes three essential steps: (1) cell culturing, siRNA transfection and EGF exposure, (2) fluorescent staining of proteins of interest and (3) image acquisition.

Here we use a design of an EGFR-regulation related siRNA screening to illustrate this workflow. In this design, cells are cultured in 96 well culture plate and transfected using Dharmafect smartpool siRNAs. Subsequently, the transfected cell population is exposed to epidermal growth factor (EGF) for a different duration of time. Cells are fixed at different time points and visualized with a confocal laser microscope (Nikon TE2000). Image acquisition automation is realized with an automated stage and an auto-refocusing lens controller. For each well, images are captured from ten randomly selected locations. For each image three channels are captured: (1) a red channel containing P-ERK expression staining (Cy3), (2) a green channel containing EGFR expression staining (Alexa-488) and (3) a blue channel containing a nuclear staining (Hoechst #33258). Upon completion of the acquisition process all images are uploaded to a database server for image analysis.

2.2.2 Image analysis

2.2.2.1 High-content analysis

Basically, the image analysis procedure converts raw microscope images into quantifications representing characteristic biological phenomena. A number of steps are elaborated to achieve this purpose; starting from image acquisition, three steps are distinguished: (1) noise suppression, (2) image segmentation and (3) phenotype measurement. Image segmentation refers to the process of partitioning an image into multiple regions with the goal to simplify and/or change the representation of an image into something that is easier to analyze. For fluorescence microscopy cell imaging we specifically designed a segmentation algorithm: i.e. watershed masked clustering (WMC). The WMC algorithm (cf. Figure 2.2d) [Yan and Verbeek, 2012b] is an innovative and customized segmentation algorithm that serves different types of cytomics studies like dynamic cell migration analysis [Bera and Jarque, 1981; Roepstorff et al., 2008; Yan et al., 2009a] and protein signaling modeling [Qin et al., 2012b]. Due to the absence of an indicator for the cell border (cf. 2.1), a border reconstruction and interpolation algorithm is designed to provide artificial representations of the cell borders; i.e. the weighted Voronoi diagram based reconstruction (W-V) algorithm [Qin et al., 2012b]. The

W-V algorithm (cf. Figure 2.2c) offers the possibility to measure both border-related signal localization [Qin et al., 2012b] and protein expression in terms of continuity and integrity [Qin et al., 2012b]; it does not require a complete cell border or cytoplasmic staining. Both binary mask and artificial cell border are used to derive a number of phenotype measurements for further data analysis.

2.2.2.2 Phenotype measurement

In the current experiment and imaging protocol, the phenotype measurements can be categorized into two subgroups: (1) basic measurements of the phenotypes covering shape descriptors and (2) the localization phenotype describing the assessment of the correlation between two information channels. The basic phenotype measurement [Damiano et al., 2011; Le Dévédec et al., 2010; Yan et al., 2009a] includes a series of shape parameters listed in Table 2.2. In addition to the basic phenotype measurement [Damiano et al., 2011; Le Dévédec et al., 2010; Qin et al., 2012b; Yan et al., 2009a], localization measurements can be derived for a specific experimental hypothesis; e.g. the expression ratio between protein channels or shape correlation between objects. The localization phenotypes are quantifications of comparative measurement between information channels such as relative structure-to-nucleus distance or structure-to-border distance [Qin et al., 2012b]. In this paper, we will limit the scope of phenotype measurements to the set employed by the study on EGFR endocytosis. In Table 2.3 a list of EGFR screening based localization phenotypes is shown. On the basis of the phenotype measurements, objects are classified into phenotypic stages. For the assessment of significance statistical analysis is performed.

2.2.3 Data analysis

The aim of the endocytosis study is to quantify the process of EGF-induced EGFR endocytosis in human breast cells and to identify proteins that may regulate this process. The EGFR endocytosis process can roughly be divided into three characteristic episodes:plasma-membrane, vesicle and cluster. The characteristic episodes are the read-out for HTS. Based on this model it is believed that EGFR endocytosis regulators may be potential drug targets for EGFR-induced breast

cancer. Studying each of the stages (cf. Figure 2.3), i.e. plasma-membrane, vesicle and cluster, may provide a deeper understanding of the EGFR endocytosis process.

Table 2.2. Basic measurements for a phenotype (after segmentation to binary mask)

Feature Name	Description
Size	The size of object, aka as the surface area.
Perimeter	The perimeter of the object.
Extension	Derived from 2nd-order invariants of the object [Hu, 1962; Yan et al., 2009a].
Dispersion	Derived from 2nd-order invariants of the object [Hu, 1962; Yan et al., 2009a].
Elongation	Derived from 2nd-order invariants of the object [Hu, 1962; Yan et al., 2009a].
Orientation	Derived from 2nd-order moments of the object [Hu, 1962; Yan et al., 2009a].
Intensity	Average intensity of all pixels belong to an object.
Circularity	Area-to-perimeter ratio; higher compactness suggests a more smooth and less protrusive shape.
Semi-major axis length	Derived from 2nd-order moments of the object [Hu, 1962; Yan et al., 2009a].
Semi-minor axis length	Derived from 2nd-order moments of the object [Hu, 1962; Yan et al., 2009a].
Closest object distance	The distance to nearest neighbor of the object, the distance is measured similar to the border distance in Table 2.3.
In nucleus	Boolean describing if the object is included in nucleus mask.

2.2.3.1 Phenotypic sub categorization

Here we introduce a profound explanation of the whole procedure employed in the phenotypic sub-categorization including the production of a training set and

the procedure for the training of the classifier. The training set is derived from manually delineated outlines of each phenotypic group and is subsequently used to train a classifier distinguishing three different phenotypes. From two case studies the capability of our solution with respect to identifying characteristic episodes in the process under study stages as well as the scalability in describing different phenotypic groups, is assessed.

Preparation of the Training Set. Ground truth data were obtained by the outlines of the three characteristic episode groups, i.e. cell border/plasma-membrane, vesicle and cluster. These were separately delineated by biologists using our dedicated annotation software (TDR) with a digitizer tablet (WACOM, Cintiq LCD-tablet). From each outline a binary mask is created for each phenotypic stage. In Figure 2.4(b) the vesicle mask derived from a manually selected vesicle outline is shown. This mask is overlaid with the mask obtained from the WMC algorithm so as to extract the intersection set of two masks as shown in Figure 2.4(d). Finally, the phenotype measurements are computed with this mask. In similar fashion the ground truth datasets for the plasma-membrane and cluster groups are prepared.

Table 2.3. Localization measurement

Feature Name	**Description**
Nucleus distance	Distance between structure and nucleus, measured as the average distance between each pixel in an object and the center of mass of the corresponding nucleus.
Border distance	Distance between structure and cell membrane, measured as the average distance between each object-pixel and the center of mass of the cell border (membrane).
Intactness	Overlap between structure expression and cell membrane divided by the total length of cell membrane.

The training dataset includes three characteristic episode groups with 2254 objects and 14 features. Given the huge differences in the feature ranges, it is necessary to normalize the dataset. Normalization is accomplished by shifting the mean of the dataset to the origin and scaling the total of variances of all features to 1. In this way the magnitude effect is successfully removed and the

recognition accuracy can be significantly improved [Okun, 2004]. The normalized dataset is used for training of the EGFR classifier.

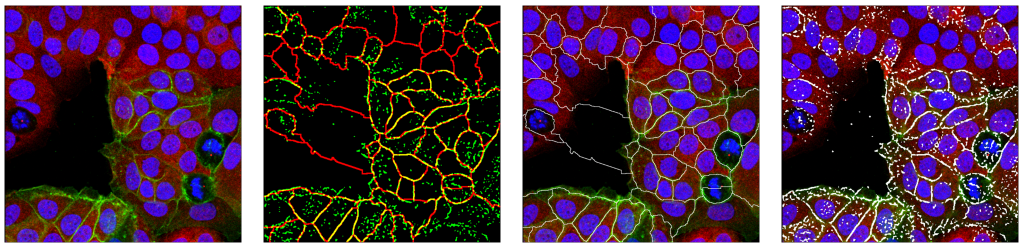

(a) (b) (c) (d)

Figure 2.2. (a) Original image: PERK(red), EGFR (green) and nucleus (blue), (b) Component definition: artificial cell border (red) and binary mask of protein expression (green), (c) cell border reconstruction : artificial cell border (W-V), (d) image segmentation: binary mask of EGFR channel by WMC.

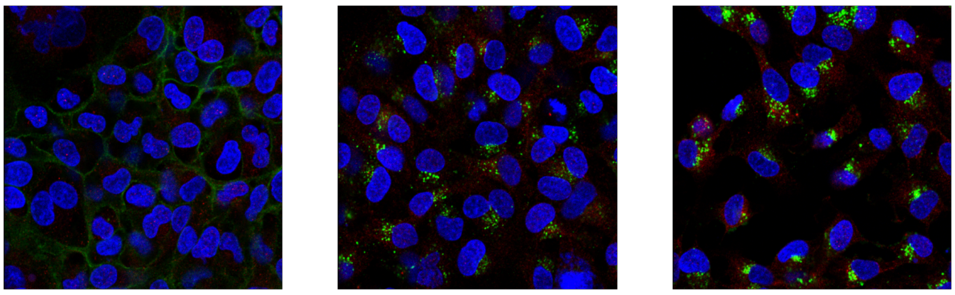

(a) (b) (c)

Figure 2.3. Sample images of the 3 phenotypic groups with (a) Plasma-membrane, (b) Vesicle, (c) Cluster.

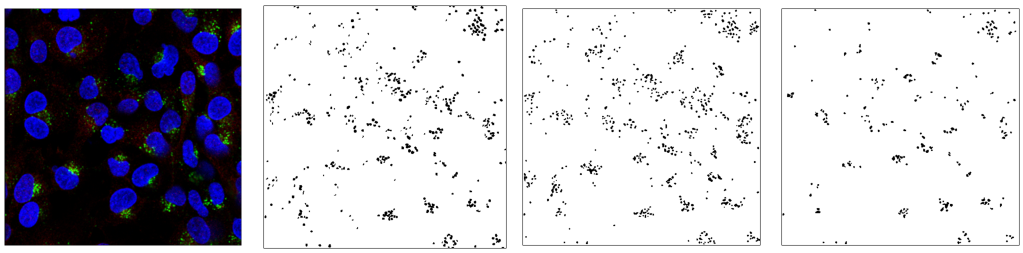

(a) (b) (c) (d)

Figure 2.4. Ground truth data production. (a) Original image, (b) manual mask, (c) WMC mask, (d) overlay of the mask.

Feature Selection. First, it is crucial to make a selection of the probabilistic distance criterion for the discriminability estimation. For this we choose the Mahalanobis distance [Mahalanobis, 1936a] since it takes the correlations among the variables into consideration and, in addition, it is scale-invariant. Other distance criteria, such as the Euclidean or Manhattan distance, are, more or less, related to the assumption that all features are independent and have an equal variance. We cannot be certain that all features in our dataset are independent and therefore the Mahalanobis distance is preferred.
Second, we have selected three representative search algorithms including parametric and non-parametric search algorithms; i.e. the branch and bound procedure [Land and Doig, 1960a], best individual N features and sequential backward selection [Jain et al., 2000]. Branch and bound is a top-down procedure, beginning with the set of variables and constructing a tree by deleting variables successively; i.e. an optimum searching procedure requiring the evaluation of partially constructed or approximate solutions without involving exhaustive search. Best individual N features procedure is the simplest suboptimal method for choosing the best N features by individually assigning a discrimination power estimate to each of the features in the original set. In some cases, especially if the features from original set are uncorrelated, this method results in a well-defined feature sets. Sequential backward selection is another suboptimal search algorithm. Variables are deleted one at a time until the required number of measurements remains [Fukunaga, 1990]. The advantage of backward selection is its capability for global control during the feature selection.
Third, we choose three classifiers covering both linear and non-linear categories; i.e. the linear classifier (LDC), the quadratic classifier (QDC) and k-nearest neighbor classifier (KNNC). A linear classifier makes a classification decision based on the value of a linear combination of the characteristics [Mitchell, 2005]. If the data are strongly non-Gaussian, they can perform quite poorly relative to nonlinear classifiers [Devroye et al., 1996]. A quadratic classifier, which is generalization of the linear classifier; it separates measurements of classes by a quadric surface. Finally, the k-nearest neighbor classifier classifies an object by a majority vote of its neighbors, with the object being assigned to the class most common amongst its k nearest neighbors. The k-nearest neighbor rule achieves a consistent high

performance, without a priori assumptions about the distributions from which the training examples are drawn. Moreover, it is robust with respect to noisy training data and still effective if the training dataset is large. By permutation we obtained 9 pairs of combinations. The result of the error estimation is shown in Figure 2.5. An interesting characteristic can be observed in these plots. The weighted error of the quadratic classifier jumps abruptly when the number of features exceeds a certain threshold (10 for individual feature selection, 12 for branch & bound, and 5 for backward feature selection). This is caused (1) by including a feature with which it is hard to distinguish three phenotypic groups and (2) by the fact that the distribution of the three classes might be more properly classified by the linear and k-nearest neighbor classifier rather than quadratic classifier.

Feature extraction. Feature extraction is another category to manage multi-dimensional features by reducing dimensionality of features trough combining. For the final result, we also test the performance of the feature extraction combined with the three classifiers selected. As our starting point is a labeled training dataset, a supervised feature extraction method is most suitable. The Fisher mapping [Fukunaga, 1990] is chosen as extraction method. Fisher mapping finds a mapping of the labeled dataset onto an N-dimensional linear subspace such that it maximizes the between-scatter over the within-scatter. It should be taken into account that the number of dimensions to map is less than the number of classes in the dataset. We have three phenotype classes and consequently the labeled dataset can only be mapped onto a 1D or 2D linear subspace. The result of the performance estimation is shown in Figure 2.6(a). In addition, in Figure 2.6(b,c,d), the scatter plots of mapped data with corresponding classifiers are shown.

Comparison of the results. Each weighted classification error curve (cf. Fig. 2.5 and 2.6(a)) represents a combination of a feature selection/extraction method and a classifier algorithm. For each combination, we select the lowest point value representing the best feature selection/extraction performance of the combination and, subsequently, compare the weighted error and standard deviation of each lowest point. The combination of branch and bound feature selection with k-nearest neighbor classifier has the lowest minimal value and relatively small

standard deviation, as can be concluded from Table 2.4.

Table 2.4. Minimal value of Mean Weighted Errors and its Standard Deviation

	Individual		B&B		Backward		Fisher	
	min	σ	min	σ	min	σ	min	σ
LDC	0.0586	0.0093	0.0562	0.0098	0.0534	0.0109	0.0555	0.0105
QDC	0.0609	0.0119	0.0626	0.0117	0.0815	0.0113	0.0589	0.0125
KNNC	0.0502	0.0092	0.0450	0.0091	0.0535	0.009	0.0587	0.0124

The three selected features, derived from branch and bound feature selection with the best performance, are closest object dist, object intensity and area. The closest object dist is a distance measurement between an object and its nearest neighbor. It defines the local numerical density of an object. The cluster and vesicle categories usually have a much lower closest object dist since they tend to appear in clusters. The amount of fluorescence therefore directly relates to the amount of EGFR and can be measured as intensity at a certain spot. We suppose that plasma-membrane, vesicle or cluster are all composed of EGFR and the expression of EGFR is more evenly distributed in the plasma-membrane and gradually increases concentration in vesicle and cluster. Intensity represents the amount of EGFR and is significant. Size is undoubtedly the major feature for describing three characteristic episode groups. The results confirm our expectations. We have chosen the combination of branch and bound feature selection with k-nearest neighbor classifier as the best classifier for the case studies.

Statistical Analysis. We provide two case studies in order to sustain the performance of our solution. The first case study is aimed at a better understanding of EGFR endocytosis across time series. The EGFR endocytosis procedure is as follows: in the absence of EGF, EGFR localizes at the cell membrane (e.g. cell border localization). Upon EGF exposure, a portion of the plasma membrane containing EGFR is invaginated and pinched off forming a membrane-bounded vesicle. Some vesicles would be accumulated in clusters in the peri-nuclear region. As for the experimental design, the cells in separate wells are treated with EGF for a variable amount of time. In this way each well represents a fixed time point. After fixation, cells are stained and visualized. The images that have a clear representation of phenotype stage are carefully selected by a specialist. The result of

image and data analysis based on selected images provides a notable capability of our solution on identifying the dynamics in the characteristic episodes. The source images include a total of 13 time points with 2 pairs of images each.

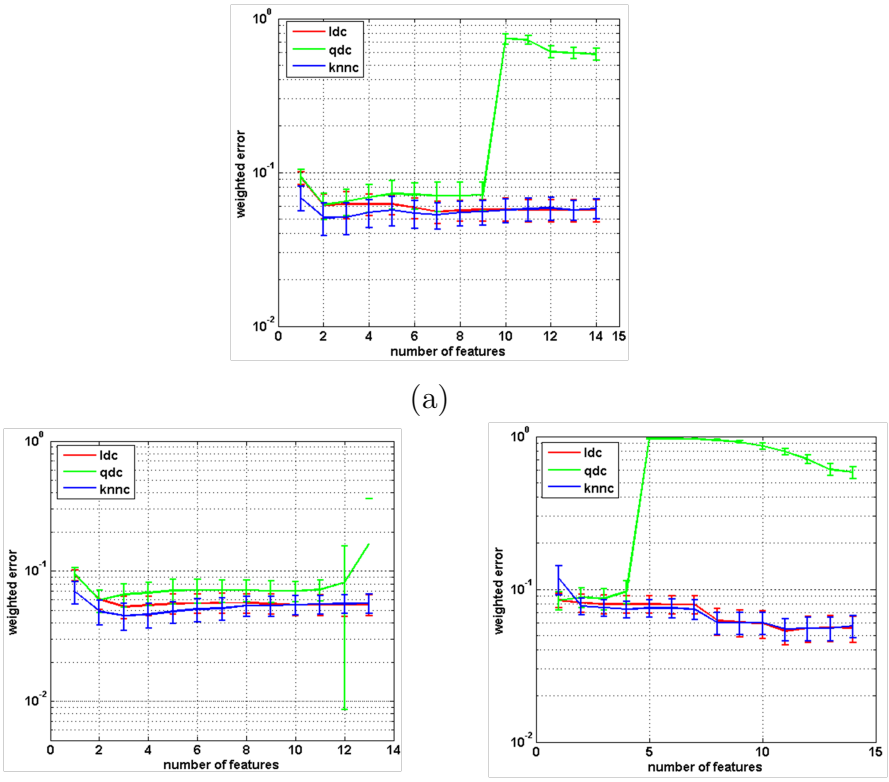

Figure 2.5. Weighted classification error curves, with (a) Individual feature selection, (b) Branch and bound feature selection and (c) Backward feature selection.

The second case study is on identification of mediators of EGFR endocytosis. The results demonstrate that our automated high-content analysis solution can properly describe different phenotypic groups and is capable to manage large quantities of phenotypes. For each culture plate ten images are acquired per well; i.e. 9610 images are used in the image and data analysis. In order to evaluate the phenotype difference between wells, we calculate the number of each phenotypic group (vesicle, plasma-membrane, and cluster) per nucleus in each well. The plasma-membrane, representing the composed EGFR evenly distributed on the

cell membrane, is always continuously linked between cells. The quantification is accomplished by calculating the pixels of plasma-membrane per nucleus.
An analysis with both the Jarque-Bera [Bera and Jarque, 1981] and Lillie test [Lilliefors, 1969] established that over 80% of our measurement data of the composition vesicle/plasma-membrane/cluster is not normally distributed. We, therefore, use the Kolmogorov-Smrinov test [Massey, 1951a] with siCtrl#2 as control sample to identify significant changes in EGFR endocytosis.

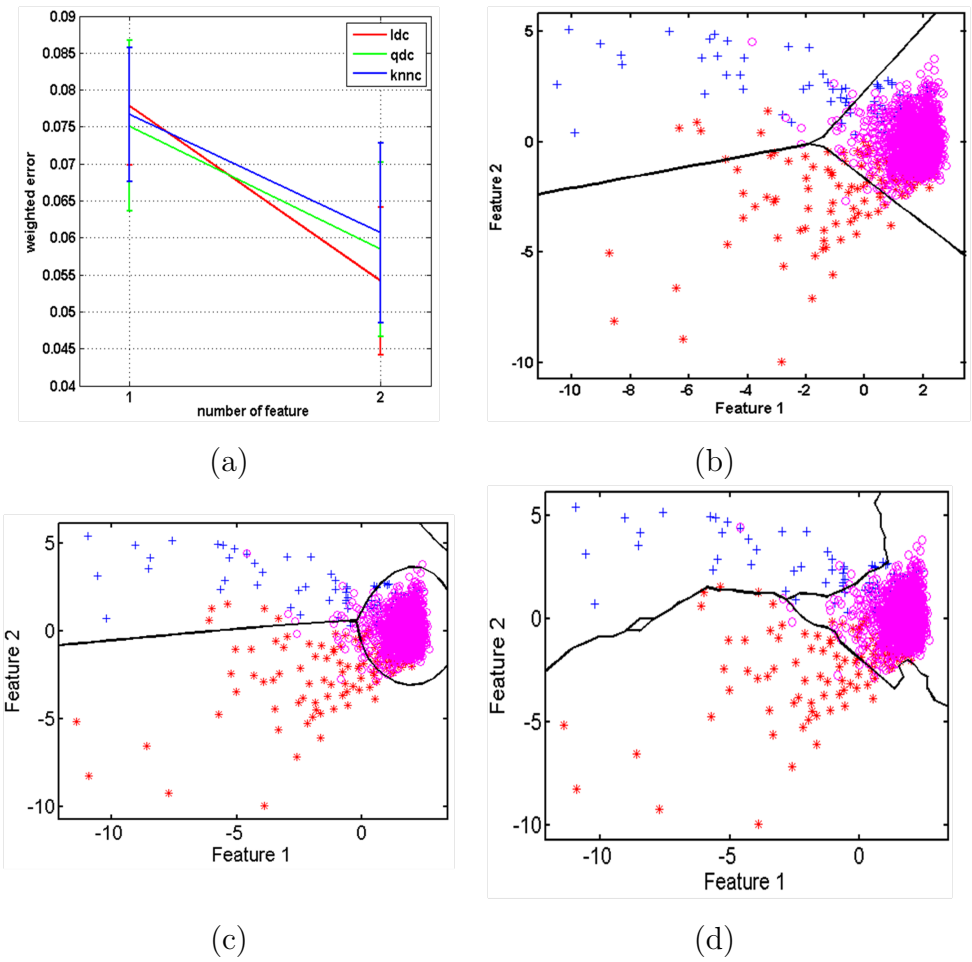

Figure 2.6. Results of feature extraction: (a) Weighted classification error curve of Fisher feature extraction, (b) Fisher feature extraction with Linear Discriminant Classifier,(c) Fisher feature extraction with Quadratic Discriminant Classifier, (d) Fisher feature extraction with K-Nearest Neighbor Classifier.

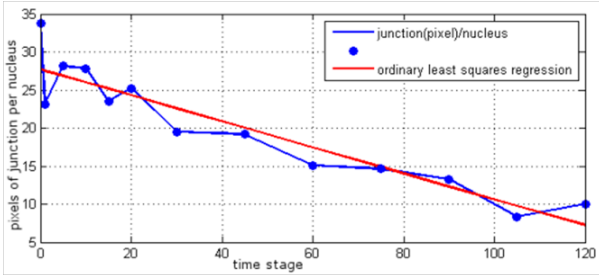

(a)

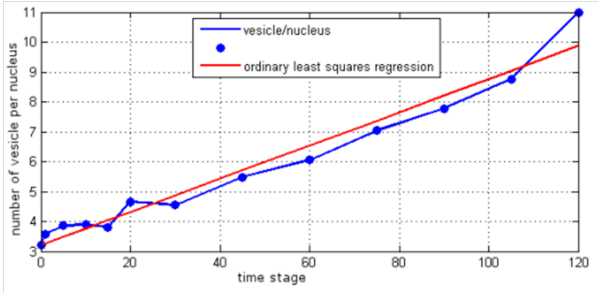

(b)

Figure 2.7. Average number of plasma-membrane (a) and vesicle (b) per nucleus.

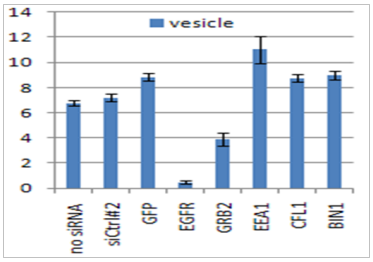

(a)

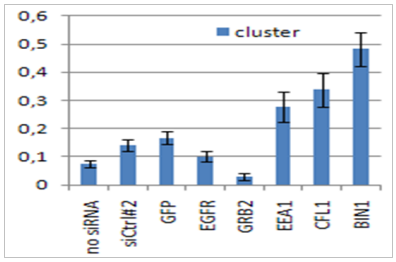

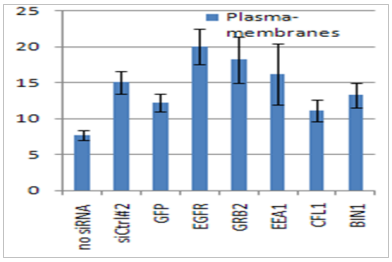

(b) (c)

Figure 2.8. (a) Number of vesicles per nucleus, (b) Number of clusters per nucleus (c) Plasma-membranes (pixel) per nucleus.

2.3 Experimental results

2.3.1 Dynamic phenotype stage

The results shown in Figure 2.7a illustrate that the amount of EGFR localized at the plasma-membrane (e.g. number of plasma-membranes, expressed as pixel/nucleus) decreases over time. This fits with the EGFR endocytosis process during which EGF exposure causes a gradual EGFR re-distribution from the plasma-membrane into vesicles. Meanwhile, the number of vesicles per nucleus increases caused by the formation vesicles as illustrated in Figure 2.7b. These graphs indicate the trend of the endocytosis process and are representative to illustrate phenotype stage dynamics.

2.3.2 Phenotype classification

We validate our automated high throughput image analysis using siRNA-mediated knock-down of several known EGFR endocytosis regulators (e.g. siGrb2, siEEA1, siCFL) To this end images are selected from WT cells (not treated with siRNA), control siRNA treated cells (siCtrl#2 and siGFP), siEGFR treated cells and three target siRNAs. In Figure 2.8a-c the comparison of selected results with three phenotypic groups is shown. In Figure 2.9 some sample images are depicted to check the correctness of our solution for phenotype description. Our analysis shows that cells treated with siCtrl#2 resemble non-treated WT cells, while siGFP differs significantly; indicating that siCtrl#2 is the best control for further analysis. The siEGFR shows decreased levels in vesicle and cluster classes since treatment of cells with siEGFR results in $> 90\%$ knock-down of EGFR. In addition, siGrb2, siEEA1 and siCFL behave as expected. These results demonstrate that the automated high throughput analysis could be used for large scale siRNA screening. A comprehensive overview of the results of a complete experiment is shown in the heatmaps depicted in Figure 2.10. The data are derived from a siRNA screening of more than 200 potential regulators of EGFR endocytosis. The y-axis represents different siRNA targets (regulators) and the x-axis represents the features plus the number of different phenotypic groups.

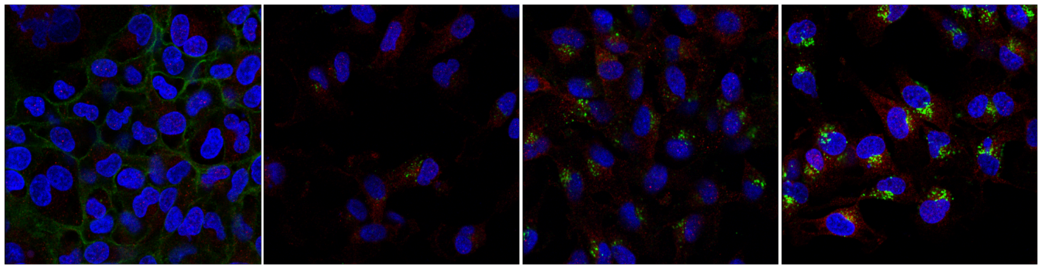

(a) (b) (c) (d)

Figure 2.9. Characteristic images with anti-body staining applied in this experiment: PERK(red), EGFR (green) and nucleus (blue). (a) no siRNA no EGF, (b) EGFR, (c) GRB2, (d) BIN1 (> response).

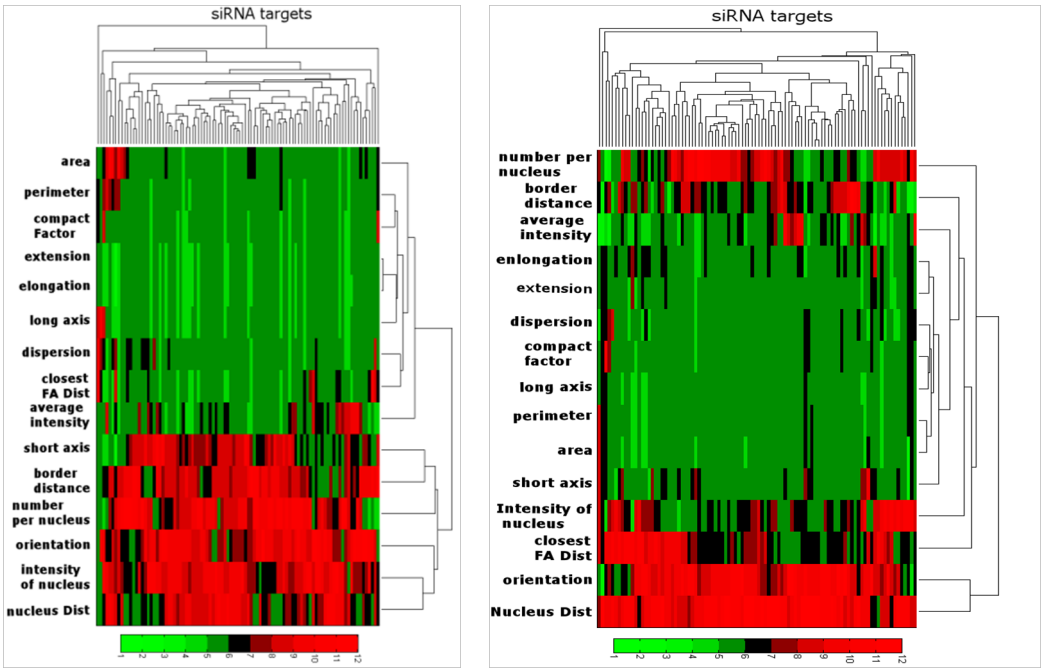

(a) (b)

Figure 2.10. (a) Vesicle p-value heat map (b) Plasma-membrane p-value heat map.

2.4 Conclusions

This paper provides an efficient solution to analyze the high-throughput image data sets on the level of protein location. The experimental results of both case

studies show that our automated analysis procedure can be involved in the identification of the characteristic episodes in the EGFR process and provides a set of robust and precise phenotypic descriptions. From the case studies it is illustrated that our solution is suitable for a robust analysis of different phenotypes in a siRNA based HTS. Furthermore, the whole process, from image segmentation, phenotypic quantification to classification, is part of a successfully automated procedure. Our solution can be easily extended to cope with studies utilizing fluorescence microscopy.

Chapter 3

Hierarchical classification strategy for Phenotype extraction from epidermal growth factor receptor endocytosis screening

Based on:

L. Cao, M. de Graauw, K. Yan, L. Winkel, F.J. Verbeek. Hierarchical classification strategy for Phenotype extraction from epidermal growth factor receptor endocytosis screening. Journal of BMC bioinformatics, 2013 (submitted)

M. de Graauw, L. Cao, L. Winkel, M. H.A.M. van Miltenburg, S. E. le Dévédec, M. Klop, K. Yan, C. Pont, V. M. Rogkoti, A. Tijsma, A. Chaudhuri, R. Lalai, L. Price, F.J. Verbeek, B. van de Water. Annexin A2 depletion delays EGFR endocytic trafficking via cofilin activation and enhances EGFR signaling and metastasis formation. Oncogene, pages 1-10, 2013

Abstract: Endocytosis is regarded as a mechanism of attenuating the epidermal growth factor receptor (EGFR) signaling and of receptor degradation. There is increasing evidence becoming available showing that breast cancer progression is associated with a defect in EGFR endocytosis. In order to find related Ribonucleic acid (RNA) regulators in this process, high-throughput imaging with fluorescent markers is used to visualize the complex EGFR endocytosis process. Subsequently a dedicated automatic image and data analysis system is developed and applied to extract the phenotype measurement and distinguish different developmental episodes from a huge amount of images acquired from high-throughput imaging. For the image analysis, a phenotype measurement quantifies the important image information into distinct features or measurements. Therefore, the manner in which prominent measurements are chosen to represent the dynamics of the EGFR process becomes a crucial step for the identification of the phenotype. In the subsequent data analysis, classification is used to categorize each observation by making use of all prominent measurements obtained from image analysis. Therefore, a better construction of classification strategy will help to raise the performance level in our image and data analysis system. In this paper, we illustrate an integrated method employing wavelet-based texture measurements and a hierarchical classification strategy to further improve the recognition of phenotypic episodes of EGFR during endocytosis. Different strategies for normalization, feature selection and classification are evaluated. The performance estimation results show that our hierarchical classification scheme combined with wavelet-based texture measurements provides a notable improvement in the temporal analysis of EGFR endocytosis. The scheme could be further applied for the drug discovery to constrain the defect EGFR endocytosis process.

3.1 Background

The epidermal growth factor receptor (EGFR) is important for normal growth and function of breast tissue. Its signaling is regulated via endocytosis, a process that results in receptor degradation and thereby attenuation of EGFR signaling. In cancer cells, however, the endocytosis pathway is often found to be defective, resulting in an uncontrolled EGFR signaling. These enhanced EGFR signaling triggers breast cancer cells to escape from the primary tumor and spread to the lung, resulting in a poor prognosis for the disease progression. Moreover, it may result in complications like resistance to anti-cancer therapy.
From the literature [Geldner and Jürgens, 2006] a generic model of epidermal growth factor induced (EGF-induced) EGFR endocytosis can be distilled into four characteristic episodes. (1) Under normal conditions, EGFR is localized at the plasma-membrane site for internalization; this is in our study defined as the "plasma-membrane" episode. (2) Upon binding of EGF to the receptor, EGFR is taken up into small vesicular structures and starts sorting in early endosomes; in our study this is defined in our study as the "vesicle" episode. (3) Over time, EGFR containing vesicles are transported to late endosomes localized near the nuclear region and these form into a larger complex multi-vesicular body; in our study this defined as the "cluster" episode. (4) In final episode, EGFR is degraded in the lysosomes. In addition to this route, EGFR can also be partly transported back to the plasma-membrane sites. Using this dynamic model as the major guideline, the analysis of the EGFR-regulation-related genetic pathway could be linked to the analysis of the characteristic episodes in EGFR endocytosis. In this paper, we will focus on the analysis of this dynamic model but only the first three characteristic episodes as shown in Figure 3.1, since, in the final episode the EGFR signaling can not be traced.
Over the past years, RNA interference in combination with fluorescence microscopy-based imaging has become a powerful high-throughput tool for the visualization of complex EGFR endocytosis processes [Goldoni et al., 2006; Muniz Feliciano et al., 2013; Rappoport and Simon, 2009]. With these techniques, it becomes feasible to distinguish characteristic episodes and identify potential EGFR endocytosis regulators. However, it is impossible to perform manual processing of

such a large volume of image data. This requires an automated method for the analysis of EGFR endocytosis [de Graauw et al., 2013].

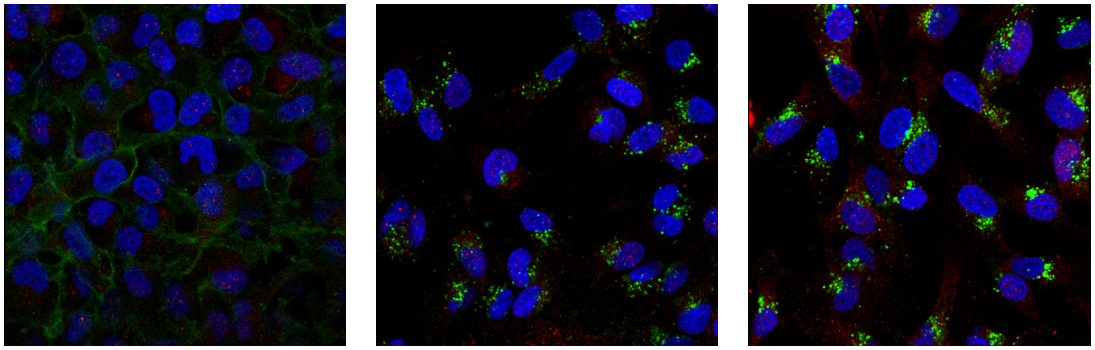

(a) (b) (c)

Figure 3.1. Sample images of the 3 phenotypic groups: (a) Plasma-membrane, (b) Vesicle and (c) Cluster. Red channel is P-ERK expression staining (Cy3); green channel is EGFR expression staining (Alexa-488); blue channel is nuclear staining (Hoechst #33258).

In the solution presented here, a single-step multi-class classification solution is demonstrated to properly capture the EGFR dynamics which transforming along three characteristic episodes and classify different EGFR episodes. From earlier application we have identified some weaknesses require better solutions. First, the same subset of features is used to classify three episodes. Second, the flat classification ignores the existence of potential hierarchical relationships that may exist in the data set. Another shortcoming is including the average intensity in the phenotype measurements. A variation of fluorescent intensity in image datasets is always presented. Thus, a more advanced classification strategy is required.
For our observation from previous results, we found the vesicle and cluster have more morphological similarity with each other than with plasma-membrane episode. As a result, we designed a new hierarchical classification strategy [Silla and Freitas, 2011]. Hierarchical classification strategies are an efficient way to deal with complex classification problems. First of all, the problem is divided in an hierarchical manner where classes with higher similarity to each other are grouped together into a sub-class, resulting in a simplification of original problem [Kumar et al., 2002]. Each parent node in the hierarchical tree has an individual classifi-

cation scheme choosing related features and the best classifier to distinguish the child nodes. Specifically, this hierarchical classification strategy separates classifier training into two levels. For the first level, we train the first level a local classifier to distinguish the plasma membrane from endosome, the subgroup containing vesicle and cluster. Subsequently, we train a second level local classifier to separate vesicle from cluster. With this strategy, we can make use of prominence in the subsets of features and thereby improve the performance of the classifier noticeably. Meanwhile, instead of using average of intensity directly, we introduce a set of texture measurements including those from wavelet transform to describe the intensity characteristics in a more sophisticated way.

3.2 Methods

3.2.1 Cell material and preparation

The study of cell systems at the cellular level at large scale is called cytomics. The workflow for image data preparation in cytomics includes three essential steps: (1) cell culturing, (2) labeling, preparation for imaging and (3) image acquisition. In this paper we use a workflow of an EGFR-regulation related siRNA screening to illustrate this workflow. In this design, breast cells from human breast carcinoma cell line (HBL100) were cultured in 96 well culture plate and transfected using Dharmafect smartpool Small interfering RNAs (siRNAs). Subsequently, the transfected cell population was exposed to epidermal growth factor (EGF) for a specific duration of time. Cells were fixed at different time points and visualized as confocal slice with a confocal laser microscope (Nikon TE2000).

3.2.2 Image acquisition and processing

Automated image acquisition was realized with a controlled motion stage equipped with an auto-refocusing module. For each well, images were captured from ten randomly selected locations. For each image three channels were captured: (1) a red channel containing staining of Phospho-ERK(P-ERK) expression (Cy3), (2) a green channel containing EGFR expression staining (Alexa-488) and (3) a blue

channel containing a nuclear staining (Hoechst #33258).
The subsequent image processing consists of two major steps: noise suppression and image segmentation. Image segmentation refers to the process of partitioning an image into multiple regions with the goal to simplify and/or change the representation of an image into comprehensive components. For fluorescence microscopy cell imaging, we utilized a customized segmentation algorithm known as the watershed masked clustering (WMC [Yan and Verbeek, 2012a]). The WMC algorithm is an innovative segmentation algorithm that is particularly suitable for images in which the individual objects exhibit a variation in fluorescence. The WMC algorithm serves different types of cytomics studies like dynamic cell migration analysis [Roepstorff et al., 2008; Yan et al., 2009b] and protein signaling modeling [Qin et al., 2012a]. Output binary mask was used to derive a number of phenotypic measurements for further data analysis.

3.2.3 Phenotype measurement

A phenotype is considered as the composite of an organism's observable characteristics or traits: such as its morphology or development (cf Chapter 1). It is important for the detection of genetic variants in complex traits. Therefore, researchers should be aware of the theoretical importance of unbiased, reliable and replicable measurements [Johannsen, 1911]. In our previous work, we have already introduced amount of basic measurements and localization phenotype measures [Cao et al., 2011]. In order to attempt finding more prominent phenotype measurements to characterize the three EGFR phenotypes, two aspects were considered. On the one hand, the phenotype measurements should be representative and relevant. On the other hand, these measurements must be robust to small variations in fluorescent intensity, meaning that the measurements are scale-free and self-normalized.
Based on the empirical observations in a ground truth data set, several potential texture patterns in object intensities were identified to characterize EGFR episodes. For instance, the vesicle (1st episode) has a higher intensity in the central region and relatively lower intensity around the boundary. In contrast, the cluster episode (2nd episode) has a more evenly distributed intensity throughout

the region of interest. In addition, these three EGFR episodes could also present distinctively in different texture features. Therefore, we introduced several texture measurements to describe different phenotypical characteristics.

3.2.3.1 Texture measurement

Table 3.1. Phenotype measurements description

Feature Name	**Expression**	**Description**
std	$f_1 = \sqrt{\sum_i (i - mean)^2 H(i)}$	The standard deviation of intensity from all the pixels in a region.
Smoothness	$f_2 = 1 - \frac{1}{(1+f_1^2)}$	The relative smoothness of the intensity in a region. It is 0 for a region of constant intensity and 1 for a region with large excursion in the values of its intensity levels.
Skewness	$f_3 = \sum_i (i - mean)^3 H(i)$	The order moment about the mean. The departure from symmetry about the mean intensity. It is 0 for symmetric histograms, positive for histograms skewed to the right and negative for histograms skewed to the left.
Uniformity	$f_4 = \sum_i H^2(i)$	The sum of squared elements in Histogram. It reaches maximum when all intensity levels are equal and decreases from there.
Entropy	$f_5 = -\sum_i H(i) \log_2 H(i)$	The statistical measure of randomness.
i represents the intensity value. H(i) is the histogram of intensity. mean symbolizes the average intensity.		

The most frequently used approach for texture measurements are the First Order Statistics; these are derived from statistical properties of the intensity histogram

of an image [Bountris et al.]. We used standard First Order Statistics for each individual object as obtained from the segmentation; i.e. standard deviation of intensity, smoothness, skewness, uniformity and entropy. Definitions and formulations of these texture measurements are presented in Table 3.1.

3.2.3.2 Wavelet texture measurement

Table 3.2. Wavelet texture measurements

Feature Name	**Description**
H_mean	The average intensity of Horizontal detail from discrete wavelet transformation.
H_std	The intensity variation of Horizontal detail from discrete wavelet transformation.
H_Entropy	The statistical randomness of Horizontal detail from discrete wavelet transformation.
V_mean	The average intensity of Vertical detail from discrete wavelet transformation.
V_std	The intensity variation of Vertical detail from discrete wavelet transformation.
V_Entropy	The statistical randomness of Vertical detail from discrete wavelet transformation.
D_mean	The average intensity of Diagonal detail from discrete wavelet transformation.
D_std	The intensity variation of Diagonal detail from discrete wavelet transformation.
D_entropy	The statistical randomness of Diagonal detail from discrete wavelet transformation.

Recently, texture analysis based on the discrete wavelet transform (DWT) has shown to be feasible [Goldoni et al., 2006; Tsiaparas et al., 2012] as it turns out to be an efficient descriptor for phenotyping [Materka, 2001]. DWT provides a set of texture representations consisting of coefficients in different directions. We calculated our wavelet-based texture measurements by multiplying each direc-

tion detail with the binary mask obtained from the segmentation and calculating the mean, standard deviation and entropy of intensity for each labeled object in each direction details (see in Table 3.2). In this study, we include a biorthogonal wavelet because it has the property of exact reconstruction and it is an outstanding wavelet representation for image decomposition. After decomposition, it generated the coefficient matrices of the level-one approximation and horizontal, vertical and diagonal details. Subsequently, we reconstructed the level-one details respectively from the corresponding coefficients. In this way, we derived the texture details from three different directions on the same scale as the original image.

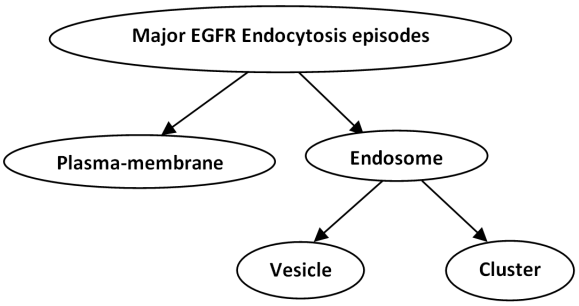

Figure 3.2. Hierarchical tree of EGFR Endocytosis Process.

3.2.4 Production of ground truth data

Collecting objective and sufficient ground truth data is important for supervised classification. We use the ground truth data as our training set during the classifier training.

Ground truth data were obtained by outlining the three characteristic episode groups, i.e. plasma-membrane, vesicle and cluster. These were separately drawn by biologists using our annotation software (TDR) with a digitizer tablet (WACOM, Cintiq LCD-tablet)[Verbeek and Boon, 2002]. From each outline a binary mask was created for each phenotypic stage. The Figure 3.4(b) illustrates the vesicle mask derived from a manually selected vesicle outline. This mask was multiplied with the mask obtained from the WMC algorithm so as to extract the intersection (cf. Figure. 3.4(d)). Finally, the phenotype measurements were computed from these masks. The ground truth datasets for the plasma-membrane

and cluster episodes were prepared in a similar manner. The training dataset included the three characteristic episode groups with a total of 2254 objects and 25 features per object.

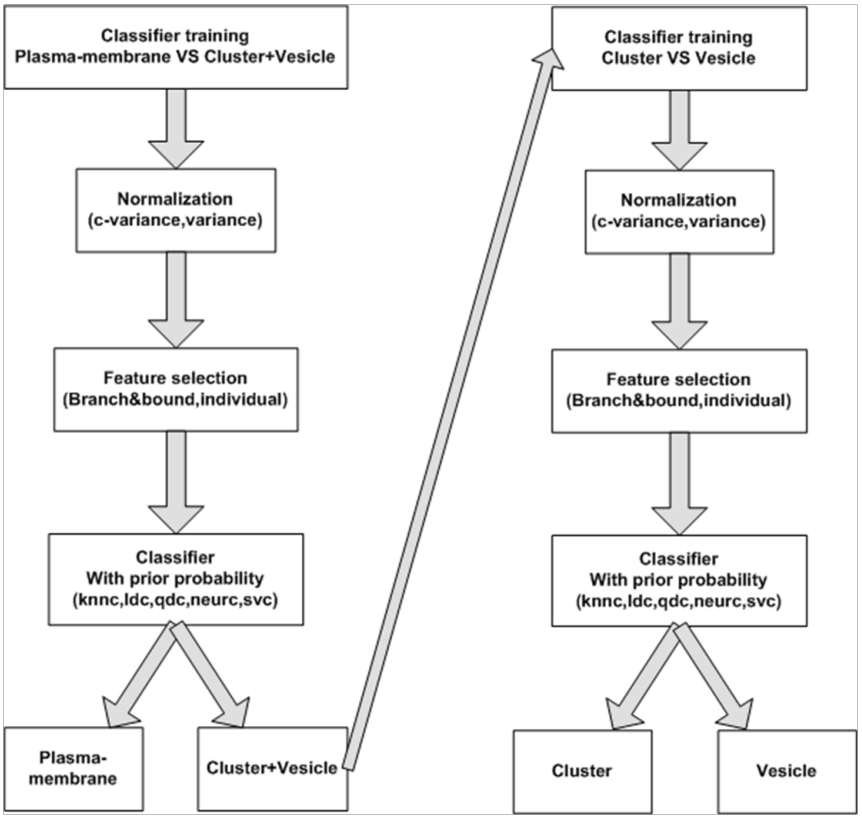

Figure 3.3. Hierarchical classification workflow.

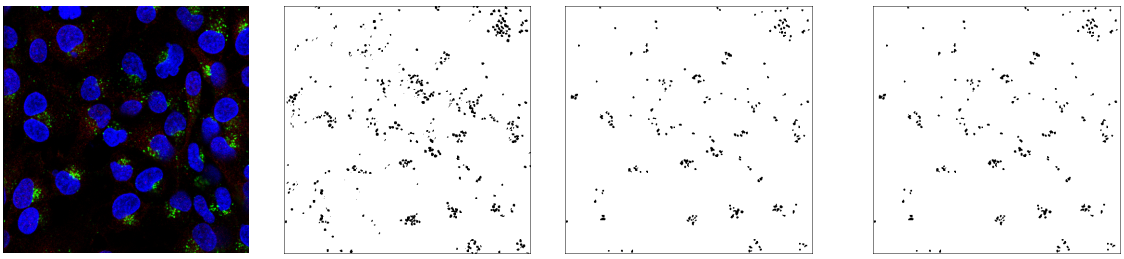

(a) (b) (c) (d)

Figure 3.4. Ground truth data production. (a) Original image, (b) Manual mask, (c) WMC mask, (d) Multiply b and c.

3.2.5 Hierarchical classification strategy workflow

On the basis of first three characteristic episodes of the generic model of epidermal growth factor induced EGFR endocytosis, vesicle is single/early endosomes and cluster is clustered/late endosomes. These two episodes have more morphological similarity with each other compared to plasma-membrane. The vesicle and cluster episodes are located in the cytoplasma which have evenly distributed high intensity value and relatively circular shape. The plasma-membrane episode is located around cell membrane which has an elongated shape with a low and unevenly distributed intensity value. Therefore, we have constructed the three characteristic episodes into a hierarchical tree as shown in Figure 3.2. Subsequently, we use a local classifier per parent node approach to train a multi-class classifier for each parent node in the class hierarchy. From this approach one avoids the problem of making inconsistent predictions and takes into account the natural constrains of class membership [Davies et al., 2007; Neuwald et al., 2012; Silla and Freitas, 2011]. In this manner, both the best classifier and the most prominent features are selected for each parent node classifier so as to classify the dynamic model with three episodes in a better fashion. The workflow of the hierarchical classification strategy is shown in Figure 3.3. In our workflow, we normalized the dataset per feature, performed the feature selection, applied the classifier and calculated the weighted classification error in order to evaluate the performance of the classification. We look for the best combination of classification process according to the error estimation and use it for EGFR episode classification.

3.2.5.1 Feature normalization

The features can have a quite substantial difference in their dynamic range. Such is the case with the features that we use in this setup. Therefore, it is necessary to normalize our dataset. Feature normalization is required to approximately equalize ranges of the features and make them have roughly the same effect in the computation of similarity [Aksoy and Haralick, 2001]. The main advantage of normalization is to avoid attributes with larger numerical ranges to dominate over those with smaller numerical ranges. Another advantage is to avoid numeri-

cal complications during the computations. Because kernel values depend on the inner products of feature vectors, large attribute values might introduce numerical complications [Hsu et al., 2010].
We applied two types of normalization schemes to normalize the dataset. One standard normalization scheme was accomplished by shifting the mean of the dataset to the origin and scaling the total of variance for all features to 1, thereby, neglecting class priors. The other scheme was achieved by shifting the mean of the dataset to the origin and normalizing the average class variances (within-class). Class priors were taken into account. The concept of within-class covariance normalization for support vector machines (SVM) classifier was recently introduced [Hatch et al., 2006]. For the evaluation of the methods considered in this paper, we are evaluating these two normalization schemes and we are interested to see whether, in our case, within-class covariance normalization outperforms the standard normalization. We will benefit from the fact that the normalization avoids differences in numerical scales.

3.2.5.2 Feature selection

After normalization, we applied feature selection procedure. We did not use the supervised linear feature extraction method because of the limitation that the number of extracted features can, at most, be one less than the number of classes. Therefore, no more than this number of new features can be obtained. In our case, for each hierarchical step we can map all the features into a 1D linear subspace since we simply have two classes for each step. It would cause difficulties in the discrimination between two classes [Shadvar and Erfanian, 2010]. Furthermore, in our study, the feature extraction method is not outstanding as feature selection method compared to [Cao et al., 2011].
For feature selection a metric is required that considers strong correlation among the variables, therefore, the Mahalanobis distance [Mahalanobis, 1936b; Webb and Copsey, 2011] was chosen. Subsequently we selected two representative search algorithms: the branch and bound procedure [Land and Doig, 1960b] and best individual-N features. Branch and bound is a top-down procedure, beginning with the set of variables and constructing a tree by successively deleting vari-

ables. This feature selection method showed a robust and high performance in our previous study [Cao et al., 2011]. Best individual-N features procedure is a computationally efficient method for choosing the best N features by assigning a discrimination power estimate to each of the features in the original set. This method could have a well-defined feature set when the features are uncorrelated. We would use these two search algorithms in the feature selection part.

3.2.5.3 Prior probability setting

In probability theory and applications, the Bayes' theorem shows the relation between a conditional probability $P(A|B)$ and its reverse form $P(B|A)$, expressed as:

$$P(A|B) = \frac{P(B|A)P(A)}{P(B)}$$

Table 3.3. Prior probability comparison

C-variance(branch&bound)										
equal prior	knnc		ldc		qdc		neurc		svc	
	mean	std	mean	std	mean	std	mean	std	mean	std
1st step	0.0333	0	0.095	0.0224	0.0317	0.0075	0.0633	0.0149	0.0333	0
2nd step	0.0575	0.0335	0.0575	0.0335	0.15	0	0.055	0.0224	0.1025	0.0112
no prior	knnc		ldc		qdc		neurc		svc	
	mean	std	mean	std	mean	std	mean	std	mean	std
1st step	0.0181	0.0014	0.0365	0.0057	0.0221	0.0037	0.01	0.0031	0.0142	0.001
2nd step	0.0292	0	0.0357	0.0088	0.043	0.0121	0.0348	0.0065	0.0402	0.0069
with prior	knnc		ldc		qdc		neurc		svc	
	mean	std	mean	std	mean	std	mean	std	mean	std
1st step	0.0053	0.0011	0.0061	0.0038	0.0059	0.0028	0.0061	0.0029	0.0061	0.0038
2nd step	0.0214	0.0031	0.0321	0.0011	0.056	0.0019	0.0231	0.0048	0.0214	0.002

A prior probability P(A) is the probability distribution of A before the specific condition is taken into account [Haldane, 1948; Witten and Frank, 2005]. It means to attribute uncertainty rather than randomness to the quantity under investigation. A prior is often a purely subjective assessment of an expert. In order to obtain this prior knowledge, we chose a group of images with 6 different time stages and manually counted the number of the three characteristic

episodes. Subsequently, we calculated the ratio between plasma-membrane and the subgroup (cluster and vesicle) as 0.0526 and the ratio between cluster and vesicle as 0.0556. This ratio is ascertained by biologists through observation. In addition, we verified the performance of this prior probability with simply no prior probability and with equal prior probability. The within-class covariance normalization was selected for this optimization scheme. Subsequently, the weighted error of different classifiers was calculated after branch and bound feature selection. The results in Table 3.3 show that the performance is increased when the prior probability is included.

3.2.5.4 Classifier

The classifiers were selected on their ability to cover both linear and non-linear categories; i.e. the linear classifier (LDC), the quadratic classifier (QDC), the k-nearest neighbor classifier (KNNC), the support vector machine classifier (SVC) and the neural network classifier (NEURC). The linear classifier makes a classification decision based on the value of a linear combination of the characteristics [Mitchell, 1997]. Compared to nonlinear classifiers, the performance of linear classifier is less preferred in data that are strongly non-Gaussian distributed [Devroye et al., 1996]. The quadratic classifier is generalized form of the linear classifier that separates classes on the basis of a quadratic hyperplane. The k-nearest neighbor classifier distinguishes an object by majority voting of its neighbors, with the object being assigned to the class most common amongst its neighbors. The Support Vector Machine (SVM) is primarily a classifier method that performs classification tasks by constructing hyperplanes in a multidimensional space that separates cases of different class labels. [Cortes and Vapnik, 1995] Key to the SVM is the use of kernels, the absence of local minima, the sparseness of the solution and the capacity control obtained by optimizing the margins [Cristianini and Shawe-Taylor, 2000].
In a neural network, units (neurons) are arranged in layers and these layers convert an input vector into some output. Each unit takes an input, applies a (often nonlinear) function to it and then passes the output on to the next layer [Zhang, 2000]. There are many artificial neural network (ANN) models; i.e., Feed-Forward

Networks, Radial Basis Function Networks, Recurrent Networks, etc. The advantage of neural networks is two-fold. First, neural networks are data driven self-adaptive methods. The flexibility is created by the combination of different nodes with related kernels. Second, they are universal functional approximators in which neural networks can approximate any function with arbitrary accuracy. The disadvantage of neural networks is that they are notoriously slow and is very difficult to determine the optimal number of kernel types, layers and nodes [SangitaB and Deshmukh, 2011]. In this study we used the biologically inspired feed-forward neural network with a single hidden layer. The feed-forward neural network is defined as a unit feeding its output to all the units in the next layer, but there is no feedback to the previous layer. It is the simplest form of artificial neural network and it can yet limit the complexity of network calculation.

3.2.5.5 Analysis

In order to find a panel of classifiers to address the categorization of our dynamic model with three episodes, we included two normalization schemes, two feature selection methods and five classifiers. We have presented the results of a weighted error estimation. The classification are the results of a weighted error estimation procedure as implemented in PRTools [Duin et al., 2007]. The results are depicted in Figure 3.5, 3.6. For the first classifier training (plasma-membrane vs. subgroup of cluster and vesicle), we observe in Figure 3.5, the weighted error of the linear classifier increases abruptly when the number of features exceeds a certain threshold (three for branch and bound and eight for individual feature selection method). The weighted error of the k nearest-neighbor classifier, however, is more stable and equals the lowest point in the branch and bound feature selection group. As for the second classifier training (cluster vs. vesicle), we noticed, in Figure 3.6, the weighted error of quadratic classifier performs worst. We created scatter plots of mapped data with a linear classifier and a quadratic classifier so as to indicate the reasons of the worst performance with the quadratic classifier; depicted in Figure 3.7. The error line of the support vector machine classifier shows quite stable; it obtains the lowest values in the group of branch and bound feature selection method. Nevertheless, in the individual feature se-

lection group, the error of neural network classifier always evaluates as the best performance in terms of magnitude of the error.
For a global observation, we selected the minimal mean error from all weighted error with different feature dimensions. This value represents the best performance of the combination between feature selection and classifier. In Table 3.4, the standard deviation of each minimal mean value is shown. The combination of branch and bound feature selection with k-nearest neighbor classifier has the lowest minimal value and relatively small standard deviation for the first classifier training with both normalization schemes. For the second classifier training, both the combination of branch and bound feature selection with support vector machine classifier and the combination of individual feature selection with neural network classifier have the same lowest minimal value and comparatively small standard deviation in two normalization schemes. In order to make a final combination more general and with a lower feature dimension, we choose the combination of branch and bound feature selection with k-nearest neighbor classifier for first step classification with variance normalization scheme. For the second step, the combination of branch and bound feature selection with support vector machine classifier is chosen with variance normalization scheme. The reason for the selection of branch and bound feature selection method is the existence of correlated features on our feature set which causes the low performance of the best individual-N feature selection method. The branch and bound feature selection method guarantees the optimal feature subset without explicitly evaluating all possible feature subsets because the criterion function fulfils the monotonicity condition [Somol et al., 2004]. The K-nearest neighbor classifier as the selection of the first step is a simple but efficient classifier for the basic recognition problem such as two classes classification problem. On the other hand, a higher value of K provides smoothness which reduces the vulnerability to noise in the training data. For the second step, support vector machine is selected for its flexibility in threshold choosing since its function is non-parametric. Additionally, support vector machine has the ability of maximizing the generalization because it is trained to maximize the margin.

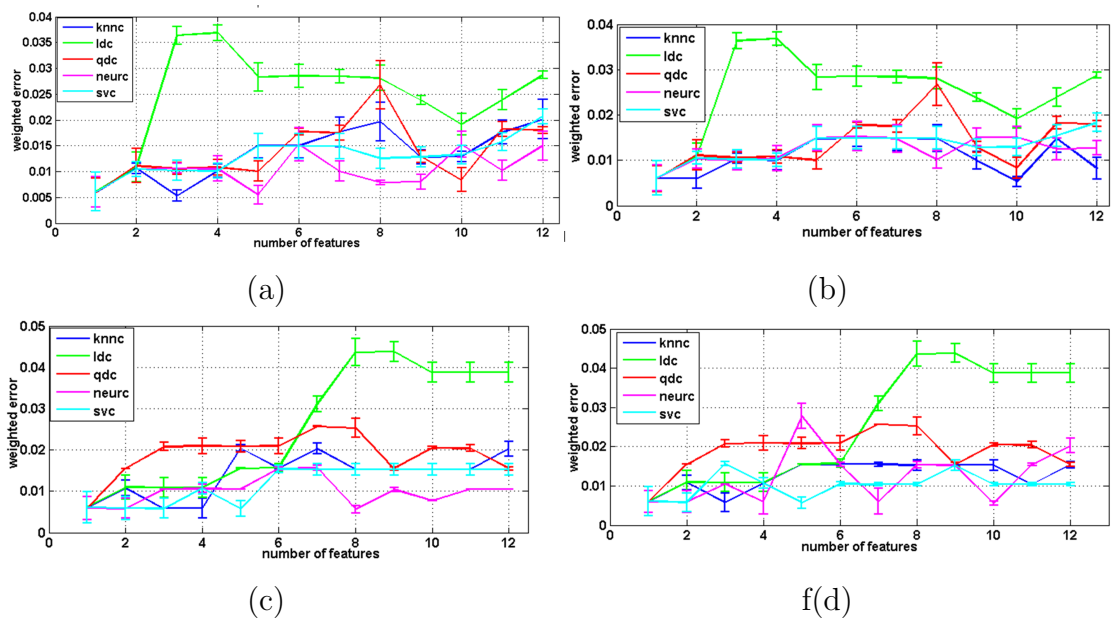

Figure 3.5. First classifier training (plasma-membrane VS subgroup of cluster and vesicle). (a) Branch&bound feature selection method with standard variance normalization (b) Branch&bound feature selection method with within-class variance normalization (c) Individual feature selection method with standard variance variance normalization (d) Individual feature selection method with within-class variance normalization.

The prominent features we choose for the first step are long axis, D-entropy and standard deviation of intensity. For the second step we choose the top five features; i.e. skewness, entropy, H-entropy, closest object Dist, area. The evaluation of the feature selection performance is shown in Table 3.5. We do the evaluation by calculating the probability of each feature being selected by the feature selection method. These highly selected features reflect the phenotype changes between three characteristic episodes. For example, for the step 1, Long Axis is chosen most of the time because the plasma membrane is around the membrane which tends to have an elongated shape than other two episodes. In step 2, the intensity entropy is selected because clusters have a flatter region than vesicles which results in a lower entropy value. In Figure 3.8 and Figure 3.9 scatter-plots are shown for both hierarchical steps. The evaluation results tell us that there is no relevance in using large amounts of features. Just a few will contribute to

the final results. We can also see both steps choose the wavelet texture features that we introduced in this research; these clearly resulted in a better performance compared to the previous classifier scheme.

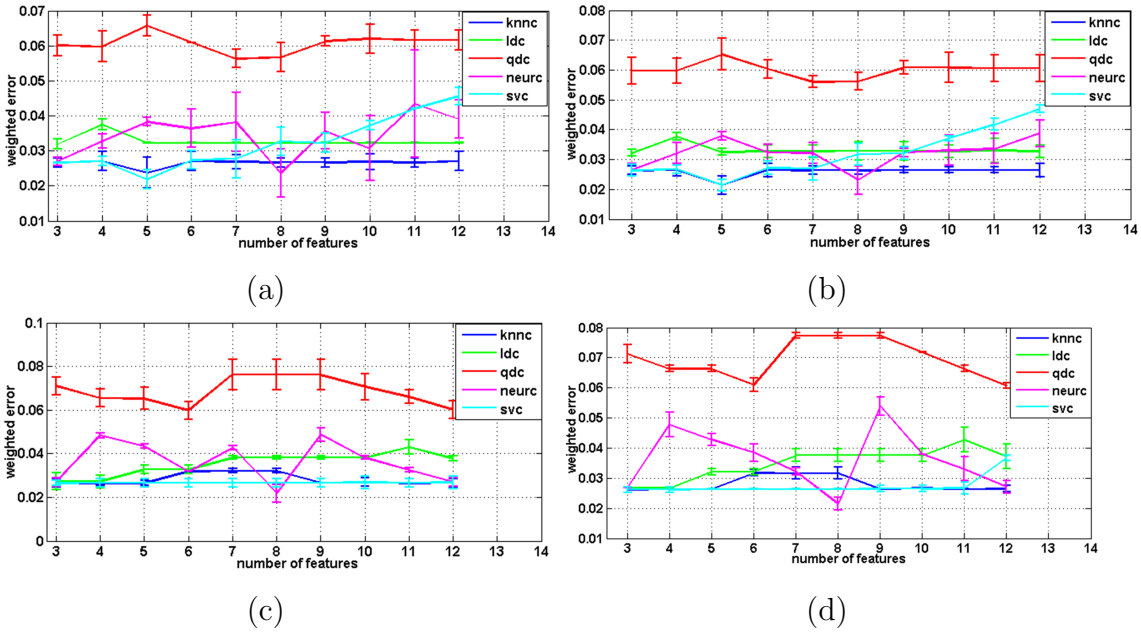

Figure 3.6. Second classifier training (cluster VS vesicle). (a) Branch&bound feature selection method with standard variance normalization, (b) branch&bound feature selection method with within-class variance normalization, (c) Individual feature selection method with standard variance variance normalization, (d) Individual feature selection method with within-class variance normalization.

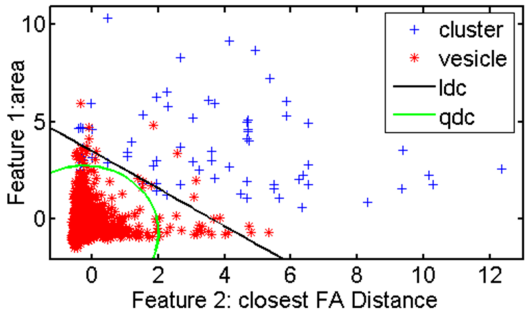

Figure 3.7. Scattered plot of training data with ldc and qdc.

Table 3.4. Weighted error comparison

1st step	knnc		ldc		qdc		neurc		svc	
C-V	mean	std	mean	std	mean	std	mean	std	mean	std
B&B	0.0053	0.0011	0.0061	0.0038	0.0059	0.0028	0.0061	0.0029	0.0061	0.0038
IND	0.0058	0.0023	0.0061	0.0038	0.0059	0.0028	0.0055	0	0.0057	0.0014
2nd step	knnc		ldc		qdc		neurc		svc	
C-V	mean	std	mean	std	mean	std	mean	std	mean	std
B&B	0.0214	0.0031	0.0321	0.0011	0.056	0.0019	0.0231	0.0048	0.0214	0.002
IND	0.0261	0	0.0267	0	0.0607	0	0.0214	0.0021	0.0261	0
1st step	knnc		ldc		qdc		neurc		svc	
VAR	mean	std	mean	std	mean	std	mean	std	mean	std
B&B	0.0053	0.0011	0.0061	0.0038	0.0059	0.0028	0.0055	0.0018	0.0061	0.0038
IND	0.0058	0.0023	0.0061	0.0038	0.0059	0.0028	0.0056	0	0.0058	0.0019
2nd step	knnc		ldc		qdc		neurc		svc	
VAR	mean	std	mean	std	mean	std	mean	std	mean	std
B&B	0.0237	0.0044	0.0319	0.0015	0.0563	0.0027	0.0236	0.0069	0.0218	0.0028
IND	0.0263	0	0.0272	0.0029	0.0598	0.004	0.0218	0.004	0.0265	0.001

C-V represents c-variance. B&B represents branch & bound. IND represents individual. VAR represents variance.

Table 3.5. Feature selection performance

Features	Step 1
Long Axis	100
Int Std	100
D_entropy	87
H_entropy	7
V_entropy	5
Smoothness	1
Area	0
Perimeter	0
Extension	0
Dispersion	0
Elongation	0
Orientation	0
Compact Factor	0
Border Dist/Nucleus Dist	0
Closest FA Dist	0
Short Axis	0
Skewness	0
Int Uniformity	0
Int Entropy	0
H_mean	0
H_std	0
V_mean	0
V_std	0
D_mean	0
D_std	0

Features	Step 2
Closest FA Dist	100
Int Entropy	100
Area	96
Int Std	73
Compact Factor	44
Int Uniformity	34
Smoothness	14
H_entropy	8
Border Dist/Nucleus Dist	7
Perimeter	6
Long Axis	6
Short Axis	5
D_std	5
Skewness	2
Extension	0
Dispersion	0
Elongation	0
Orientation	0
H_mean	0
H_std	0
V_mean	0
V_std	0
V_entropy	0
D_mean	0
D_entropy	0

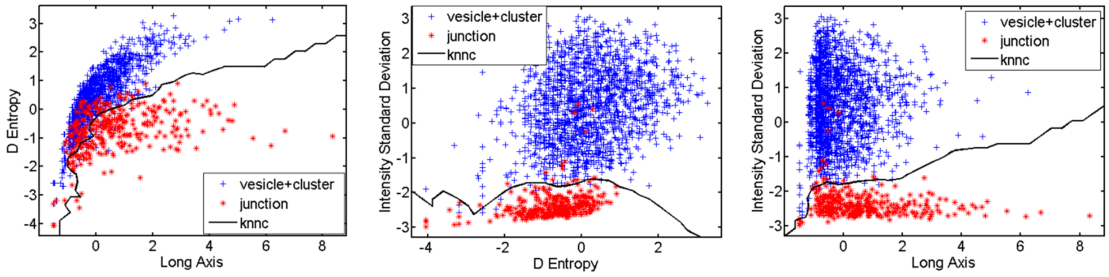

Figure 3.8. Step 1 Scattered Plot.

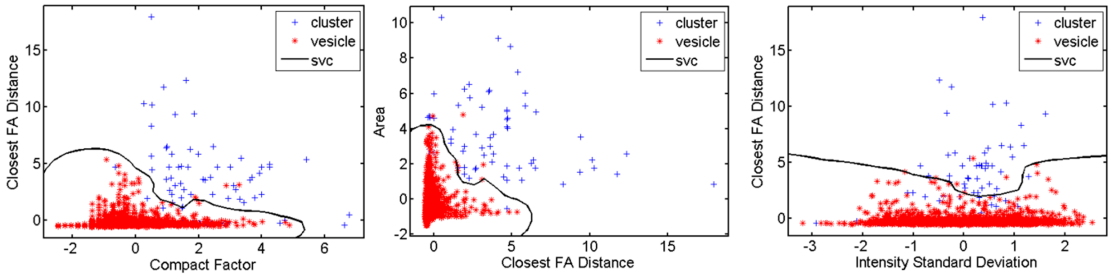

Figure 3.9. Step 2 Scattered Plot.

3.3 Results and discussion

3.3.1 EGFR endocytosis regulator identification

Our hierarchical classification strategy was used to validate siRNA-mediated knock-down of several known EGFR endocytosis regulators (e.g. siGrb2, siEEA1, siCFL). We selected 10 sample points per well from WT cells (not treated with siRNA), control siRNA treated cells (siCtrl#2 and siGFP), siEGFR treated cells and three target siRNAs. After image processing and data analysis, we calculated the number of objects belonging to each episode group per nucleus and compared the result. This is depicted in Figure 3.10. As expected, cells treated with siEGFR show a decreased level of all three classes since treatment of cells with siEGFR results in $> 90\%$ knock-down of EGFR. Cells incubated with siGrb2 show a drastic reduction in number of endosomes (vesicle and cluster) because siGrb2, as a known regulator of EGFR endocytosis, can significantly inhibit EGFR internalization [Jiang et al., 2003]. In general the increase in number of endosomes

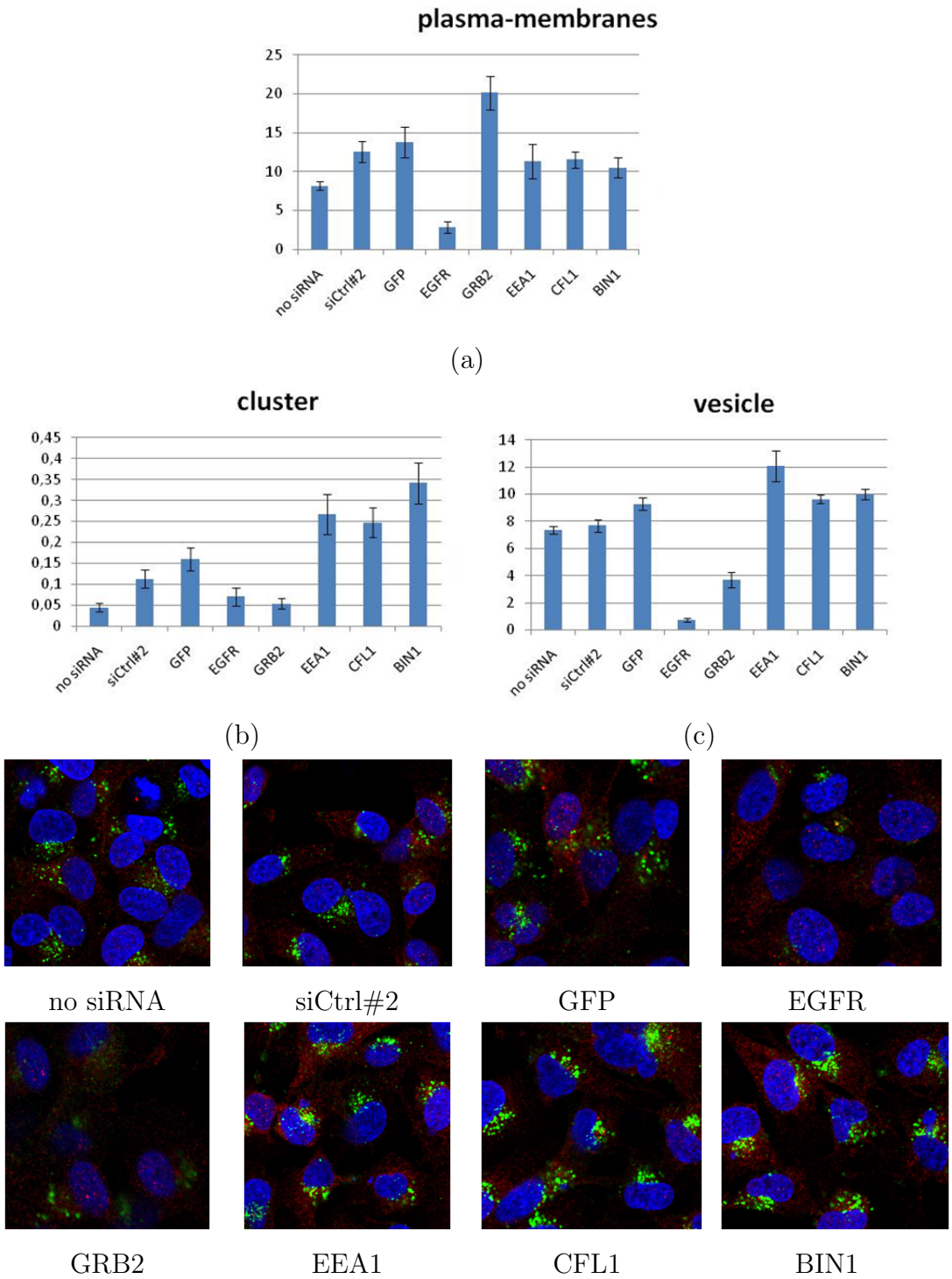

Figure 3.10. EGFR endocytosis regulator identification results. (a) Pixels of plasma-membrane, (b) Number of clusters, (c) Number of vesicles.

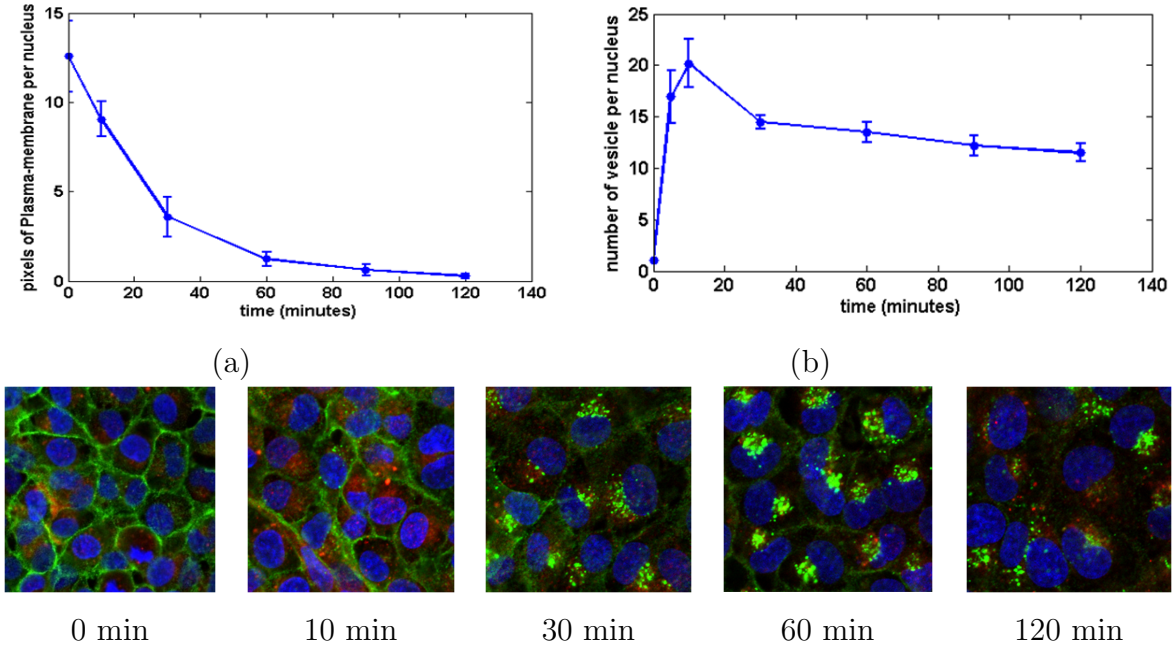

c. sample images with different time point

Figure 3.11. Dynamic stages of EGFR endocytosis. (a) Number of EGFR localized at Plasma-membrane (pixels/nucleus), (b) Number of EGFR as vesicle in early endosome (number/nucleus).

(vesicle and cluster) can be caused either by enhanced uptake of EGFR resulting in an enhanced EGFR endocytosis and EGFR degradation, or by delayed endocytosis and EGFR breakdown. For EEA1 (a member of the early endosomes), an increase in number of endosomes (vesicle and cluster) is due to delayed endocytosis [Leonard et al., 2008]. Cofilin (CFL) regulates the cytoskeleton and because of these changes in the actin cytoskeleton the endocytosis route of EGFR changes [Nishimura et al., 2006]. At present, there is not a lot of knowledge about BIN1 in EGFR endocytosis. Regarding the result, BIN1 depletion decreases EGFR at plasma-membrane, increases the number of vesicles and clusters, suggesting that it potentiates EGFR endocytosis and possibly signaling. These results demonstrate the robustness of our hierarchical classification scheme and the capability to predict new EGFR endocytosis regulators.

3.3.2 Dynamic EGFR endocytosis stage

In this case study, HBL100 cells were exposed to EGF (50 ng/ml) for indicated timepoints (Figure 11c). The number of EGFR localizations at the plasma-membrane and the vesicles was quantified. The amount of EGFR localized at the plasma-membrane, expressed as pixels of plasma-membrane per nucleus, decreases over time as shown in Figure 11a. This fits with the EGFR endocytosis process during which EGF exposure is causing a gradual EGFR re-distribution from the plasma-membrane into vesicles. Meanwhile, the number of vesicles per nucleus increases at early endosome caused by the EGFR internalization, then decreases at the late endosome stage when the vesicles form into a larger complex clusters and degrades at the end as illustrated in Figure 11b. These graphs indicate the trend of EGFR endocytosis process and are representative in illustrating the dynamics of EGFR endocytosis stages.

3.4 Conclusions

This chapter discusses an improved image and data analysis system for High-throughput screening including texture wavelet-based measurements and a hierarchical classification strategy. Having learned from earlier results [Cao et al., 2011] we have improved the phenotype description with the new texture features and improved the classification of the characteristic episodes with an alternative classification scheme. For the image analysis we use an innovative image segmentation algorithm combined with representative phenotype measurements which include relative texture features with wavelet transform to replace the absolute intensity feature so as to decrease the impact of fluorescent intensity variation. For the data analysis part, we change from a single-step multi-class classification solution into a two step Hierarchical classification strategy to categorize three dynamic phenotypes of EGFR endocytosis process. We include two feature normalization methods, two feature selection methods and five classifiers to find the best classification strategy. After evaluation of different combinations, we have chosen the combination of branch and bound feature selection with k-nearest neighbor classifier as for first step classification after normalization of variance.

As shown in Table 3.4, the combination of branch and bound feature selection with support vector machine classifier is chosen for the second step classification after having applied the same normalization method.
With the selected combination, the classifier shows a notable improvement in distinguishing plasma-membrane from the dataset. This improvement is due to three factors. First, it benefits from the hierarchical classification scheme which introduce multilevel classifiers to deal with two subset classes at a time. Second, we introduced the exact prior probability for the classifier training which improve the performance of the classification strategy significantly. Third, the relative texture measurements show their potential to describe the phenotype characteristics.
This explicit hierarchical classification solution can identify the characteristic episodes in the EGFR endocytosis process and is helpful to find new regulators in this crucial process relating to breast cancer progression. With all kinds of phenotype measurement and flexible classifier training strategy that we introduced in this work, it is easy to detect morphological changes of phenotype and extend our solution to cope with studies utilizing fluorescence microscopy in a siRNA based high-throughput screening (HTS).

Chapter 4

Evaluation of Algorithms for Point Cloud Surface Reconstruction through the Analysis of Shape Parameters

Based on:

L. Cao, F.J. Verbeek. Evaluation of algorithms for point cloud surface reconstruction through the analysis of shape parameters. 3D Image Processing (3DIP) and Applications 2012, Proceedings SPIE Vol. 8290,Bellingham, 82900G, 2012

L. Cao, F.J. Verbeek. Analytical evaluation of algorithms for point cloud surface reconstruction using shape features. Journal of Electronic Imaging, 22 (4), 043008, October 2013

Abstract: In computer vision and graphics, reconstruction of a 3D surface from a point cloud is a well-studied research area. As the surface contains information that can be measured, the application of surface reconstruction may be potentially important for applications in bio-imaging. In the past decade, a number of algorithms for surface reconstruction have been developed. Generally speaking, these algorithms can be separated into two categories: explicit representation and implicit approximation. Most of these algorithms have a sound basis in mathematical theory. However, so far, no analytical evaluation between these algorithms has been presented. The straightforward method of evaluation has been by convincing through visual inspection. Therefore, we designed an analytical approach by selecting surface distance, surface area and surface curvature as three major surface descriptors. We evaluate these features in varied conditions. Our ground truth values are obtained from analytical shapes: the sphere, the ellipsoid and the oval. Through evaluation we search for a method that can preserve the surface characteristics best and which is robust in the presence of noise. The results obtained from our experiments indicate that Poisson reconstruction method performs best. This outcome can now be used to produce reliable surface reconstruction of biological models.

4.1 Introduction

The problem of 3D surface reconstruction from a point cloud is widely studied and we consider it as important in the field of geometric modeling and analysis of biological objects (models) that have been acquired by an imaging device; for that matter we are specifically interested in objects at the microscopic scale.
At present, a number of approaches have been introduced to represent a 3D surface. The approaches are generally classified into two categories: explicit representation and implicit approximation. The major explicit representations include parametric surfaces and triangulated surfaces. Parametric surfaces, such as B-splines [He and Qin, 2004; Pfeifle and Seidel, 1996; Pottmann and Leopoldseder, 2003; Sun et al., 2006] and Bezier patches, attempt to represent all shapes with a set of elementary shapes, i.e. super-quadratics, generalized cylinders, parametric patches, etc. These parametric surfaces can be described by only a few parameters. The reconstructed surface is smooth whilst the data set can be non-uniform. There is, however, one major drawback of parametric surfaces, which is that several parametric patches need to be combined to form a closed surface, resulting in seams between the patches.
Another explicit representation is denoted as triangulated surfaces. In this representation, all or most of the points are directly interpolated based on structures from computational geometry, such as Delaunay triangulations [Boissonnat, 1984], alpha shapes [Amenta et al., 2000], or Voronoi diagrams [Amenta et al., 1998]. The CRUST method [Amenta et al., 1998] is the first one with a provable reconstruction. The CRUST algorithm exploits the Voronoi diagram of the input-point set to reconstruct the surface. Subsequently, POWER CRUST [Amenta et al., 2001] uses a weighted Voronoi diagram to produce a water-tight surface. This algorithm, however, introduces many extra points in the output and also does not produce a triangulated surface. As an improvement to CRUST, theoretical as well as practical, the COCONE algorithm [Amenta et al., 2000] was introduced. In time this was followed by SUPER COCONE [Dey et al., 2001], TIGHT COCONE [Dey and Goswami, 2003] and ROBUST COCONE [Dey and Goswami, 2004]. Triangulated methods have a profound basis in theory and thereby a guaranteed solution, nevertheless, the implicit interpolations have a

negative effect on the sensitivity to noise. Consequently, in order to produce smooth surfaces from noisy data [Kolluri et al., 2004; Mederos et al., 2005], extensive pre- and/or post-processing is required.
The implicit approximation is based on a scheme which integrates characteristic of each point on the surface into a feature function, a.k.a. the implicit function. The implicit function can be constructed in different ways, such as local fitting, global fitting and combined fitting.
In terms of the local fitting method, Hoppe et. al.[Hoppe et al., 1992] reconstructed the surface by locally estimating the implicit function as the signed distance to the tangent plane of the closest point. In a volumetric approach Curless and Levoy [Curless and Levoy, 1996] extended the distance function approach for laser range data, in which they also derive error and tangent plane information. Another approach is to capture the local shape of the surface by adaptively subdividing the space [Ohtake et al., 2003]. Global fitting methods normally use globally supported radial basis functions as the implicit function to reconstruct smooth surfaces [Carr et al., 2003]. Radial basis functions based methods are especially useful for repairing large and irregular holes in an incomplete surface. In these methods serious difficulties are encountered in capturing sharp surface features. In combined fitting methods the advantages from both global and local fitting schemes are integrated. In a Fourier-based reconstruction scheme [Kazhdan, 2005] the Fast Fourier Transform (FFT) is used to derive a characteristic function of the solid model. The Poisson reconstruction [Kazhdan et al., 2006a] is associated with the so called ambient space rather than the data points and has a simple hierarchical structure that results in a sparse, well-conditioned system. The implicit function is derived from a Poisson equation , computing a scalar function whose Laplacian equals the divergence of the oriented point samples . All the implicit approaches are particularly convenient since they all guarantee a, so called, watertight 2-manifold surface approximation [Dey and Goswami, 2003].
A large volume of research papers is available on methods for surface reconstruction from a point cloud. A great deal of effort has been put into method design. The existence of such large number of methods makes a systematic evaluation necessary. Although error estimation is available for several methods, the evaluations are still rather inefficiently described. In most cases a rather straightforward

way of evaluation is based on visual inspection. One of the apparent reasons for the lack of more comprehensive evaluation is probably related to the amount of parameters that have to be analyzed when comparing reconstruction methods.
As indicated, we are particularly interested in applying surface reconstruction methods in the field of biology. In molecular genetics and developmental biology, the analysis of gene expression is important and requires the development of new elaborate tools for shape analysis. We are modeling the genetic markup through gene expression in relation to development and shape for the Zebrafish (Danio rerio) and the Frog (Xenopus laevis) [Verbeek et al., 1999b]; to this end, we study the development of the embryo. A surface is used as a shape descriptor and as a means to project gene expression. As for the features it holds that subtle changes in shape need to be noticed so that phenotypical changes can be understood. Therefore, the surface representation needs to be precise and robust. The source datasets that we use for the reconstruction are derived from microscopy [Verbeek, 1999a]; these are stacks of plan parallel images that are aligned as precise as possible. Surfaces are derived from specific labeled volumes in the 3D image and given the context of the application; we need to preserve these surfaces as precise as possible. Numerous contour-based surface reconstruction algorithms exist [Barequet et al., 2003; Braude et al.; Ekoule et al., 1991; Ganapathy and Dennehy, 1982; Jones and Chen, 1994; Klein et al., 2000], however, the more advanced point-based reconstruction technique will support shape analysis in a better manner and parameterization of the surface provides a good starting point. In the contour-based surface reconstruction these algorithms are increasingly used [Barequet et al., 2003]. In order to assess the surface reconstruction we need develop profound insight in the point-based reconstruction technique; i.e. we need to know which algorithm would preserve the shape characteristics best and with the highest accuracy.
In order to complete an analysis of the point bases surface reconstruction algorithms, we have selected four representative algorithms from two major classes. The quality of the surface created by the different algorithms is assessed under noise conditions and compared to known analytical values. In this paper, the point cloud models that we utilized are the sphere, the ellipsoid and the oval; these shapes resemble the early embryo and therefore are realistic as a model.

The evaluation is performed with four methods and for our experiment some related parameters will be selected in the methods evaluation. Given the number of parameters that will be assessed in the evaluation, it should be clear that this evaluation approach requires large memory resources and considerable computation time.
The remainder of this paper is organized follows. In section 4.2, we introduce and propose our evaluation methods. In section 4.3, the experimental results are presented. Finally, in section 4.4, we present our conclusions and indicate directions for our future research.

4.2 Evaluation design

In this paper, we aim at obtaining a higher level of understanding of the major reconstruction approaches currently available. To that end we have selected four representative surface reconstruction methods. Two methods are typical to the group of explicit representation, i.e. Power Crust and Robust Cocone. Two other methods are typical to the group of implicit representation and derive a surface from an implicit approximation, i.e. Fourier-based reconstruction and Poisson reconstruction. According a visual evaluation presented by Kazhdan et al.[Verbeek et al., 1999b] the latter two implicit methods perform best.
In order to make an objective assessment of the quality we will use an error estimation of surface distance, surface area and surface curvature in a comparison of the surface that results from the reconstruction to analytical descriptions of the shape. These three major characteristics of the surface are chosen because: (1) surface distance provides volumetric information of the model which is known as an important global Riemannian invariant, (2) surface area represents the shape of the surface which is a notable integral property, and (3) surface curvature is one of the critical intrinsic properties for providing information on the local shape of a surface. These three features are the paramount ones providing the geometric information of the surface model. A sound error estimation based on these three features would present us a good and objective impression of the performance of each of the surface reconstruction methods.

The point cloud models used in the evaluation are three synthetic objects i.e. the sphere, the ellipsoid and the oval. The reason for employing synthetically generated objects is that we can compute the surface area and surface curvature from the parametrical mathematical representation of these synthetic surfaces. Furthermore, it is also convenient for the calculation of surface distance between synthetic objects and reconstructed objects. Moreover, the biological models that we intend to reconstruct also portray these spherical or elliptical surface characteristics. Thus, this analytical approach supports a more thorough understanding the behavior of different reconstruction methods in the context of the intended application.

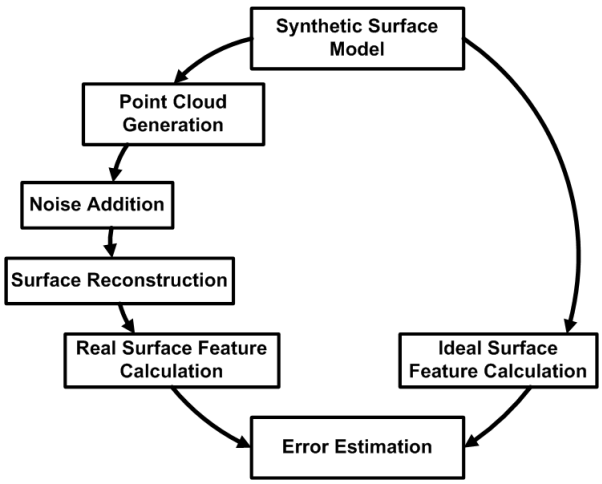

Figure 4.1. Evaluation Design Workflow.

4.2.1 Generation of points and noise

According to our observations, surface curvature differs with point location of the point on the surface, e.g. the surface curvature on the sphere is always equal while the curvature on the ellipsoid changes with spatial location. Therefore, we generate point samples for the synthetic objects in accordance with the surface curvature, so as to properly preserve the surface characteristics. For the sphere, the best way to represent its curvature is generating the surface sample points with a uniform distribution. For the ellipsoid, we generate the points sample according to the equation:

$$\frac{(x-xc)^2}{xr^2}+\frac{(y-yc)^2}{yr^2}+\frac{(z-zc)^2}{zr^2}=1, \tag{4.1}$$

Where [xc,yc,zc] represents the center of ellipsoid and xr, yr and zr denotes the equatorial radii (along the x y and z axes). In the case of the oval shape, we use the equation provided by Yamamoto [Solvenus and Yamamoto, 2011]. They treat an oval shape by rotating the oval curve around x axis. The equation of a 3D oval surface is given by the following equations:

$$\begin{cases} x = a\cos\theta \\ y = b\cos(\frac{\theta}{4})\sin\theta\cos\phi \\ z = b\cos(\frac{\theta}{4})\sin\theta\sin\phi \\ 0 \leq \theta \leq \pi \end{cases} \tag{4.2}$$

where $a = 0.5$, $b = 0.37$, $0 < \phi < 2$. With the coordinates data calculated from Equation 2, we can obtain a nicely distributed point cloud without holes existing on both poles that properly represent the surface curvature characteristic.

For the Fourier-based reconstruction and the Poisson reconstruction methods, the generation of point position as an input is not sufficient. These two methods require an oriented point-set as an input. We, therefore, apply point normal calculation as described by Hoppe et al.[Hoppe et al., 1992].

Uniformly distributed noise is added randomly on the point cloud so as to estimate the robustness of each of the methods in the presence of noise. Most of the methods are robust to the Gaussian noise, e.g. the Fourier-based reconstruction algorithm; we therefore have chosen to observe the performance of these methods using uniformly distributed noise. For this type of evaluation we consider uniformly distributed noise to be valid and meaningful.

4.2.2 Surface area calculation

Unlike the surface area of a sphere, the surface area of a general ellipsoid cannot be expressed exactly by an analytical function. The equation to approximate the surface area of an ellipse is given as:

$$A \approx 4\pi(\frac{a^p b^p + a^p c^p + b^p c^p}{3})^{1/p} \tag{4.3}$$

where a and b denote the equatorial radii (along the x and y axes), c denotes the polar radius (along the z-axis) and, according to Knud Thomsen's formula $p \approx 1.6075$.
Since the equation of oval surface can be treated as parametric surface $\overrightarrow{r} = \overrightarrow{r}(u, v)$, we thereafter make use of the definition for surface area of parametric surface to calculate the oval area. The surface area can be calculated by integrating the length of the normal vector $\overrightarrow{r_u} \times \overrightarrow{r_v}$ to the surface over the appropriate region D in the parametric uv plane:

$$A(D) = \iint_D |\overrightarrow{r_u} \times \overrightarrow{r_v}| \, dudv \tag{4.4}$$

We use the surface area equation expressed in terms of the first fundamental form as follows:

$$A(D) = \iint_D \sqrt{EG - F^2} dudv \tag{4.5}$$

where $E = \overrightarrow{r_u}.\overrightarrow{r_u}$, $F = \overrightarrow{r_u}.\overrightarrow{r_v}$, $G = \overrightarrow{r_v}.\overrightarrow{r_v}$. The expression under the square root is precisely $|\overrightarrow{r_u} \times \overrightarrow{r_v}|$, and so it is strictly positive at the regular points.
In order to estimate the error between the ideal value derived from formulas above and the real value calculated from the output model, we also need to calculate the area of the reconstructed surface. Since the output of the surface is a triangulation, we can derive the overall area by summation of all areas of the triangle patches on the surface.

4.2.3 Point distance calculation

With respect to the point distance error evaluation, we compute the distance from the points on the output triangulated surface to the synthetic surface model. It is easy to find the shortest distance from a point in 3D surface to the sphere surface centered at the origin of the coordinate system.

$$D = R_p - R_s \tag{4.6}$$

where R_p denotes the distance from point to the origin, and R_s denotes the radius of the sphere. For the ellipsoid the distance calculation is less straightforward. In the literature [Eberly, 2011] algorithms are described to compute the distance from an arbitrary point to an ellipsoid; we have adhered to this approach.
Since oval is a parametric surface, we can treat this specific problem of finding the shortest distance from a point to oval surface as a general one of projecting a point onto a parametric surface. Therefore, we apply the method provided by Shi-min [Hu and Wallner, 2005] to project a point orthogonally onto a surface. This method consists of a geometric second order iteration which converges faster than first order methods and whose sensitivity to the choice of initial values is small.

4.2.4 Surface curvature calculation

With respect to curvature, we estimate the error between ideal and real curvature value:

$$Error_c = \frac{\sum_{i=1}^{n} ||ideal_c| - |real_c||}{n} \tag{4.7}$$

where $ideal_c$ represents the analytically obtained value and $real_c$ represents the measured value from the point cloud reconstruction. From its remarkable symmetry [Conway and Sloane, 1999], we know that the ideal Gaussian and mean curvatures of sphere model are constant. Therefore, for each point on the sphere, the Gaussian curvature is $K = 1/R^2$ and the mean curvature is $H = 1/R$ where R is the radius of the sphere. As for the point on the ellipsoid surface, the

Gaussian and mean curvature are derived from equation introduced by Jacobs et al.[Jacobsen et al., 2009]. As we have learned, the oval surface is a parametric type surface. For the parametric surface, the first and second fundamental forms of a surface determine its important differential-geometric invariants: the Gaussian curvature, the mean curvature, and the principal curvatures. So we derive the surface curvature of oval by the equation:

$$K = \frac{LN - M^2}{EG - F^2}, H = \frac{EN - 2FM + GL}{2(EG - F^2)} \tag{4.8}$$

where $E = \overrightarrow{r_u}.\overrightarrow{r_u}$, $F = \overrightarrow{r_u}.\overrightarrow{r_v}$, $G = \overrightarrow{r_v}.\overrightarrow{r_v}$, $L = \overrightarrow{r_{uu}}.\overrightarrow{n}$, $M = \overrightarrow{r_{uv}}.\overrightarrow{n}$, $N = \overrightarrow{r_{vv}}.\overrightarrow{n}$, $\overrightarrow{n}$ is a unit normal vector to the parameterized surface at a regular point:

$$\overrightarrow{n} = \frac{\overrightarrow{r_u} \times \overrightarrow{r_v}}{|\overrightarrow{r_u} \times \overrightarrow{r_v}|} \tag{4.9}$$

Up to a sign, these quantities are independent of the parameterization used. However we only use the absolute value of Gaussian curvature and mean curvature to estimate the curvature error, as a result, these quantities are thoroughly independent during our curvature error estimation.

However, because of the addition of noise, points on the output surface are not necessary still on the original ellipsoid surface. To that end, we first find the nearest point on ellipsoid surface for each point on output surface and then calculate the ideal Gaussian/mean curvature of each point on output surface as that of its nearest point on ellipsoid surface.

A large number of approaches have been proposed for triangulated surface curvature calculation [Magid et al., 2007], some of which give very unpredictable results. In order to estimate the real curvature value of points on the output surface, we choose the paraboloid fitting approach [Sander and Zucker, 1990] which is by far one of the most stable methods in the field of surface curvature calculation.

4.3 Experimental results

We evaluate the four representative algorithms on our synthetic models i.e. a sphere with the radius 0.8004, an ellipsoid (a=0.5, b=0.8547, c=1.2) and an oval (a=1, b=0.78). In this case, these three synthetic models can be more comparable since they are evaluated with the same volume. First of all we need to establish if the number of points generated for the point cloud provides sufficient information for the reconstruction process. In other words, we need to check if the points sample set results in a situation of oversampling or under-sampling. Subsequently, we take a local observation of each algorithm to check the performance at different noise level. Finally, we have an overall view of all the methods to see which one has the best stability and resilience.

4.3.1 Under/oversampling estimation

For the estimation of the under/oversampling, a number of factors need to be taken into consideration. Scale is one of the important parameters included in both the Fourier-based algorithm and Poisson reconstruction method, though slightly different definitions for scale are used by these methods. Generally speaking, the scale factor is defined as a floating point value that specifies the ratio of diameters between the cube used for reconstruction and the bounding cube of the samples. In this estimation we select two factors i.e. input point number and scale. We applied Fourier-based algorithm on the point cloud representing a sphere model without noise and evaluate the surface distance error.
In Figure 4.3 the result of under/oversampling estimation is depicted. As can be seen, the distance error decreases when the number of input points increases. Moreover, the decay of the distance error is relatively sharp at the beginning while in the end it diminishes, especially in the range of 30000 to 50000 input points the error is almost stable. From these results we conclude that if the input point number is over 30000, then, for the reconstruction methods, the model can be considered oversampled.

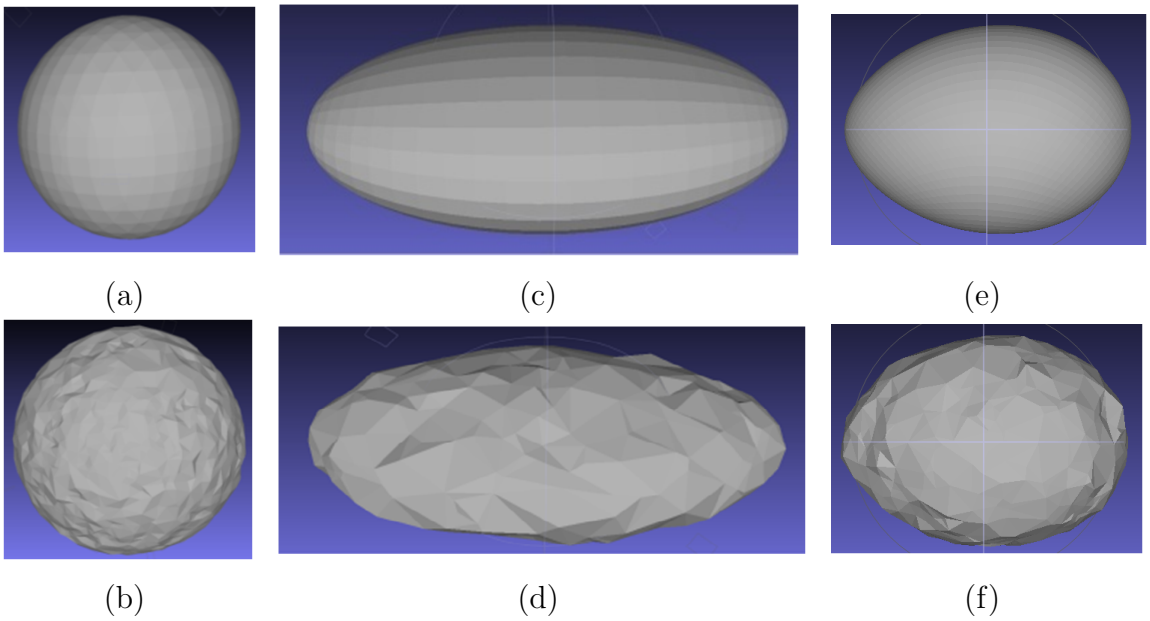

Figure 4.2. Models with and without noise (snapshots from Meshlab [Cignoni, 2010]). (a) Sphere model without noise, (b) Sphere model with noise, (c) Ellipsoid model without noise, (d) Ellipsoid model with noise, (e) Oval model without noise, (f) Oval model with noise.

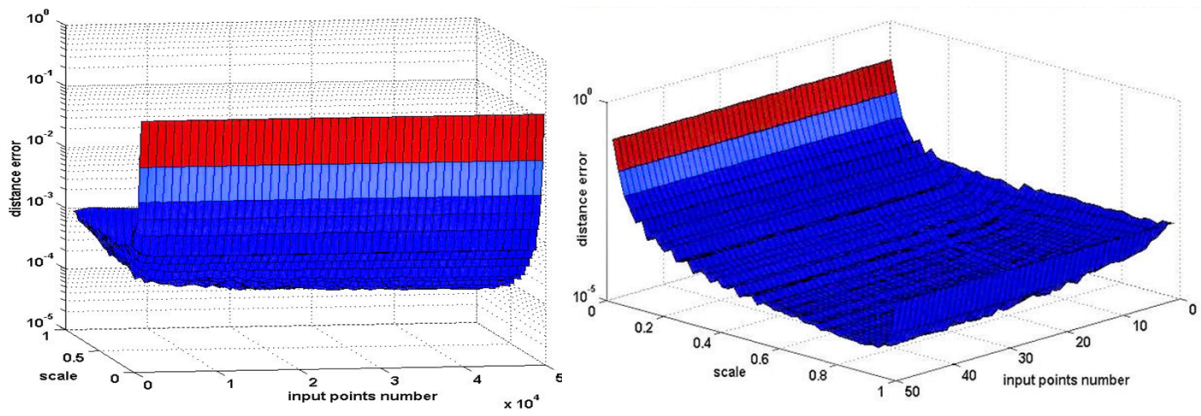

Figure 4.3. Under/oversampling estimation. (a) front view, (b) top view. We apply point distance calculation to estimate the range of the input point number when the model is oversampled. The change of the stripe color from dark blue to red shows the increase of distance error. Therefore, red indicates undersampling.

4.3.2 Local observation

4.3.2.1 Sphere model distance/area error estimation

For convenience of the evaluation procedure, the algorithms are divided into two groups. The first group consists of Power Crust (PC) and Robust Cocone (RCC). By changing the number of input points we observe the performance of two methods under different noise levels. In the reconstruction process we use the default settings of each algorithm. In table 4.1 the changes in the number of output points with respect to the number of input points without the addition noise. Power Crust adds a large number of additional points on the output surface while, for Robust Cocone, the number of output points remains the same. Figure 4.4 (a) and (b) demonstrate that the distance error estimations of these two methods are almost the same. However, in Figure 4.4 (c) and (d) the area error estimation shows clear differences. The area error of Robust Cocone is lower and more stable. Nevertheless, both methods demonstrate the same trend that at increasing levels of noise, the distance error and the area error escalate accordingly.
The second group includes Fourier-based reconstruction (FOU) and Poisson reconstruction (POI) as they have a similar structure of processing and parameters (i.e. resolution, scale). We compare these methods with an oversampling and input of 50000 points; using the same resolution. Their performance is tested within a range of the scale factor and under different levels of noise. In the Fourier-based reconstruction method, as shown in Figure 4.5(a) and 4.5(c), the output number increases together with scale factor. At smaller scales, the error in both parameters is large. This is due to the inadequacy of characteristics integrated in the implicit function since the model only has less than 30 points on the surface, as shown in Figure 4.6(a). When the scale is increasing, the error reduces drastically. An example is shown in Figure 4.6(b). However, at a scale > 0.95, the error in the area increases again. This is due to the fact that the diameter of the cube used for reconstruction is too small to have any points in the cube. As a result, the output surface model is no longer watertight (i.e. closed) and consequently the area error increases. This is shown in Figure 4.6(c).
In contrast, in the Poisson reconstruction method, the scale setting is the inverse of the scale in Fourier-based reconstruction. As can be seen in Figure 4.5(b) and

4.5(d); i.e. when the scale increases, the error increases. Although the Poisson error estimation curves are not smooth, the error ranges for both measurements remain relatively small compared to Fourier-based reconstruction method.

Table 4.1. Output points comparison

IP	500	1000	1500	2000	2500	3000	3500	4000	4500	5000	5500
PC	2146	4272	6797	8548	11261	13588	15266	18049	20184	22209	25483
RCC	500	1000	1500	2000	2500	3000	3500	4000	4500	5000	5500
IP=input points, PC= Power Crust output points, RCC=Robust Cocone output points											

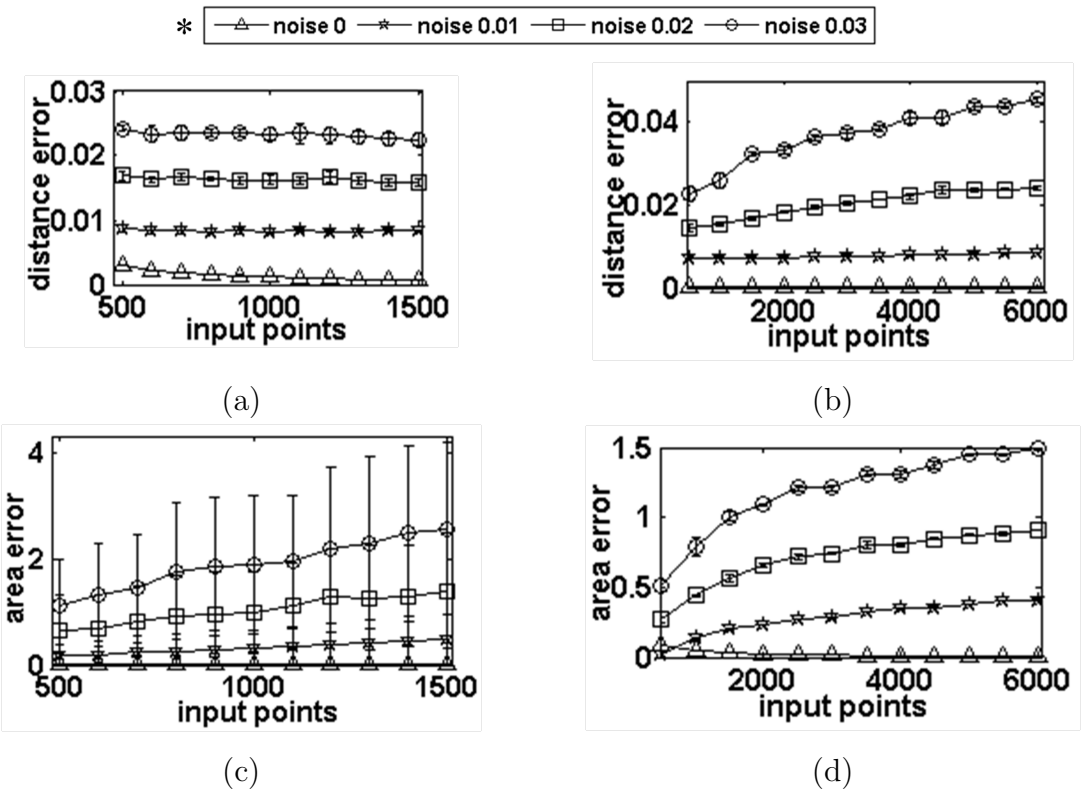

Figure 4.4. Sphere PC/RCC distance and area error estimation. (a) PC Distance error, (b) RCC Distance error, (c) PC Area error, (d) RCC Area error. * the ranges of the noise and the glyphs used in the graphs in (a-d).

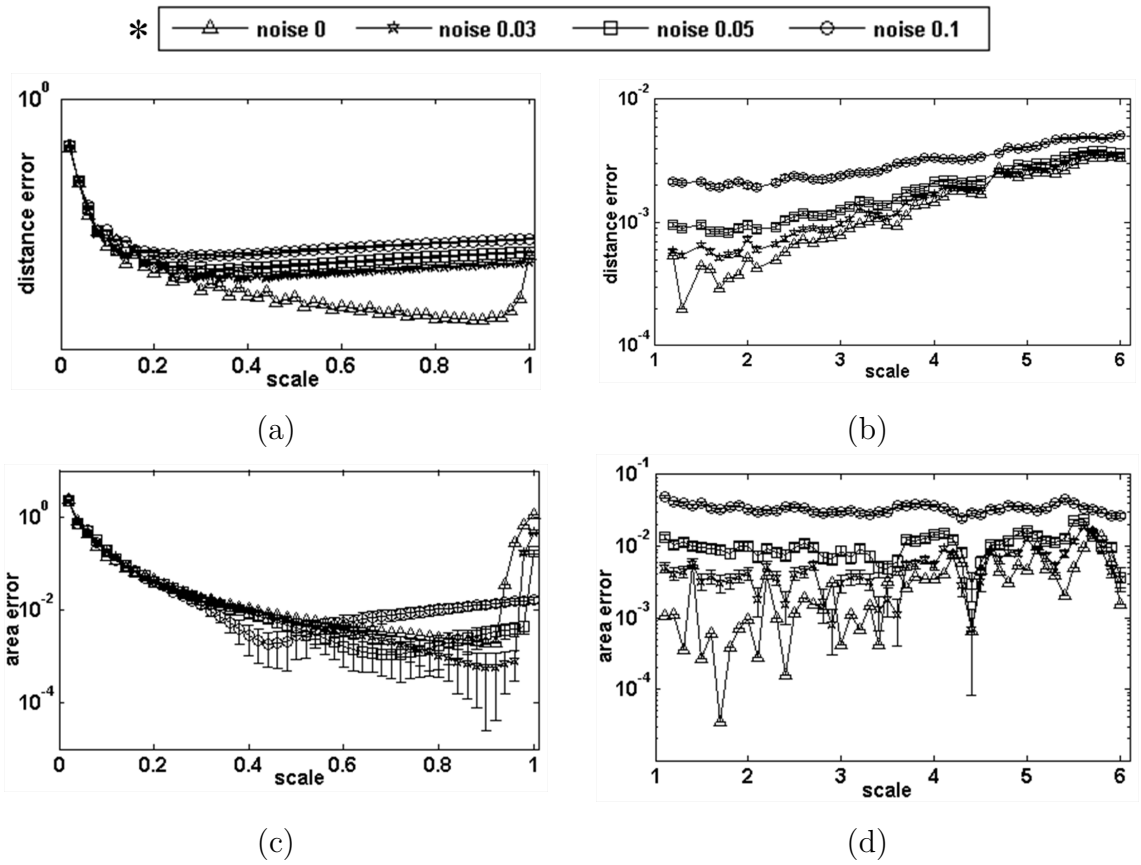

Figure 4.5. Sphere FOU/POI distance and area error estimation. (a) FOU Distance error, (b) POI Distance error, (c) FOU Area error (d) POI Area error. * the ranges of the noise and the glyphs used in the graphs in (a-d).

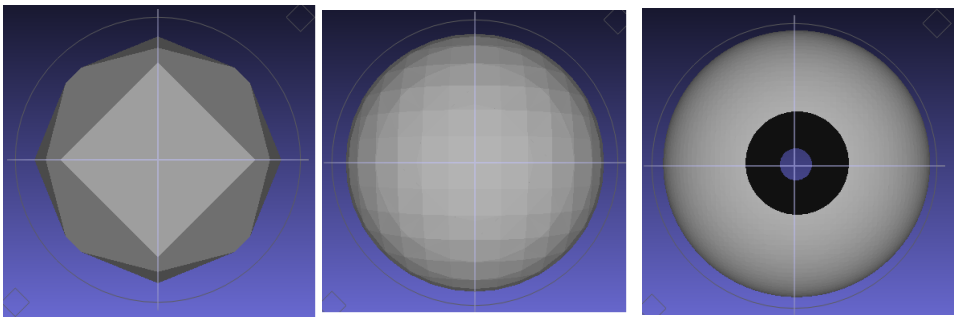

(a) (b) (c)

Figure 4.6. Sphere output samples of Fourier-based reconstruction method (snapshot in Meshlab [Cignoni, 2010]).(a) sphere output model with scale 0.04, (b) sphere output model with scale 0.2, (c) sphere output model with scale 0.98.

4.3.2.2 Ellipsoid model distance/area error estimation

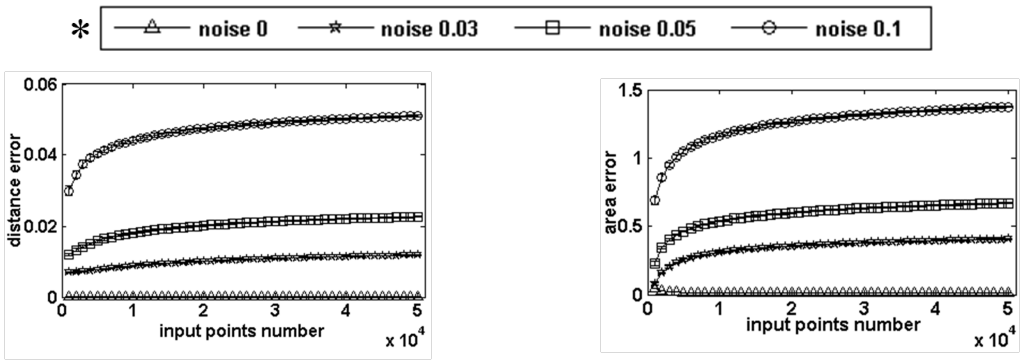

(a) (b)

Figure 4.7. Ellipsoid RCC distance and area error estimation (a)RCC Distance error, (b)RCC Area error. * the ranges of the noise and the glyphs used in the graphs in (a-b).

From this part of the evaluation we exclude Power Crust reconstruction methods since the output model is easily broken and obviously not resilient to noise. The remaining three methods are used for further evaluation. Figure 4.7 and Figure 4.8 provide the distance and area evaluations for these three methods. It is clear that the error in distance and area demonstrate the same trend. For example, when the scale factor in Poisson reconstruction increases, both the distance and area error increase as shown in Figure 4.8(c) and 4.8(d). Interestingly, for the results of both Fourier-based and Poisson reconstruction there usually exists an optimum for the minimal distance and area error.

4.3.2.3 Oval model distance/area error estimation

For the oval model, most of the graphs show the same trend as the sphere model and the ellipsoid model. However, in Figure 4.10(d), the area error for Poisson reconstruction method demonstrates some difference. When the noise increases, the area error shows high up at a low scale level. That is because, for a more complicated model, the Poisson reconstruction method integrates more noise points as a feature factor into the characteristic function. As a result the output surface

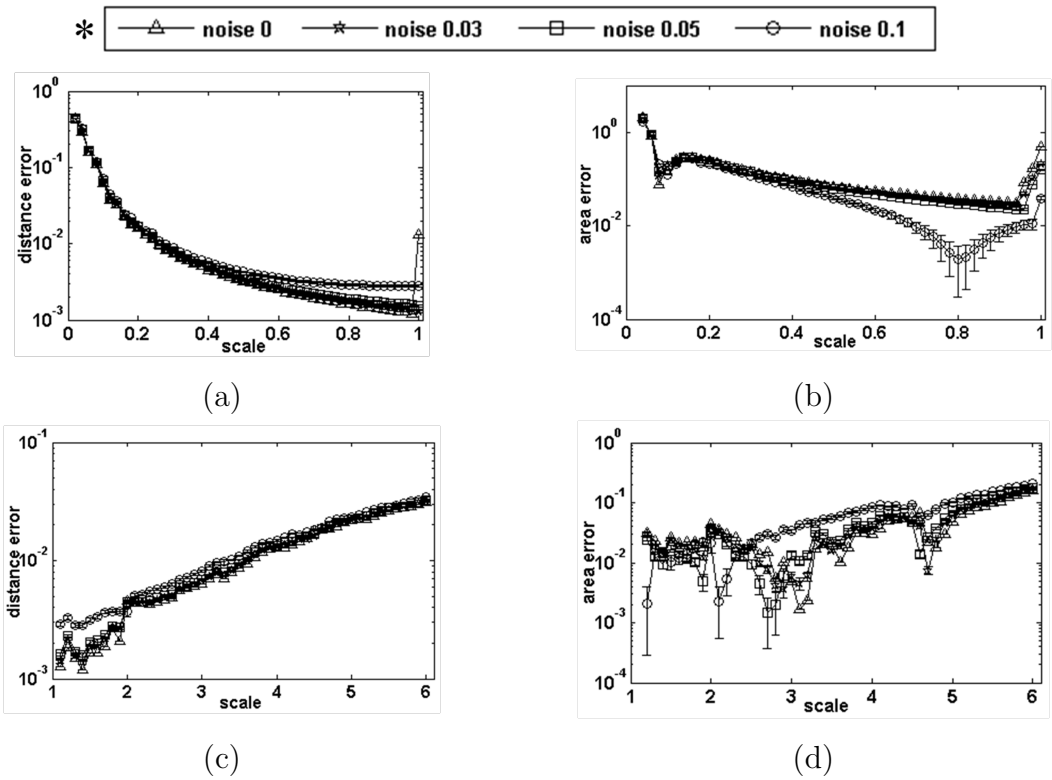

Figure 4.8. Ellipsoid FOU and POI distance and area error estimation. (a) FOU Distance error, (b) FOU Area error, (c) POI Distance error, (d) POI Area error. * the ranges of the noise and the glyphs used in the graphs in (a-d).

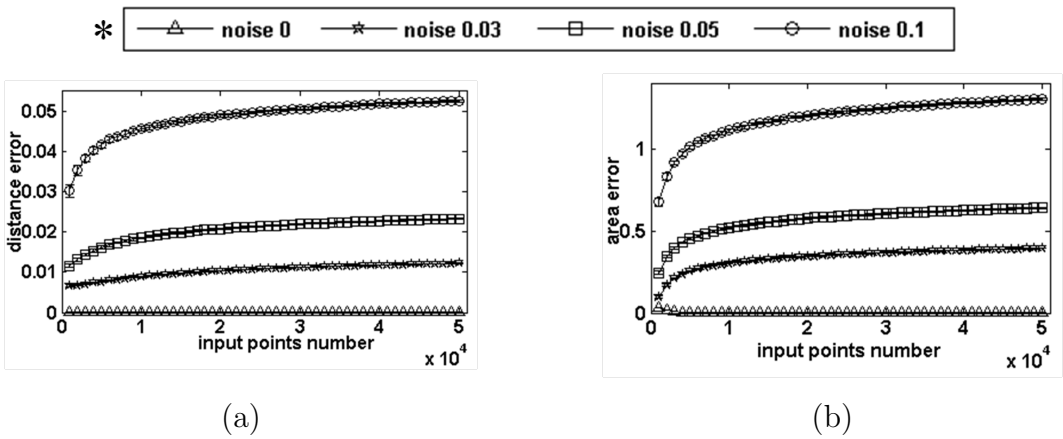

Figure 4.9. Oval RCC distance and area error estimation (a)RCC Distance error, (b)RCC Area error. * the ranges of the noise and the glyphs used in the graphs in (a-b).

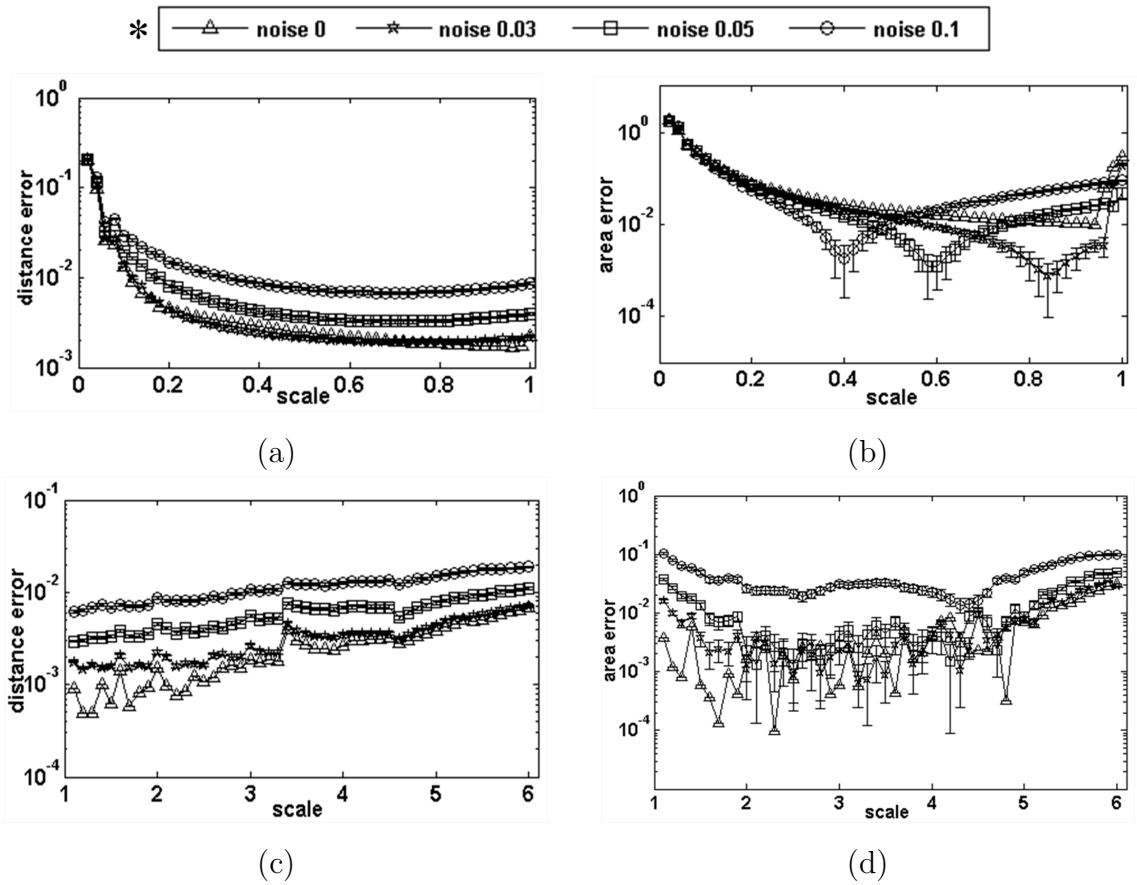

Figure 4.10. Oval FOU and POI distance and area error estimation. (a) FOU Distance error, (b) FOU Area error, (c) POI Distance error, (d) POI Area error. * the ranges of the noise and the glyphs used in the graphs in (a-d).

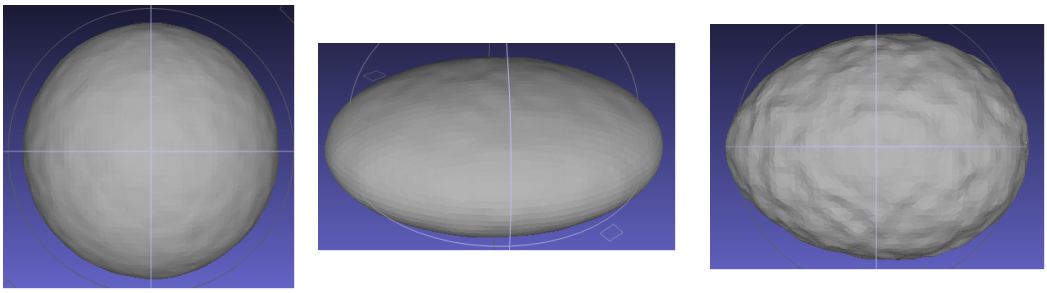

Figure 4.11. Output surface of Poisson reconstruction method with the noise level 0.1 and the scale 1.1 (snapshot in Meshlab [Cignoni, 2010]).

would be rougher and the area error is increasing. In Figure 4.11, we compare the output surface of the sphere, the ellipsoid and the oval from Poisson recon-

struction method with the same noise level and a same low scale setting.

4.3.2.4 Sphere model curvature error estimation

The discussion of curvature error estimation is continued in following three sections. So as to find the reconstruction method that best preserves the curvature characteristic, three methods would be further evaluated. Moreover, in order to obtain a better observation of the results, we use the standard deviation of mean as our error bar for the curvature error estimation sessions.

When we take into a close look at the output surface model from Robust Cocone, we find the orientation of each triangulated surface is not coherent. Moreover, some of the output surface model has non manifold faces. However, for the paraboloid fitting scheme, all the faces on the output surface should be coherently oriented. As a result, we use the script of Meshlab [Lindblad, 2005] software to remove non manifold faces and re-orient all the faces before we estimate the mean/Gaussian curvature. The curvature estimation results from Robust Cocone, as shown in Figure 4.8(a) and 4.8(b), seem irrational. Apart from noise level 0, at increasing noise, the mean/Gaussian curvature error is decreasing. This is caused by the fact that in the reconstruction process of Robust Cocone, at higher levels of noise in the input point cloud, the output number of triangulated points is reduced so as to preserve the smoothness of the output surface. Thus, producing the same number of input points, lower levels of noise generate a surface model with higher resolution resulting in a rougher output surface and a higher local curvature error.

Since with the same scale setting the point number of output surface remains the same, the results of Fourier-based and Poisson reconstruction methods are much more rational. At increasing output resolution, the curvature error decreases at very beginning and increases again at the end. The reason is that, take Fourier-based reconstruction method as an example, when the scale is small the resolution of output surface model is quite low, as shown in Figure 4.6(a). As a result, the local curvature error is high. On the other hand, when the scale is high, more noisy points are preserved. Therefore, the local curvature error is still high. In Figure 4.12 it is illustrated that the Fourier-based and Poisson reconstruction methods have a smaller error in curvature compared to the Robust

Cocone method.

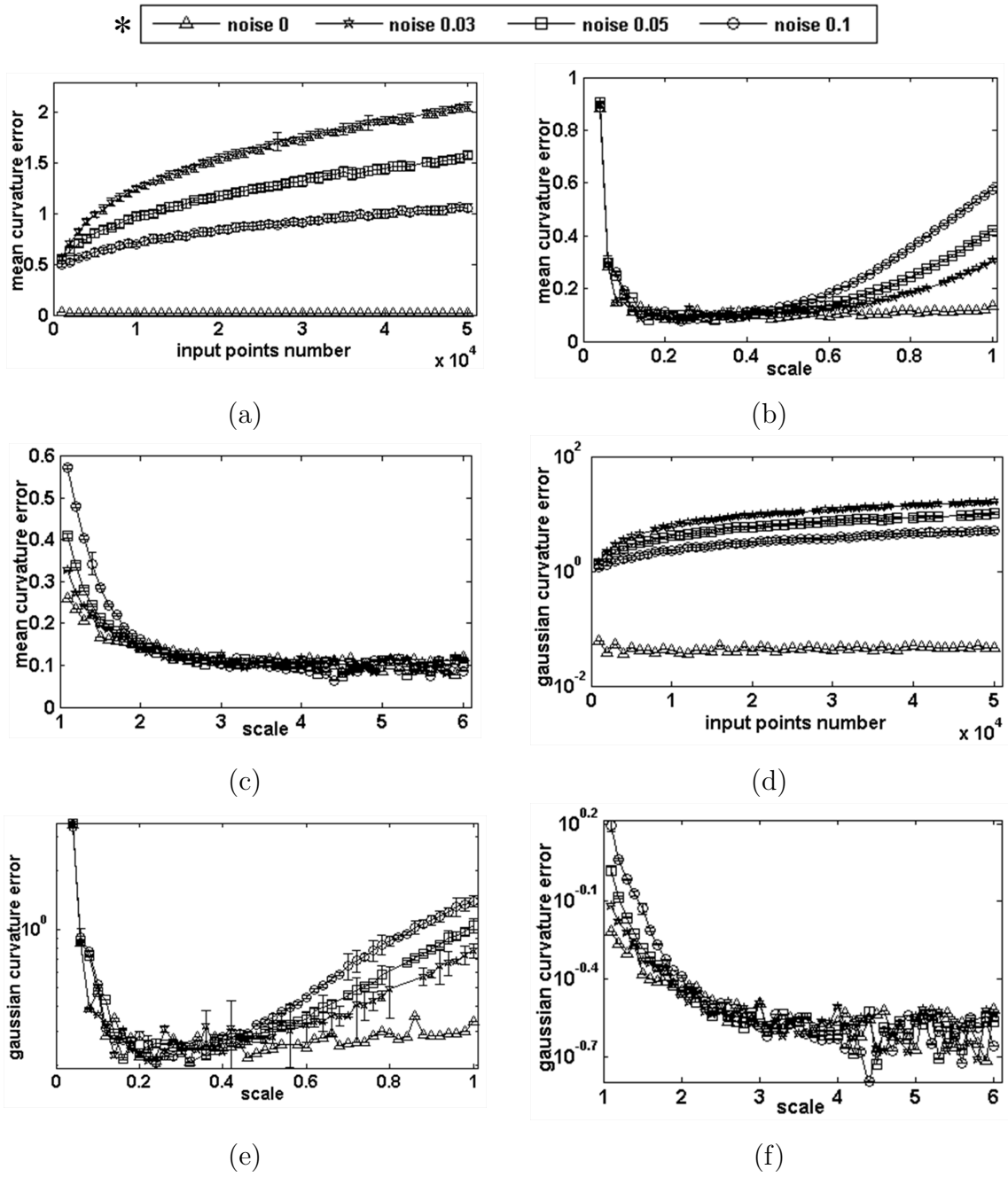

Figure 4.12. Sphere curvature error estimation. (a) RCC Mean curvature, (b) FOU Mean curvature, (c) POI Mean curvature, (d) RCC Gaussian curvature, (e) FOU Gaussian curvature, (f) POI Gaussian curvature. * the ranges of the noise and the glyphs used in the graphs in (a-f).

4.3.2.5 Ellipsoid & oval model curvature error estimation

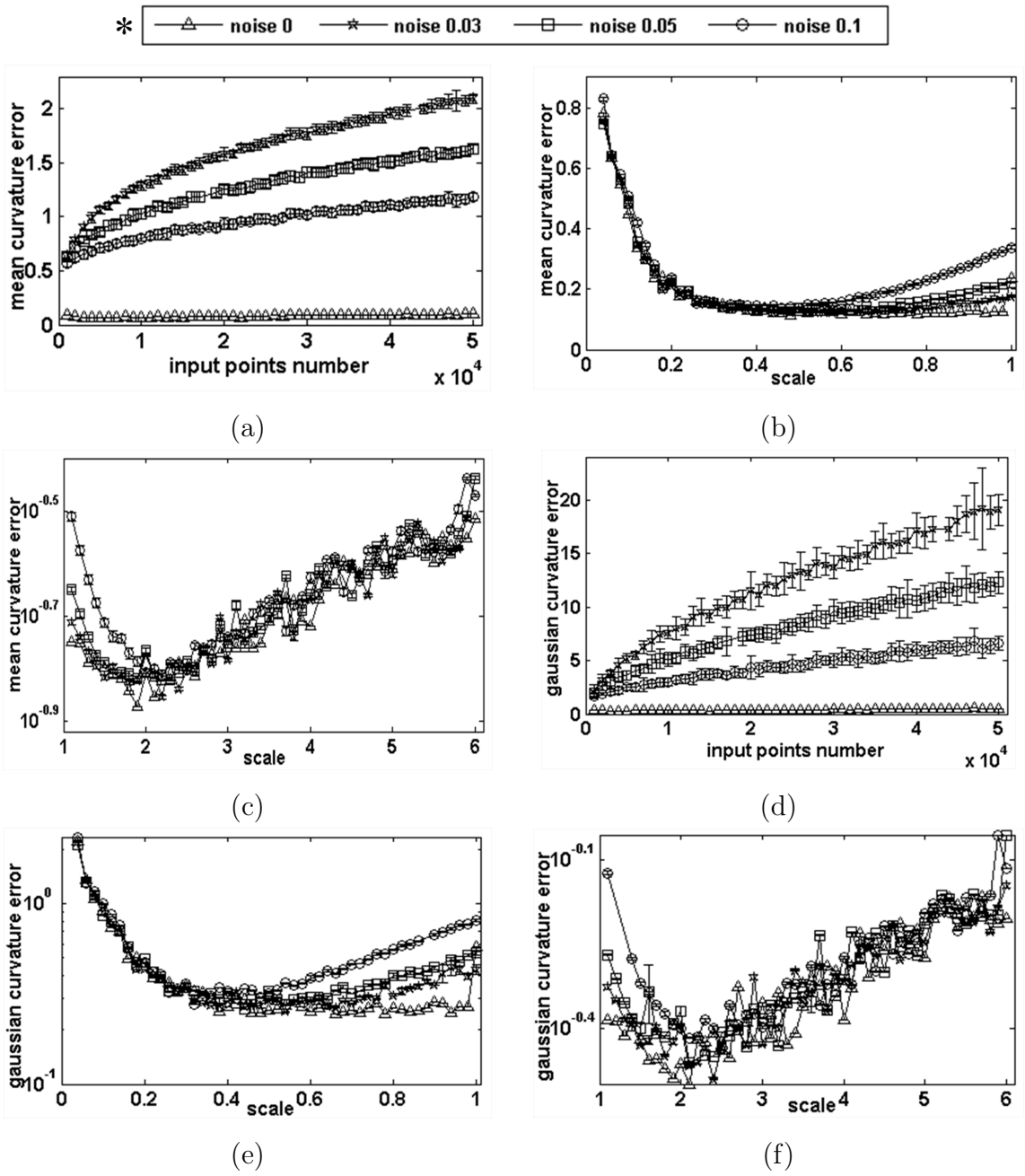

Figure 4.13. Ellipsoid curvature error estimation. (a) RCC Mean curvature, (b) FOU Mean curvature, (c) POI Mean curvature, (d) RCC Gaussian curvature, (e) FOU Gaussian curvature, (f) POI Gaussian curvature. * the ranges of the noise and the glyphs used in the graphs in (a-f).

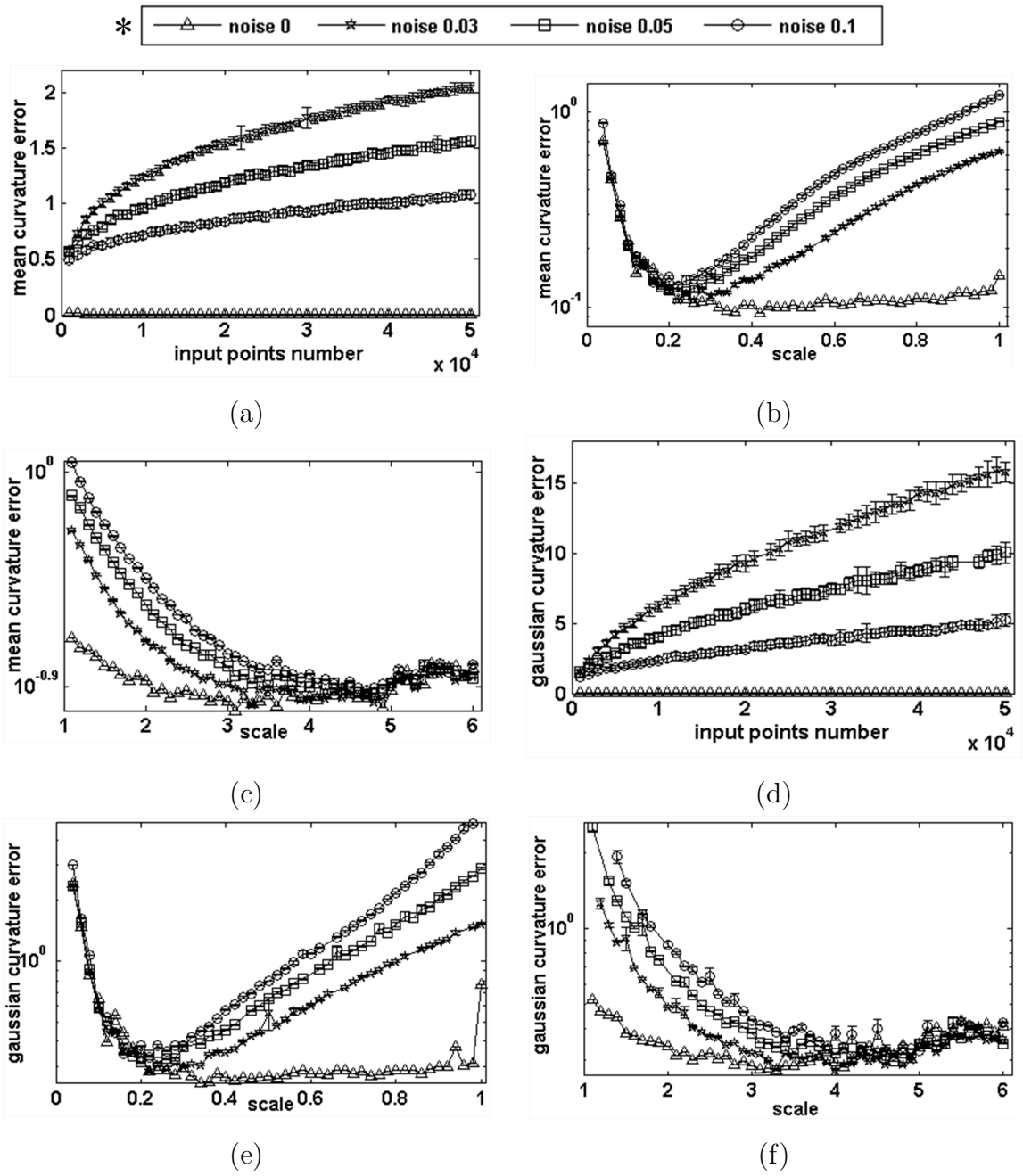

Figure 4.14. Oval curvature error estimation. (a) RCC Mean curvature, (b) FOU Mean curvature, (c) POI Mean curvature, (d) RCC Gaussian curvature, (e) FOU Gaussian curvature, (f) POI Gaussian curvature. * the ranges of the noise and the glyphs used in the graphs in (a-f).

For the ellipsoid and the oval, the curvature errors show the same trend. In Figure 4.13(a),(b) and Figure 4.14(a),(b), as noise increasing the mean/Gaussian curvature error of Robust Cocone is decreasing. For the Fourier-based and Poisson reconstruction methods the curvature error decreases at very beginning and increases again at the end when the output resolution ascends. Overall the Fourier-based and Poisson reconstruction methods have a smaller error in curvature compared to the Robust Cocone method as shown in Figure 4.13 and Figure 4.14.

4.3.3 Global observation

Table 4.2. Sphere distance/area comparison.

SPHERE	D	A				
	MIN		MEAN		σ	
POI	1.98E-04	0	0.0021	0.0132	0.0012	0.0128
FOU	3.83E-05	9.54E-07	0.0033	0.1092	0.0154	0.3558
RCC	2.23E-07	4.01E-05	0.0199	0.5164	0.0183	0.4334

Table 4.3. Sphere Gaussian/mean curvature comparison.

SPHERE	K	H				
	MIN		MEAN		σ	
POI	0.1516	0.0606	0.3326	0.1322	0.1771	0.0681
FOU	0.1863	0.0725	0.6539	0.1834	11.1527	0.1453
RCC	0.0359	0.0145	5.0525	0.9171	4.5942	0.6271

Table 4.4. Ellipsoid distance/area comparison.

ELLIPSOID	D	A				
	MIN		MEAN		σ	
POI	0.0012	3.81E-06	0.0128	0.05	0.0094	0.0466
FOU	0.0012	4.01E-05	0.0277	0.1578	0.077	0.3011
RCC	7.32E-07	0.0097	0.0193	0.5493	0.0177	0.4615

Table 4.5. Ellipsoid Gaussian/mean curvature comparison.

ELLIPSOID	K	H				
	MIN		MEAN		σ	
POI	0.3169	0.1339	0.5067	0.2142	0.4799	0.0513
FOU	0.2458	0.1153	0.4744	0.2060	0.6649	0.1382
RCC	0.2824	0.0648	6.3863	0.9863	5.7915	0.6215

Table 4.6. Oval distance/area comparison.

OVAL	D	A				
	MIN		MEAN		σ	
POI	4.94E-04	0	0.0059	0.017	0.0043	0.0218
FOU	0.0017	3.81E-06	0.0124	0.1177	0.0318	0.3092
RCC	2.31E-07	1.72E-04	0.0199	0.5263	0.0182	0.4418

Table 4.7. Oval Gaussian/mean curvature comparison.

OVAL	K	H				
	MIN		MEAN		σ	
POI	0.2637	0.1003	0.5295	0.1939	0.7663	0.1507
FOU	0.2455	0.0935	0.9321	0.3277	1.0066	0.2594
RCC	0.0146	0.0050	5.0815	0.9183	4.5232	0.6306

After an evaluation based on observations in the local ranges, we still need to compare the results as a whole so as to establish the method with the best performance. To that end, we change the input point number from 1000 to 50000 at 1000 point intervals and at the same time change the scale factor in a range of 50 different values. The uniformly distributed noise is added to each set in 4 different levels (cf. Figure 4.8). This procedure has been repeated 50 times for each reconstruction setting. Finally, we calculated the minimum, average and standard deviation for the distance error, the area error, the Gaussian and mean curvature error as estimated from each data set.

Table 4.2 to Table 4.7 present the general evaluation for the combination of all the noise levels. With respect to the sphere model evaluation (Table 4.2 and Table 4.3), Poisson reconstruction method performs more stable (cf. the column). The mean values indicate that Poisson reconstruction still has the best performance with respect to distance error, area error and surface curvature error estimation. For the minimum values, Robust Cocone reconstruction method shows the highest incidence to be in the top. Regarding the Ellipsoid model evaluation (cf. Table 4.4 and Table 4.5), Poisson has the best mean value with relatively high stability in distance error and area error. While Fourier-based reconstruction method has the best mean value in curvature error estimation. However, Poisson always has the lowest standard deviation value. According to the lowest minimum value, Robust Cocone is on top of distance error and mean curvature error evaluation, while Poisson reconstruction method has the lowest minimum value in the area error estimation and Fourier-based reconstruction method has the lowest minimum value in the Gaussian curvature error estimation. As for the oval model (Table 4.6 and Table 4.7), Poisson reconstruction method always has the lowest mean value with the best stability. Robust Cocone has the lowest minimum value of distance error and curvature error estimation, meanwhile, Poisson reconstruction method has the lowest minimum value of area error evaluation.

4.4 Conclusion and future work

In this paper, we have presented an analytical approach to the evaluation of four different methods for 3D surface reconstruction from a point cloud. We generate the point cloud of synthetic geometrical objects i.e. sphere, ellipsoid and oval, and perform error estimation by comparing surface area, distance and curvature between output surface models and ideal synthetic models. By evaluating all parameters of the algorithm and at different noise levels, the total size of the experimental dataset exceeded 50000 files (ply format). From our experimental results we conclude that the Poisson reconstruction method [Kazhdan et al., 2006a] has the most stable performance and is most resilient with increasing amounts of noise in the data. The Fourier-based reconstruction method comes second. Therefore, we can conclude that the class of implicit surface reconstruction methods clearly performs better than the interpolation based class for the surface reconstruction. That is, as we evaluate it to analytical criteria.

The rationale of this work is to obtain a profound assessment of different 3D surface reconstruction approaches, in particular, with respect to measurements that can be derived from reconstructed surfaces. The evaluation will help us in a motivated method selection of surface reconstruction for biological 3D models. For the progress in the research area of bio-imaging and image modelling, such analysis is crucial. With the results surface features for biological shapes can be derived from the data that are obtained by some imaging device, i.e. a microscope. Modern imaging techniques produce 3D images and with the methods described in this paper we can derive surface estimations directly from the image data. In general, these images are pre-processed and sublimated to 3D models. In that case, the methodology will be applied in the same manner; that is, starting from an annotated 3D model [Verbeek, 1999a].

Given a 3D representation, other approaches for surface area computation have been described; early methods use the statistical approach from stereology [Baddeley et al., 1986] to come to an estimation of the surface area. These methods can be very efficient if prior information on the shape can be used; and the stereology approach is still successfully used [Ziegel and Kiderlen, 2010]. Taking a

sampled volume as the starting point, estimators for digitized surfaces have been developed [Lindblad, 2005; Mullikin and Verbeek, 1993]; these are based on the probability that a certain voxel-position can contribute to the surface area and weights are assigned to surface voxel configurations. Moreover, the estimators on volume data require an isotropically sampled image; this is not in all cases possible. Stereology is able to deal with the non-isotropically sampled data and the undersampling in the z-direction is specifically addressed. The stereology is therefore successfully used with images obtained from physical sections. The method based on implicit surface reconstruction can very well deal with undersampling and therefore it is suitable for models derived from physical sections or otherwise undersampled input.

The methods described in this paper first derive a surface which is subsequently used in the measurements. In this manner the initial sampling is surpassed; the surface description allows extracting a number of features from the surface, i.e. surface area, curvature and others. The analytical shapes that we have used for the assessment of the surface description provide useful information on the surface representations. From tables 4.2-4.7 we learn that the more the shape resembles a sphere, the more accurate the measurement will be. The ovaloid shape is closer to the sphere than the ellipsoid shape and this is reflected in the resulting error measurement. Including previous results [Cao and Verbeek, 2012] we conclude that the error of the shape increases with size. Importantly, with the given shapes the error and the coefficient of variation are below the range that one expects as variation in a measurement of a population of individuals as is common in biology. Therefore the measurements can be used to describe differences between individuals of treated/untreated groups, although in all cases reflection on the outcome remains important. Moreover, the analytical shapes that we have exploited are also representing shapes, or at least partially, as we encounter them in nature. The results can therefore be used to assess the range of the error that can be expected with the reconstruction of a surface of a shape; i.e. it resembles more of a sphere or an ellipsoid.

From the results presented in this paper, it is clear that we intend to further exploit the Poisson reconstruction method. Next, we will specifically utilize the results on biological 3D models so as to improve the quality of the surface rep-

resentations as well as making the surface representations suitable for analytical approaches. The imaging research supporting analytical description of 3D shapes, i.e. embryos in molecular genetics and development, will greatly benefit from the possibilities provided in this study.

Chapter 5

Optimizing 3D model representations for 3D phenotype analysis

Partially based on:

L. Cao, F.J. Verbeek. Nature inspired phenotype analysis with 3D model representation optimization. The 4th International Conference on Innovations in Bio-Inspired Computing and Applications,Ostrava, 2013

Abstract: In support of research in biology 3D models are constructed. These are made for visualization and analysis. In micro-anatomy these models often suffer from undersampling in the plane perpendicular to the sampling plane. In this paper we present a pipeline for optimization of 3D models obtained from plan-parallel images so that the 3D model is more suitable for shape analysis. In particular, we intend to create an optimized 3D model for analyzing phenotypical differences originating from different conditions and we extract shape features from the 3D models. The optimization is required for obtaining shape features that properly represent the object. The 3D model contains structures represented as contours that were extracted from the image stack. Starting from a point cloud based reconstruction method, i.e. Poisson reconstruction, we devised a method to convert a stack of contours into a uniformly distributed point cloud. The entire point cloud is integrated in the surface construction resulting in a surface that accurately represents the shape. The feasibility of our method has been confirmed by a representative case study in zebrafish development. The method can be successfully used for datasets from different types of imaging modalities.

5.1 Introduction

In recent studies [Long et al., 2012; Ng et al., 2012; Rubel et al., 2010] three-dimensional(3D) morphological information is used to find the various phenotypes in a sample population. Here a sample population consists of biological objects from images captured with a microscope at a certain magnification. The phenotype differences in the population are found in the micro-anatomy and characterized by shape features. It is clear that 3D models derived from microscope images potentially offer deeper insights for analysis. Therefore, 3D images and 3D models are frequently used for biological object visualization and analysis. With 3D microscopy techniques such as bright field [Tadrous, 2012; Willis et al., 1993] and confocal microscopy [Gouaillard et al., 2009; Natalie et al., 2004] it is possible to obtain 3D information from a plan-parallel stack of 2D slices. For bright field microscopy, the sampling is often realized by invasive physical sections that are acquired to capture images and then reassembled to a 3D image stack. Another option is to acquire images on the confocal laser scanning microscope (CLSM) and process the non-invasive optical sections to 3D models. The physical sectioning technique is very suitable for modelling histological information and larger structures such as tissues or organisms. The confocal technique is more geared towards imaging specific small structures such as cells and small multi-cellular structures such as embryos.

From the 3D stack of images a graphical model can be derived by segmentation or manual delineation of structures of interest. Manual delineation is used when specific structural knowledge cannot directly be derived from the image; a specialist then selects the specific information through graphical annotation [Verbeek et al., 1999a], aka delineation. A set of contours as extracted from the stack subsequently represents the 3D model. The general observation is that the output stack of 2D contours is (nearly) always under-sampled perpendicular to the direction of sampling. In order to improve the model some kind of interpolation can be applied. The classical way of performing such interpolation between section images (slices) is an interpolation of the gray values in the slices so as to estimate the gray values in the missing slices [Herman et al., 1992]. A linear interpolation for estimating the missing slices, however, may lead to artifacts. A

more advanced manner is a shape-based interpolation [Herman et al., 1992] which is applied directly to the contours of the model.
Two dominant methods of 3D shape reconstruction from consecutive contours are contour stitching and volumetric methods. Contour stitching methods directly connect the vertices of adjacent contours and produce a mesh that passes through all contours such as the methods provided by Keppel [Keppel, 1975] and Boissonnat [Boissonnat, 1988]. Keppels method intends to maximize a function based on the volume of the triangulated surface model. However, this early technique is not handling special cases such as branching. Boissonnat utilizes Delaunay tetrahedralization to successfully cope with branching structures in the model. Contour stitching methods construct the surface by consecutively building up the triangulated patches slice by slice. It disregards the whole picture of the object which could result in noise remaining in between the slices and creating incorrect topologies in the structure of the model. The volumetric methods treats the stack of images as a whole by first interpolating intermediate gray-values and extracting the isosurfaces from a volumetric field. Representative methods are described by Levin [Levin, 1987] and Barrett et al. [Barrett et al., 1994]. Volumetric methods derive the isosurfaces directly from the interpolated gray-values. The smoothness of the surface model depends on the interpolation scheme. We tackle the problem of surface reconstruction using a point cloud based surface reconstruction method. The point cloud reconstruction method treats each point as a feature and inputs features into a mathematical model for an isosurface construction. The merit of a point cloud based reconstruction method is that as abstraction from a specific case to a general problem it sheds light on the critical aspects of the problem [Hoppe et al., 1992]. The process of mathematical model construction facilitates unwanted noise suppression and prominent feature preserving of the surface. In our analytical evaluation of point cloud based reconstruction methods [Cao and Verbeek, 2012] a review of recent methods is given. We aim at reconstructing the surface and suppressing the noise with the information from three directions (xyz). As a result, we develop a pipeline to produce a precise and smooth surface from a set of plane-parallel contours and extract important surface features to analyze the model that is derived from sampling under different conditions.

The remainder of this paper is structured as follows. In section 5.2 we introduce our methodology. In section 5.3 we validate our method with two case studies: zebrafish embryo and the mouse mammary gland. In section 5.4 we present our conclusions and discuss the results.

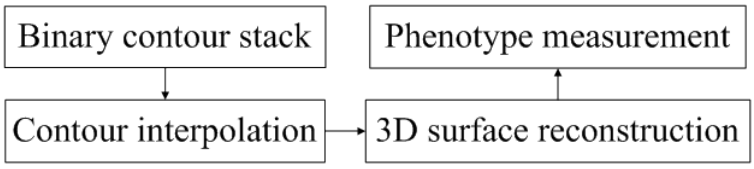

Figure 5.1. Pipeline of our system.

5.2 Methodology for model optimization

The input of our pipeline for model optimization is a stack of nicely aligned binary images with annotation information e.g. as obtained from an annotation software (TDR). Our pipeline is divided into several steps; the individual steps are as schematically shown in Figure 5.1: (1) contour interpolation, (2) 3D surface reconstruction and (3) phenotype analysis. Following to acquisition, the data are organized in a database and, structures apparent in the images are delineated by a contours. This is done either, for each slice through a manual delineation using our dedicated annotation software (TDR [Verbeek et al., 1993]) or automated segmentation; for manual delineation a WACOM digitizer tablet (WACOM, Cintiq LCD-tablet) is used. The contour stacks that are the basis of our models are well aligned by procedures prior to the modeling [Boon et al., 2000] and in case of the confocal images the alignment is an intrinsic quality of the microscope. In our pipeline we use the stack of images with only the contours as input.

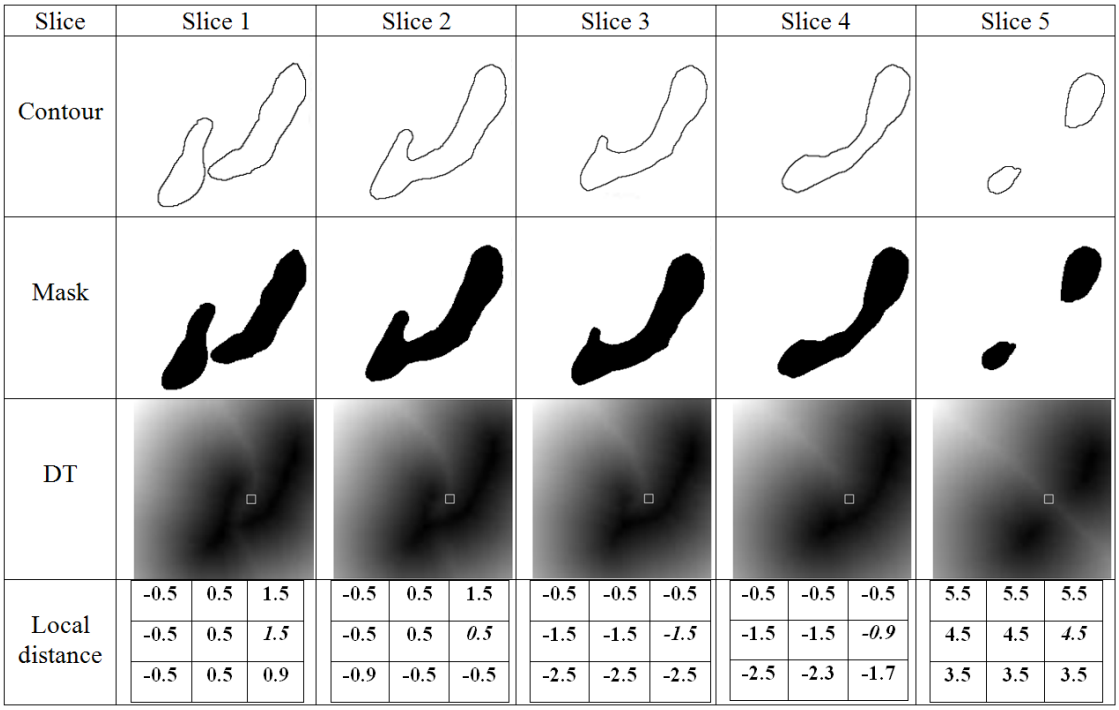

Slice	Slice 1	Slice 2	Slice 3	Slice 4	Slice 5
Contour					
Mask					
DT					
Local distance	-0.5 0.5 1.5 -0.5 0.5 *1.5* -0.5 0.5 0.9	-0.5 0.5 1.5 -0.5 0.5 *0.5* -0.9 -0.5 -0.5	-0.5 -0.5 -0.5 -1.5 -1.5 *-1.5* -2.5 -2.5 -2.5	-0.5 -0.5 -0.5 -1.5 -1.5 *-0.9* -2.5 -2.3 -1.7	5.5 5.5 5.5 4.5 4.5 *4.5* 3.5 3.5 3.5

Figure 5.2. Contour interpolation procedure from 5 example slices. Mask= Binary mask of the contour; DT= Distance transformation represented by Gray-value.

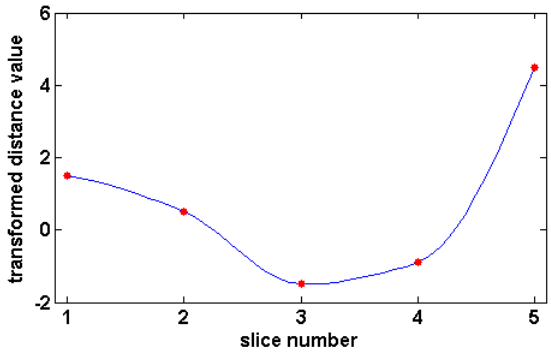

Figure 5.3. Piecewise cubic Hermite interpolation.

5.2.1 Contour interpolation

The sampling of an image stack derived from physical sectioning specifically is, in general, insufficient in the direction of sectioning (z direction). The insufficient

information in the Z-direction would prevent us from making a good surface description. Therefore, we introduce a method of subsampling through interpolation and develop the method to produce a truthful interpolation. In this process, we make use of a shape-based contour interpolation method [Verbeek, 1992; Verbeek et al., 1995]. To that end a distance transform is applied in the contour as shown in figure 5.2; each point in the resulting image represents the shortest distance to the contour. The points on the contour are zero. Now, the distances inside the contour set positive whereas the distances outside the contour are multiplied with -1 and thus these have a negative value. Setting the negative value is to distinguish between the pixels outside of the object and the pixels belonging to the object. For each pixel-column in the z-direction, a 1D monotone piecewise cubic spline [Fritsch and Carlson, 1980] is constructed to interpolate distance values in z-direction [Braude et al., 2006]. A monotone cubic interpolation is based on the cubic Hermite spline with a coefficient matrix that looks as follows:

$$P(t) = \begin{bmatrix} t^3 & t^2 & t & 1 \end{bmatrix} \begin{bmatrix} 2 & -2 & 1 & 1 \\ -3 & 3 & -2 & -1 \\ 0 & 0 & 1 & 0 \\ 1 & 0 & 0 & 0 \end{bmatrix} \begin{bmatrix} \mathbf{p}_0 \\ \mathbf{p}_1 \\ \mathbf{v}_0 \\ \mathbf{v}_1 \end{bmatrix} \tag{5.1}$$

where $\mathbf{p}_0$ and $\mathbf{p}_1$ are two endpoints; $\mathbf{v}_0$ and $\mathbf{v}_1$ are two related tangents. If a cubic Hermite spline is used for interpolation of a monotonic data set, the interpolated function will not necessarily be monotonic, but monotonicity can be preserved by adjusting the tangents. In Figure 5.3 an example for the construction of a 1D-interpolation in z-direction is shown. A monotone piecewise cubic spline is used to obtain a smooth function from interpolation. The output spline preserves the shape of the data and at the same time respects monotonicity. In this manner derived overshooting artifacts are eliminated by the method. So as to say, it will not introduce extra or artificial surface information to the biological model. We project the biological model in a bounding box before we do the interpolation so as to neglect unnecessary interpolation calculation. Once the spline is constructed from each vertical column within the bounding box, the intensity of intermediate missing slices at the same column can be evaluated by providing different position values in the z-direction. Finally, the interpolated contour is extracted by setting

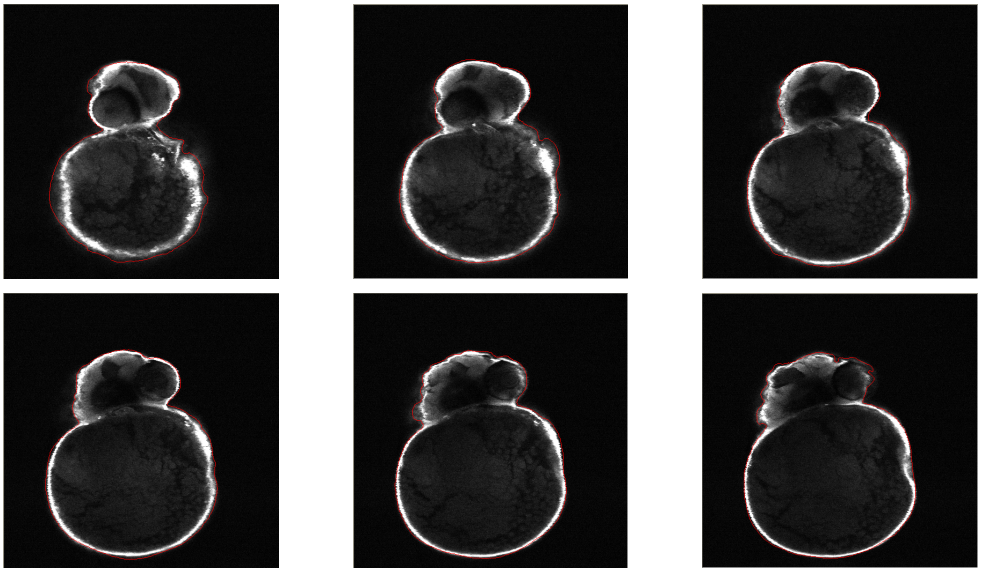

Figure 5.4. Example of original images of zebrafish embryo from confocal microscope.

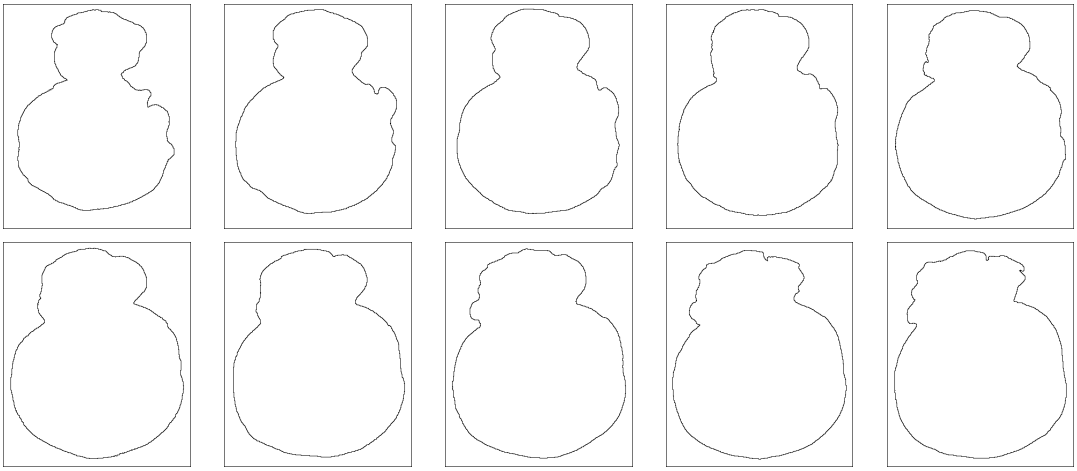

Figure 5.5. Example of contour interpolation of zebrafish embryo.

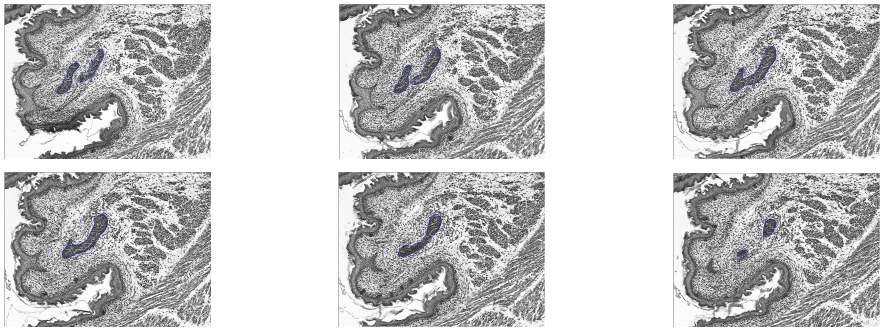

Figure 5.6. Example of original images of mammary gland from bright field microscope.

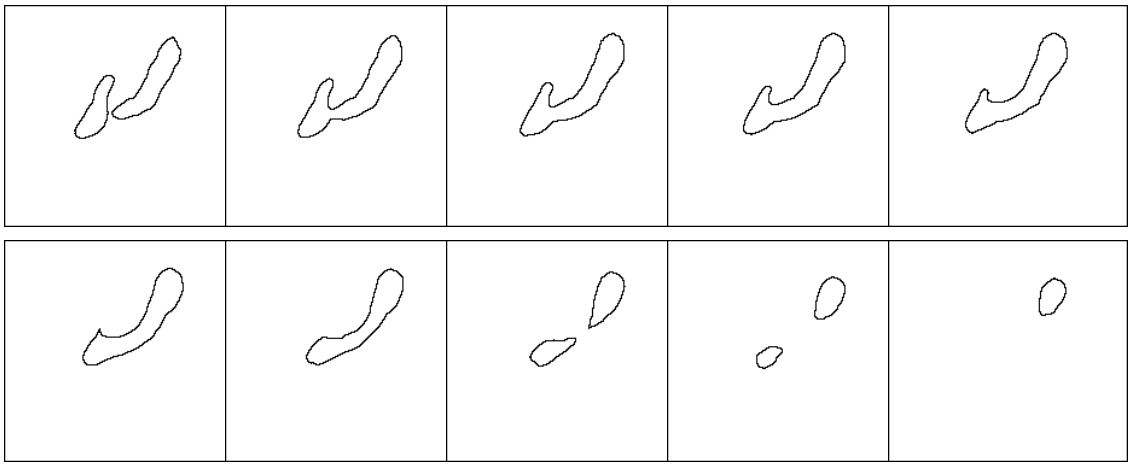

Figure 5.7. Example of contour interpolation of mammary gland.

the threshold of gray-value to zero for each slice. This approach results in an interpolated and equidistant sampled boundary for the model. The number of extra slices we have added for our model is based on the amount of difference in resolution at x,y directions and at z direction. For example, we capture a zebrafish embryo with a confocal microscope using a 10x objective (N.A. 0.5). The average volume of the zebrafish embryo is 0.1136 cubic millimeter. The pixel size in x,y direction is 0.821 µm and the optical cutting distance in z direction is 5 µm. Therefore, we added 6 extra slices in between two consecutive slices to obtain an equidistant sampling.

5.2.2 3D surface reconstruction

In order to be able to use the point cloud based reconstruction method, the stack of binary contour images needs to be converted into a point cloud in 3D space. Each pixel is converted to a point in 3D space taking the corresponding z-position of the slice into consideration. In this manner the point cloud is created without losing any detail and at the same time it is indisputably oversampled in both x,y and z directions. From a previously performed evaluation of point cloud based reconstruction methods [Cao and Verbeek, 2013], we concluded that the Poisson reconstruction method [Kazhdan et al., 2006b] performs the best for taking shape preservation and noise suppression into account. The Poisson reconstruction method, however, requires an oriented point cloud as an input. This means the method does not only need the location but also the normal of each point in the point cloud data. Therefore the normal for each point in the point cloud data is calculated using Hoppe's algorithm [Hoppe et al., 1992]. The normal of a point X_i is determined by gathering together the k nearest points to X_i; expressed as a nearest neighborhood function (Nbhd). The tangent plane of X_i is constructed as the least squares best fitting plane to *Nbhd(X_i)*. The normal of point X_i is calculated using a principle component analysis. The covariance matrix of *Nbhd(X_i)* is formulated from:

$$Cov = \sum_{y \in Nbhd(X_i)} (y - o_i) \bigotimes (y - o_i) \tag{5.2}$$

where $\bigotimes$ denotes the operation of outer product vector. y is one point in the nearest neighborhood set. o_i is the centroid of *Nbhd(X_i)*. The normal of point X_i is either positive or negative of the smallest eigenvalues of *Cov*. The positive or negative selection depends on the consistency of orientation of nearby tangent planes.

After having obtained on oriented point cloud data set, the Poisson reconstruction method is applied to create a precise and smooth surface for the model. If necessary, the resolution of the resulting surface model can be tuned by changing the scale parameter which is part of the Poisson reconstruction method. We evaluated the effect of the scale parameter on the reconstruction step by chang-

ing the scale value and compare the error between the ideal and real output with the analytical models. The scale parameter we have used here is based on this evaluation and sufficient for the biological model reconstruction (scale=2). The scale parameter still retains sufficient details on the surface for phenotype measurement.

5.2.3 Phenotype measurement

With the reconstructed surface model, we need to find a way for 3D shape description so as to distinguish a difference in phenotype with various treatments. The type of measurements extracted from the 3D model strongly depends on the model at hand and the hypothesis posed to resolve phenotypical differences. We extract a range of different features as shown in Figure 5.8, some are derived directly from surface including global shape, i.e. volume and surface area, and local features such as surface curvature per point.
More features can be extracted from a graph based representation of the shape, i.e. skeleton or centerline. These features encode geometrical and topological shape properties in a faithful and intuitive manner [Akgül et al., 2009]. The centerline is useful to describe the topology information of tubular structures such as blood vessels. Additional features can be extracted from the centerline such as number of branches and nerves, average branch-length, number of bifurcations, and so on. These basically follow from the graph structure.

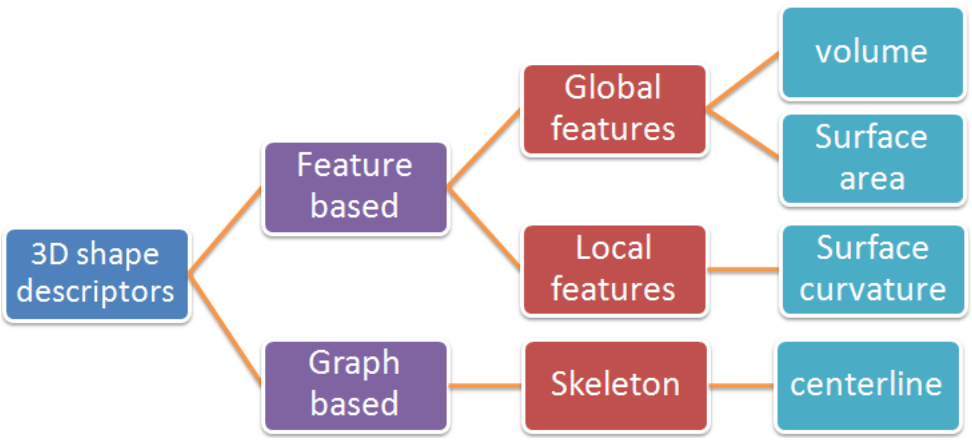

Figure 5.8. 3D shape descriptors.

5.3 Evaluation of the methodology

After the illustration of the methodology of model optimization, we continue with the evaluation of several important steps. We have three main steps as shown in Figure 5.1. Apart from the 3D surface reconstruction step, it is a parametric free pipeline. The step of 3D surface reconstruction is already evaluated in our former work [Cao and Verbeek, 2013]. In this section, we will look in detail on the contour interpolation, because this method might introduce interpolation error when the model reaches to a higher level of complexity. We want to check how well our solution is in dealing with different kinds of models. The second evaluation is given a general view on the level of improvement of the surface reconstruction compared to methods used earlier.

5.3.1 Evaluation of interpolation method

The interpolation by the 1D monotone piecewise cubic spline can introduce inaccuracies for topologically complex 3D models that are common in biology. Thus, in order to check the topological correctness of this important processing step applied to the 3D model, we also use a more complex 3D model for our evaluation. To this end the mammary gland is very suitable because it has a higher level of complexity in the shape structure, i.e. branches.
We design following evaluation method. The interpolation part is a crucial step in the construction of the relationship between slices and at the same time the correct topology of the model needs to be preserved.

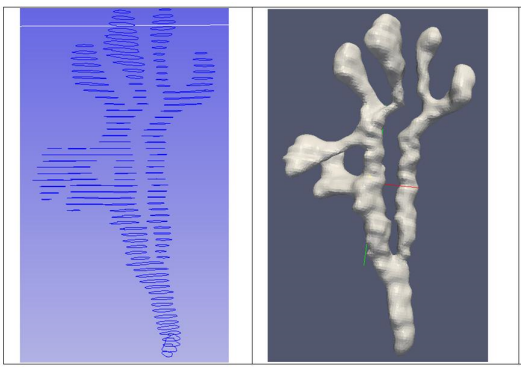

Figure 5.9. (a) original contour sections; (b) surface model.

Table 5.1. Evaluation result of interpolation part

Model name	#Contours	#Incorrect contours	Percentage
DES	1126/1271	0/0	100%/100%
EP	904/508	4/9	99.56%/99.01%
OLIE	852/1071	0/0	100%/100%
WT	746/924	0/0	100%/100%
Total	7402	13	99.82%

DES: a group exposed to a range of concentration of diethylstilbestrol; EP:a group exposed to a cocktail of estrogen and progesterone; OLIE: a condition control group exposed to an inert component; WT: a control group which is not exposed.

Note: Only in EP there is a problem.

• Therefore, first of all, we labeled the branches in original model with different IDs as shown in figure 5.9(c).
• Next, we manually annotate each contour derived from interpolation method with the same ID system relating to a specific branch by checking the correlated location on the output surfaces.
• Subsequently, we validate each contour ID in one section from the interpolation method with the corresponding contour ID in two closest slides from original model.

In this manner, we know how many contours from interpolation method mismatch with each other. By treating each contour as an individual object, we finally calculate the percentage of correctness.

From a selection of 8 mammary gland models that are obtained from species that have been exposed to different conditions (cf. Chapter 6) the evaluation result is shown in Table 5.1. These models are constructed through physical sectioning with a standard histology staining and acquired on a section by section basis with a bright field microscope. Therefore, it is undersampled in Z direction and also deformed. The incorrect contours we found were mostly because two contours are too close to each other, the interpolation method cannot nicely separate them. However, the percentage of correctness is still high which shows that the interpolation method can properly preserve the complex topology such

as in our mammary gland models. Thus, we could confidently apply this method in our process.

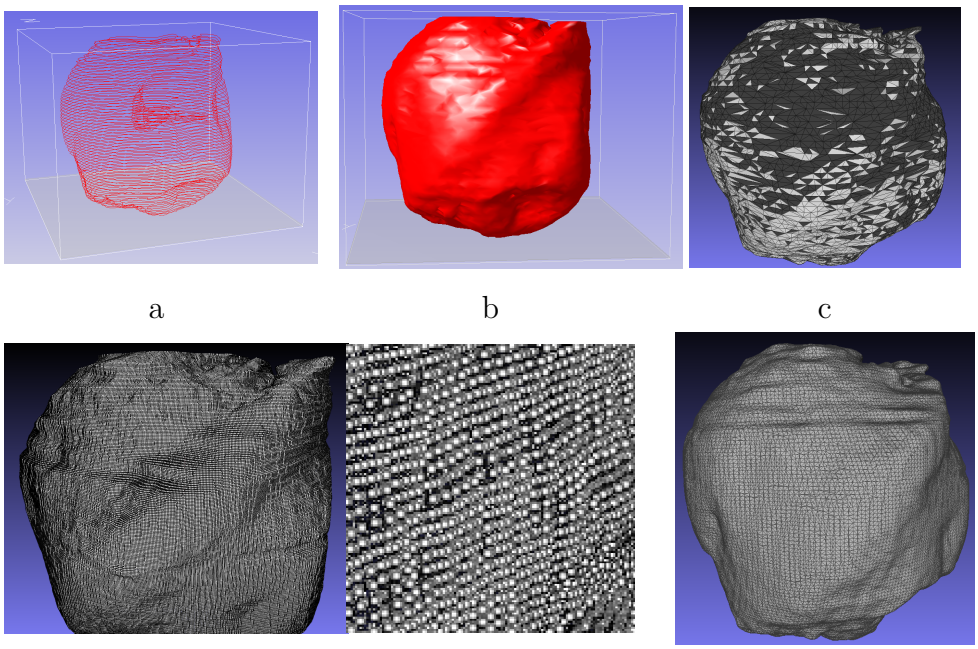

Figure 5.10. Comparison between two reconstruction methods. a. stack of contours; b. surface model from Boissonnat method in TDR; c. surface model from Boissonnat method in Meshlab; d. interpolated point cloud; e. close view of the interpolated point cloud; f. surface model from Poisson reconstruction method.

5.3.2 Evaluation of surface reconstruction method

The requirements of the surface quality for phenotype measurement are two fold. First, the surface should have a consistent surface orientation. Second, the surface should be a closed 2-manifold surface without holes on it.

A method that we successfully used for contour-based reconstruction is designed by Boissonnat and Geiger [Boissonnat and Geiger, 1993; Verbeek et al., 1995]. Their method is based on tetrahedralization of a volume. The method uses the medial axis to correct a nearest neighbor connection between adjacent slices. It is good at reconstructing complex contours such as complicated branching patterns and topologies with holes. However, extra postprocessing is required so as to

make the surface model ideal for phenotype measurements.
However, we need extra processing to adjust the output surface for the phenotype measurement. As we can see from Figure 5.10c, the reconstructed surface model does not guarantee a consistent orientation of the faces. We need post processing to reoriented the faces. Furthermore, a closed surface is a compact connected 2-manifold. But the surface model has some not 2-manifold faces which makes the re-orientation of the surface even harder, since we need to find the location of the problematic faces, delete it and try to fill the holes on the surface. These problems can be addressed by the Poisson reconstruction method as shown in Figure 5.10f. It is an implicit reconstruction method which consider all points as a whole. The output surface is closed and consistently faced. Additionally, the surface is much smoother with more characteristics preserved.

5.4 Results

The dataset resulting from the surface reconstruction method is used for the shape analysis. In this chapter, we will illustrate this with models obtained through confocal imaging i.e. the point cloud of zebrafish embryos.

5.4.1 Zebrafish embryo, measurement verification

We want to illustrate that the surface reconstruction process can be very well applied to a stack of images. As a test data set, an experiment with confocal image stacks of zebrafish embryos are used. The images are part of an experiment that consists of two treatments and therefore two different groups; i.e., a control group that develops under normal oxygen levels and a treatment group that develops under a condition of hypoxia; i.e. oxygen deprivation. For each stack, a 3D model of the embryo is constructed by extracting embryo contour per slice. In total the set consists of 21 embryo models (14 with normal treatment, 7 with hypoxia treatment). In Figure 5.11(a) and (b) an example of embryo models with different treatments are shown.
For each model we calculated the surface area and the volume. The result from the point-cloud reconstruction to shape measurements is a triangulated surface.

The surface area is computed by integration over all the triangle patches on the surface. The volume is calculated directly from the grid using divergence theorem introduced in [Zhang and Chen, 2001]. For an objective assessment of the differences between two treatments, we use the sphericity [Wadell, 1935] as shape descriptor, described as follows:

$$\Psi = \frac{\pi^{\frac{1}{3}}(6V)^{\frac{2}{3}}}{A} \tag{5.3}$$

where V represents the volume of the object and A represents the surface area of the object. The sphericity is a shape descriptor and for a sphere it equals 1. The higher the sphericity of the object the more it resembles a perfect sphere.
Our dataset is not guaranteed to adhere to a normal distribution. To test for differences, the Kolmogorov-Smirnov Test (KS-test) is used [Massey, 1951b]. The KS-test is a better choice than Student t-test when the dataset is not guaranteed to adhere to a normal distribution. Sphericity is computed for all our models and thus mean and standard deviation of the set are available. We can classify two groups on the basis of the measurement of sphericity. The results are depicted in Figure 5.11(c) and Table 5.2. On the basis of the measurements we could classify into two classes. The test results indicate that sphericity of the control group is significantly smaller than that of hypoxia group. This is consistent with the biology; the hypothesis states that the embryo is spherical at the very beginning and starts to unfold during the development. Hypoxia slows the development of the zebrafish embryo. Under normal levels of oxygen the development is faster. The embryo develops uneven in different directions and does not resemble the spherical shape anymore that it started from. The development of embryo with hypoxia, however, is restrained by the lack of oxygen as a result the shape is closer to spherical state that it started from.

Table 5.2. Measurements of Zebrafish embryo

Type	A(mm^2)	σ	V(mm^3)	σ	S	σ
Normal	0.3397	0.0209	0.0127	0.0007	0.7759	0.037
Hypoxia	0.3568	0.02695	0.0154	0.0016	0.8388	0.0136

A=Area; V=Volume; S=Sphericity; σ=Standard deviation.

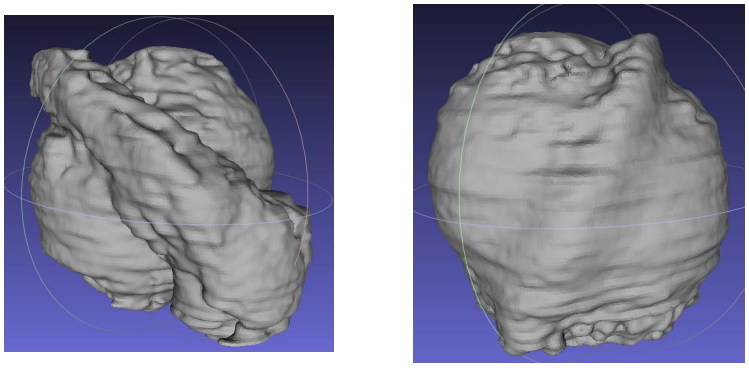

(a) (b)

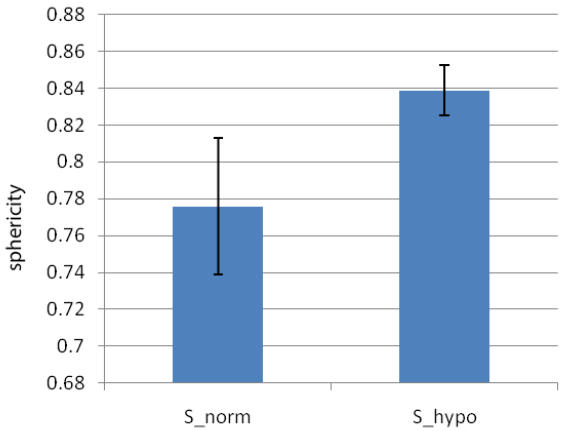

(c)

Figure 5.11. Results of Zebrafish embryo (a) Normal condition (b) Hypoxia condition (c) Bar chart of sphericity feature indicating the constrained embryo development under the condition of hypoxia.

5.5 Discussion & conclusion

In this chapter, we have computed a system for 3D representation and analysis from stack of images through a 3D model representation that is derived from that stack. We intend to use the representation for phenotype analysis. The input data for our system is a stack of images whose annotation and alignment are completed. However, the 3D model starts undersampled which is fine for visualization but not for quantification and therefore optimization is required. To that end a

point cloud based reconstruction method is used. In this manner the stack of contours in the model is efficiently converted into a uniformly distributed point cloud in 3D space. As such it changes a specific contour based reconstruction problem to a much more generalized point cloud based reconstruction method. Since we take all the 3D points at once to construct the surface representation it makes full use of the boundary point cloud relationship in 3D space. In this way we overcome the restriction imposed by the stack of contours which does not efficiently use the relationship in the z-direction. From former results [Cao and Verbeek, 2012, 2013] we have learned that the Poisson reconstruction method performs well in both shape preserving and noise suppression. This is confirmed in our current study.

Our purpose, i.e. representation and analysis of 3D biological models, the analysis pipeline presented here combines all best techniques and helps us observe the real situation. The verification of the pipeline which includes evaluation of important steps and zebrafish embryo surface analysis confirms the potential of our system in dealing with shape related studies in biology. The pipeline is applicable to different kinds of datasets that originate from different microscopes and sampling conditions. The number of additional slices interpolated in between two consecutive slices are defined by the differences in resolution at x,y direction and z direction. The complexity that one can find in micro-anatomy can be well covered by the pipeline. The pipeline needs further tuning though the type of models that we have now worked with illustrate the soundness of the pipeline. Henceforward, we will continue to develop this pipeline and include more techniques to be able to deal with the large variation of experimental settings for 3D phenotype analysis in biomedical research.

Chapter 6

Phenotype analysis of arborized structures from 3D models

Extended from:

L. Cao, F.J. Verbeek. Nature inspired phenotype analysis with 3D model representation optimization. The 4th International Conference on Innovations in Bio-Inspired Computing and Applications,Ostrava, 2013

Abstract: In biology 3D models should reflect nature as close to true nature as possible that these models can be used for a accurate analysis. The visualization of these models helps in the further understanding and conveying of the research problem. In Chapter 5 we have introduced a solution of 3D model representation optimization. We verified our pipeline under different levels of complexity of 3D structures. In this Chapter, we further focus on the investigation of complex structures from lactiferous duct of newborn mice to gain understanding of the 3D structure and the deviation as a result of enviromental factors. We make use of Lindenmayer systems (L-systems) and the results of our analysis for gaining understanding of lactiferous duct development. The approach also produces a framework for analysis of complex 3D models derived from 3D images.
The optimized 3D models we obtain through the pipeline of Chapter 5 are used in the analysis of phenotypical differences originating from experimental conditions by extracting related shape features from the model. In order to make sure we can extract the branching structure in the right manner we make use of the centerline extraction method and further design an evaluation method to verify the method. We consider that the lactiferous duct has an innate blue-print of its arborazation and assume this blue-print is kind of rewriting rule as can be simulated with an innate L-system. We analyze the duct as it is exposed to different environmental conditions and reflect on the effect on the innate L-system.
Our method can deal with the complex 3D models, the features separate the experimental conditions. The results provide a means to reflect on the manipulation of an L-system through external factors.

6.1 Introduction

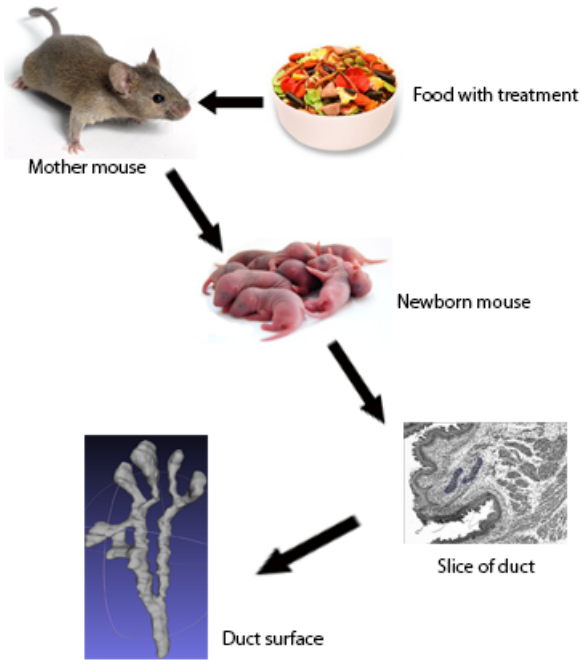

Figure 6.1. Overview of the data acquisition process.

In the previous Chapter we have illustrated the optimization of contour based reconstruction method. We make use of the method for the optimization and surface reconstruction of a complex structure: lactiferous duct of newborn mice. The study of the lactiferous duct aims to illustrate the effect of substances in the environment that mimic hormones and therefore have a potential effect on development of sexual organs or secondary sexual organs. This effect is known as endocriene disruption [Mandrup et al., 2014]. The study consists of 4 groups. In the data set presented here 4 different conditions are introduced; meaning that through the food the mother was exposed to these conditions and we would like to measure a maternal effect in the offspring. The control group: wildtype is not exposed (WT). A conditional control group is exposed to an inert component (OLIE). One group is exposed to a range of concentrations of diethylstilbestrol (DES). Another group is exposed to a cocktail of estrogen and progesterone (EP) in a range of different concentrations. An overview of the experiment is shown

in Figure 6.1. From the reconstruction it shows that the mouse lactiferous duct has distinct tree-like structure as depicted in Figure 6.2.

We want to illustrate the capability of our 3D representation method in dealing with complex structures and introduce a workflow for 3D phenotype analysis. This Chapter therefore focuses on the extraction of the complex topological features to detect the morphological changes under different treatment conditions. Graph based measurements have the potential of encoding geometrical and topological shape properties in a more faithful and intuitive manner [Akgül et al., 2009]. The skeleton is one of them defined as a thinned version of the shape of which all elements are equidistant to its boundaries. In 3D, skeletons generally contain surface patches. Centerline is a special case of the skeleton in which the skeleton is simplified to a 1D representation of the original 3D object, consisting only of curves [Dey and Sun, 2006]. In case of an arbor-like structure, the centerline is derived from the two outermost sections of an arborized structure which locally maximizes the distance from the boundary [Piccinelli et al., 2009]. The centerline describes the topology information of arborized structures in a compact and efficient way.

Numerous centerline extraction methods have been presented for medical imaging. They can be separated into three categories: topological thinning, distance-based methods and polygon-based methods.

The topological thinning deals with a volumetric dataset. Boundary voxels are iteratively peeled off according to topological rules until the whole volume has been peeled and left with the centerline [Lee et al., 1994; Xie et al., 2003]. Thinning procedures usually create centerline connected of one voxel thick. However, undesirable small branches are also created on coarse object boundaries due to the principle of end-point preservation. End-point means that the point on the one voxel graph has less than 2 neighbors. As a result, the topological thinning method needs to be coupled with an efficient pruning method [Nmeth et al., 2010].

Distance-based methods compute the boundary distance transform and find the centerline as the local maximum or ridge. However, the output centerline is usually disconnected, not guaranteed to be one voxel thick, and quite sensitive to noise on the boundary [Cardenes et al., 2010; Van Uitert and Bitter, 2007]. The reason is that the local maximum extraction might produce a surface based skele-

ton and not a centerline. There would exist a planar set of voxels in the middle of the object which would comply with the local maximum criterion [Telea and Vilanova, 2003].

The polygon-based methods directly deal with the surface and the output centerline is suitable to topological analysis of arborized structures. It is useful to obtain a centerline of a complex; e.g. arborized network. It however is a heuristic method which lacks a sound theoretical framework and guaranteed solution [Piccinelli et al., 2009]. In our case it has shown to perform well.

The centerline preserves the minimal topology of an arborized surface, therefore, for our research, the features from the centerline can be used to describe relevant parts of the arborization structure. Furthermore, several prominent features that distinguish the various treatment groups are helpful in the construction of a formalized system. To that end we investigate the connection from an arbor-like structure to an L-system [Lindenmayer, 1968; Rozenberg and Salomaa, 1980, 1986] and reason over the phenotypical effects as a result of different conditions to which the subjects have been exposed.

The L-systems have been applied successfully in arborizations such as neural tissue [Ascoli and Krichmar, 2000; Jelinek et al., 2002]. The computational construction of neurons using L-system provide an efficient and reliable method to investigate the relationships between neuromorphology and neurophysiology [Ascoli, 1999; Jelinek et al., 2004]. The mammary gland also has a noticeable branching feature; as a result, we intend to use L-system to simulate the mammary gland structure. L-systems were firstly introduced as a mathematical system to describe the developmental patterns of algae in 1968 [Lindenmayer, 1968] by a theoretical biologist: Aristide Lindenmayer. Subsequently, Lindenmayer's method was extended with a geometric interpretation and became a versatile method for plant modeling. In general, an L-system is a system of rewriting. Rewriting is a technique for defining complex objects by successively replacing parts of a simple initial object using a set of rewriting rules or productions [Prusinkiewicz and Lindenmayer, 1990]. The most known rewriting rules operate on character strings. L-systems are one of them with distinctive characteristics. Specifically, L-systems consist of two trivial elements: an axiom, and a set of productions. The axiom is the starting point of the rewriting process. The set of productions are the

derivative rules. In L-systems, the productions are applied on a parallel and simultaneous manner replacing all letters in a given string.

6.2 Methodology for arborization structure analysis

In order to understand the arborization structure we first have to extract the topological features from the optimized 3D surface model. We investigate how this can be accomplished with a minimal representation of the topology of a model i.e. the centerline. It facilitates quantitative analysis of the arborized structures. Arborization structure analysis is discussed in many areas. Researchers have recently proposed methods to trace neurons or reconstruct the neuronal structure by tracking arborized line structures in a 3D image volume [Lee et al., 2012; Zhao et al., 2011]. The quantitative analysis of the tree is substantially simplified by transforming a voxel-level tree object into a set of interconnected single-voxel centerlines representing individual tree branches [Kalman et al., 2006].
Centerline analysis is also used for the blood vessel quantification and meaningful parameter extraction from 3D vascular images [Kang et al., 2009].
All considered, we have therefore chosen the centerline extraction method. Extra and useful topology related and relevant measurements for the analysis of the lactiferous duct structures, can be extracted from the centerline; i.e. number of branches, average length of branches, number of bifurcations, and so on.

6.2.1 Centerline extraction

Polygon-based centerline extraction method can create a connected one voxel thick centerline without the undesired small branches. Futhermore, it can be implemented in fully automatic fashion which help to prevent subjective information entering into the process; i.e. the approach make the subsequent phenotype measurements more objective. The method we implement in our workflow is a mesh-based centerline extraction created by Piccinelli et al. [Piccinelli et al., 2009] for identifying vessel bifurcations and arborized network organization. First,

the algorithm identifies the bifurcations by analyzing the whole network of the arborized model with a moving sphere. In this manner the method is able to decompose the network into bifurcations and single branches. Since the complexity of the algorithm is linear with the number of surface mesh vertices, it is very efficient. There are, however, some limitations. Nested bifurcations with a very short distance between each other may be grouped into a single bifurcation if the probing sphere radius on the junction part is greater than the distance between the bifurcations [Piccinelli et al., 2009]. Centerlines can extend outside the model if the boundary has a particularly non-convex shape [Piccinelli et al., 2009]. As a result, we evaluate this centerline extraction method in section 6.3 so as to check the performance specifically, with our dataset in mind.

6.2.2 Evaluation of centerline extraction method

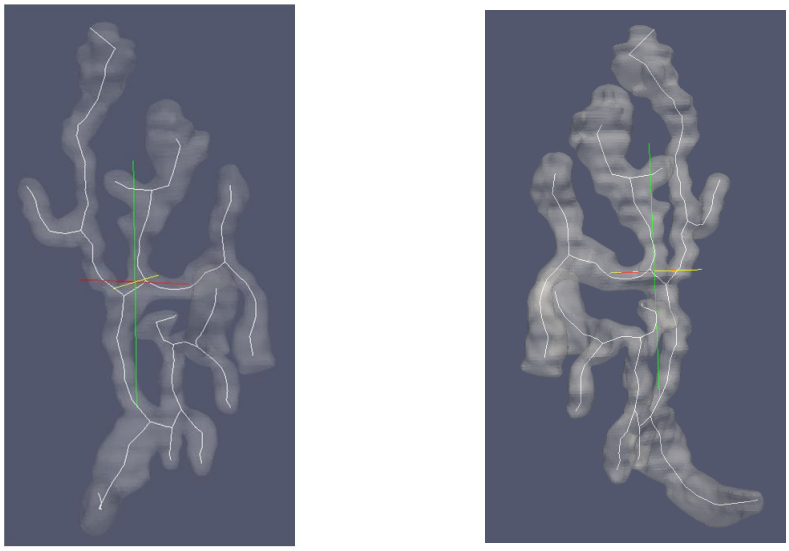

Figure 6.2. Branch structure and surface model with opacity.

Since the centerline extraction method has its limitations, it would be necessary for us to evaluate it in our own dataset. With a good evaluation, we can safely continue with the measurements, classification and modeling. The ground truth for the evaluation is the original surface model. We verify the correctness of the centerline in the ParaView software environment [Henderson, 2004] as shown in Figure 6.2. We compare each branch and bifurcation between original model and

Table 6.1. Evaluation result of centerline extraction method

Model name	#Branch	#Bifurcation	#Wrongly connected branch	#Low quality bifurcation
DES_1	6	3	0	0
DES_2	11	5	0	0
DES_3	5	2	0	0
DES_4	21	9	0	0
EP_1	11	7	1	1
EP_2	7	3	1	0
EP_3	25	12	1	0
EP_4	23	11	1	0
OLIE_1	17	8	0	1
OLIE_2	17	8	0	0
OLIE_3	5	2	0	0
OLIE_4	9	4	0	0
WT_1	7	3	0	0
WT_2	9	4	0	0
WT_3	5	2	0	0
WT_4	5	2	0	0
Total	183	85	4	2

DES: a group exposed to a range of concentration of diethylstilbestrol; EP:a group exposed to a cocktail of estrogen and progesterone; OLIE: a condition control group exposed to an inert component; WT: a control group.

cneterline so as to make sure they are extracted correctly. In [Piccinelli et al., 2009] there are two limitations for this method. One is the failed identification of two bifurcations which are too close to each other. The other is the centerlines that can extend outside the "ducts". In the mammary gland model, however, we do not find so many exceptional cases. In some cases, we find branches that are connected wrong. Some of the bifurcations locate far from the arbor center and do not nicely represent the original topology. Therefore, in an initial evaluation,

we focus on number of branches wrongly connected and the low quality bifurcations. We have randomly selected 16 out of 42 mammary gland models with automatic extraction of the centerlines and calculate the number of branches and bifurcations per model as well as the wrongly connected branches and low quality bifurcations. The results are shown in Table 6.1.
As we can compute from Table 6.1, 97.81% of the branches are detected with correct topology of the tree structure in mammary gland. Those who are connected wrong which are mostly occurring in EP condition are due to the sequence that the topology structure is relatively complicated and some small portions of the surface from two branches stick together because they are too close to each other and the interpolation method cannot separate them apart. Additionally 97.65% of the bifurcations are properly situated in the model. Although the automatic extracted centerlines do not perfectly fit to the ideal centerline, it sufficiently detects most of the branches and bifurcations correctly. Conclude that we can safely apply this automatic centerline extraction method for our model and compute features from it.

6.3 L-system construction

Within the feature set we have obtained from our experiments, we look for features that is prominent in representing phenotype changes of mammary gland under different treatment. Subsequently, we can generate a general L-system for mammary gland simulation by making use of these features.
The mammary gland that we study with is from newborn mouse whose mothers were exposed to different endocrine-like components. It is in the stage of secondary sprout: lactiferous duct or epithelial cords. In human, the amount of lactiferous ducts could reach to 10-20 for each nipple. However, in the mouse embryo, only one epithelial cord grows from the mammary bud. Thus, only one lactiferous duct exists for each nipple. This initial round of branching growth results in a primary duct with several initial branches [Cowin and Wysolmerski, 2010].
After extracting several prominent branch features from the centerline of actual 3D lactiferous duct, we would introduce these morphological features into an L-

system to model simulation of the lactiferous duct.
The platform we have chosen to construct the L-system model for lactiferous duct is L-Py: an L-system simulation framework for modeling plant architecture development based on the Python language [Boudon et al.]. We use a dynamic language to enhance the development of lactiferous duct growth models. It provides seamless control of the differential turtle geometry [Prusinkiewicz and Lindenmayer, 1990]. The turtle is a drawing tool for the geometric interpretation of a character string as a sequence of segments. During the string reading, the turtle moves on the line with varying segment lengths and angles. The turtle can move in the 3D space based on differential geometry and using quantities such as local tangent, curvature, and step size [Boudon et al.].
As for our first construction of lactiferous duct model using an L-system as described in a pseudo code of Algorithm 1, the production rules mainly focus on realizing the elongation and bifurcation of the duct. The measurements that we integrate in the system include branch length, curvature, radius and the number of branches. These features are the prominent ones based on our previous study to distinguish the morphological variation of lactiferous duct with various treatments. The way to integrate branch length, curvature and the radius of maximal inscribed sphere are relatively straightforward. The changing number of branches is realized by changing the probability of bifurcation construction. The probability density function we use is the uniform distribution.

6.4 Results

6.4.1 material and preparation

Our study is based on 3D model of the lactiferous duct of newborn mice. There were 4 different conditions introduced: control group consisting of 7 models; a condition control group as shown in Figure 6.4(c),(d) consists of 12 models; a treated group exposed to DES consists of 8 models in different increasing concentrations; another treated group exposed to EP shown in Figure 6.4(a),(b) consists of 8 models in different increasing concentrations. The distinct tree-like structure

of the wildtype mouse lactiferous duct is depicted in Figure 6.2.

Algorithm 1 Pseudo code for L-system

```
Initialize maximum number of branch order to 4
Initialize increment of radius through time to 0.0001
Initialize maximum duration of a branch relating to the branch order
Initialize branch angle with a random number from 15 to 25 weighted with
the branch order
Initialize branch angle to a random number from 3 to 7
Initialize total number of iteration of the system
for time is smaller than iteration time do
    Set time to zero
    Set branch order to zero
    if time is shorter than maximum duration of a branch then
        Continue growing with a set branch angle and length
        Set time to time +1
    else
        Create bifurcation with a set roll angle around the previous branch
and a set angle in between the bifurcation
        Set branch order to order +1
    end if
    Decrement radius of the branch
end for
```

The 3D models are obtained from serial sections and acquired with a dedicated bright field microscope imaging setup [Boon et al., 2000]. The images of the lactiferous duct are acquired and a stack of aligned images is used as input for the 3D model [Verbeek and Huijsmans, 1998; Verbeek et al., 1995]. For each stack the lactiferous duct structures are delineated by a specialist resulting in initial 3D models.

For all models, model optimization (cf. Chapter 5) and surface reconstruction (cf. Chapter 4) is applied. Subsequently, the centerlines of all branches in the arbor-like structure are extracted. To derive the topological structure a known centerline extraction method is used as described in [Piccinelli et al., 2009]. We use the centerlines to assess the topological shape differences in the models. These centerlines are also the basis for the L-system representation.

For each of the models from each global centerline we extract individual branches.

For each branch we calculate phenotype measurements including branch length, curvature, torsion, tortuosity, minimal radius, maximal radius, mean of the radius and median of the radius. The curvature of a branch is defined as the average curvature over all branch-points. The curvature of a point is the inverse of the radius of the local osculating circle, i.e.

$$K = \frac{1}{R} \tag{6.1}$$

where, K is the curvature of a point and R is the radius of the local osculating circle. The torsion is defined as the degree by which the osculating plane rotates along the line [Pressley, 2010]. The tortuosity is defined as the ratio between the branch length and the distance of the branch end-points. The radius is defined as the radius of maximum inscribed sphere for each point.

6.4.2 Prominent feature extraction

The main focus of this study is topological shape description for 3D geometrical models derived from microscope image. We have obtained experimental data from the development of the lactiferous duct; in early development a mouse embryo is exposed to different environmental factors. These factors a.k.a. endocrine disruptors influence development of reproductive organs in primary and secondary stages by altering the structure of the duct.

Changes in the duct configuration are considered changes in the innate layout of the duct. The innate layout can be modeled with an L-system. So, changes in the duct layout changes the innate coding of the L-system and this will result in a different structure or phenotype. We measure the phenotype in order to show the effect of the environmental factor and at the same time we can reason from the result how the L-system is affected.

Our question is whether we can accurately separate complex 3D structure using measurements. We construct a dataset by collecting all the branches with measurements from the same treatment groups. Because the measurements are not all normally distributed, we use the KS-test to check significant differences for every measurement.

The hypothesis is that DES and EP will have an effect on the development of the lactiferous duct; this effect should not be seen in the OLIE and WT group in which development should not be affected at all. We treat the OLIE and WT group as our ground truth. The DES and EP group should be very dissimilar from the OLIE and WT group. We therefore employ the KS-test to compare three groups with the null hypothesis that the compared groups are from the same continuous distribution: one between the groups DES and EP (DES-EP); one between the groups OLIE and WT (OLIE-WT); the other one between the combined groups DES with EP and OLIE with WT (DE-OW). In Table 6.1 the results are shown. The p-value refers to the significance level. If the test rejects the null hypothesis at the set significance level, the result value h is 1 or -1. Value h is 1 if the first dataset is significantly larger than the second. Value h is -1 if the first dataset is significantly smaller than the second dataset. Otherwise, value h is 0. The significance level was set to $p = 0.01$. From the results we can see the KS-test cannot reject the null hypothesis between group OLIE and WT which means these two groups are from the same continuous distribution. Group DES and group EP are almost the same except for the curvature, because the group EP has more curved branches compared to the group DES as we observed during the evaluation of centerline extraction method (cf. Chapter 5). Nevertheless, the combined group DES with EP and group OLIE with WT are significantly different in length, curvature, maximal radius, mean of the radius and median of the radius. These features are prominent ones over torsion, tortuosity and minimal radius. The results support the hypothesis and also confirm the feasibility of our 3D analysis for such complex system.

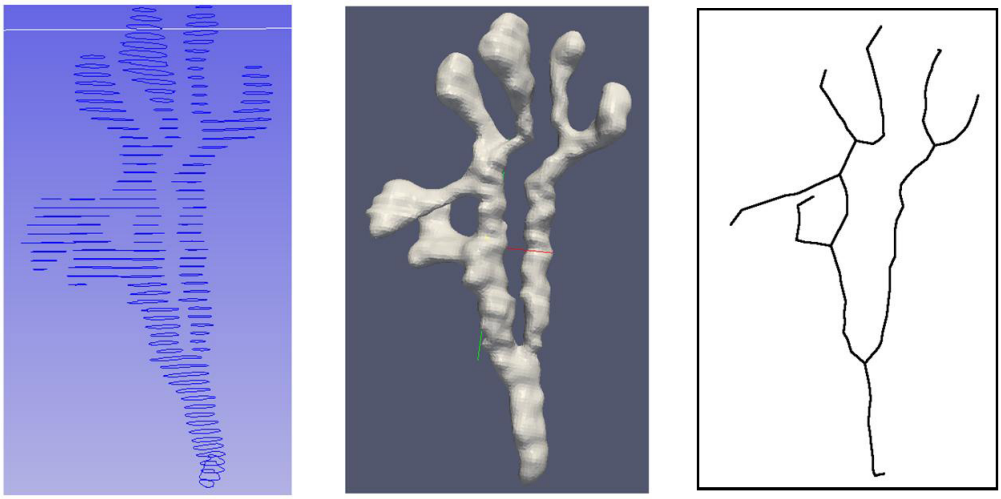

Figure 6.3. (a) original contour sections; (b) surface model; (c) centerline.

Table 6.2. Results of the different treatment groups

		length	curvature	torsion	tortuosity	min-radius	max-radius	mean-radius	median-radius
DES-EP	h	0	-1	0	0	0	0	0	0
	p	0.2027	0.0098	0.5588	0.8170	0.7951	0.6364	0.8275	0.9412
OLIE-WT	h	0	0	0	0	0	0	0	0
	p	0.2564	0.8537	0.7724	0.9246	0.0416	0.2951	0.1581	0.3943
DE-OW	h	-1	1	0	0	0	-1	-1	-1
	p	0.0043	0.0031	0.2714	0.5649	0.1007	4.99E-5	0.0026	0.0040

DES: a group exposed to a range of concentration of diethylstilbestrol; EP:a group exposed to a cocktail of estrogen and progesterone; OLIE: a condition control group exposed to an inert component; WT: a control group; DE: combined group of DES and EP; OW: combined group of OLIE and WT; h: the result of KS-test; p: the significance level of KS-test.

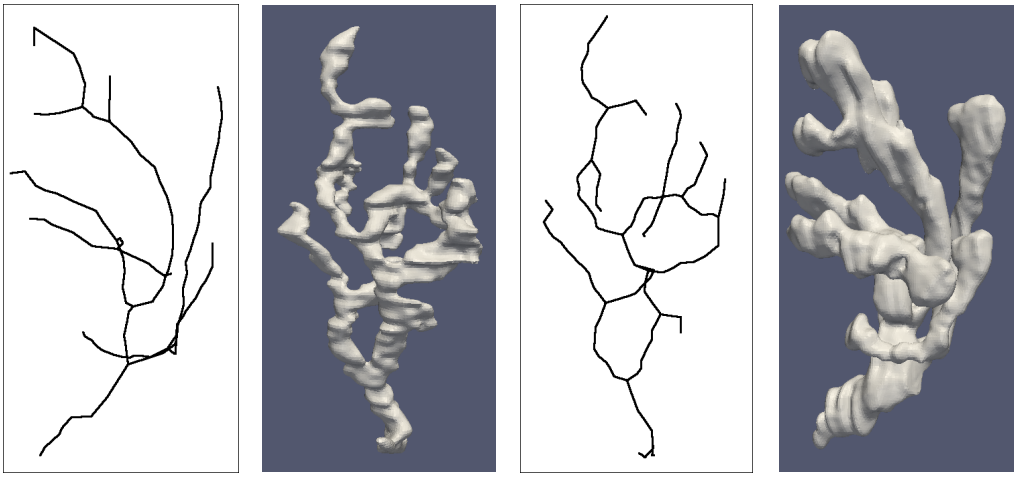

Figure 6.4. Different branch structures of lactiferous duct (a) surface model from group EP; (b) centerline of the model from group EP; (c) surface model from group OLIE; (d) centerline of the model from group OLIE.

6.4.3 L-system modeling

In this section, we intend to use the measurements, write production rules and built an L-system. This L-system model mainly focuses on the simulation of elongation and bifurcation of the centerline of the lactiferous duct. We show the simulation of our L-system model in two different kinds of lactiferous ducts: i.e. the wild type and the DES exposed type. The parameters are derived from measurement on 3D models as shown in Table 6.3.

Table 6.3. Input parameters of lactiferous duct

Type	MBL	σ_m	MBC	σ_m	MBR	σ_m	MBN	σ_m
WT	303.1	34.19	0.0096	0.0004	28.45	1.37	6.17	0.75
DES	193.1	12.85	0.0101	0.0003	27.90	0.74	14.625	3.19

WT: a control group which is not exposed; DES: a group exposed to a range of concentration of diethylstilbestrol; MBL: Mean of branch length in micrometer; MBC: Mean of branch curvature; MBR: Mean of branch radius in micrometer; MBN: Mean of branches number; σ_m: standard deviation of mean.

According to our findings, compared to wild type, the lactiferous duct with DES treatment would have significant difference such as more branches with shorter branch length. The result of our production rules and L-system visualization in

a virtual model of the lactiferous duct are shown in Figure 6.5.

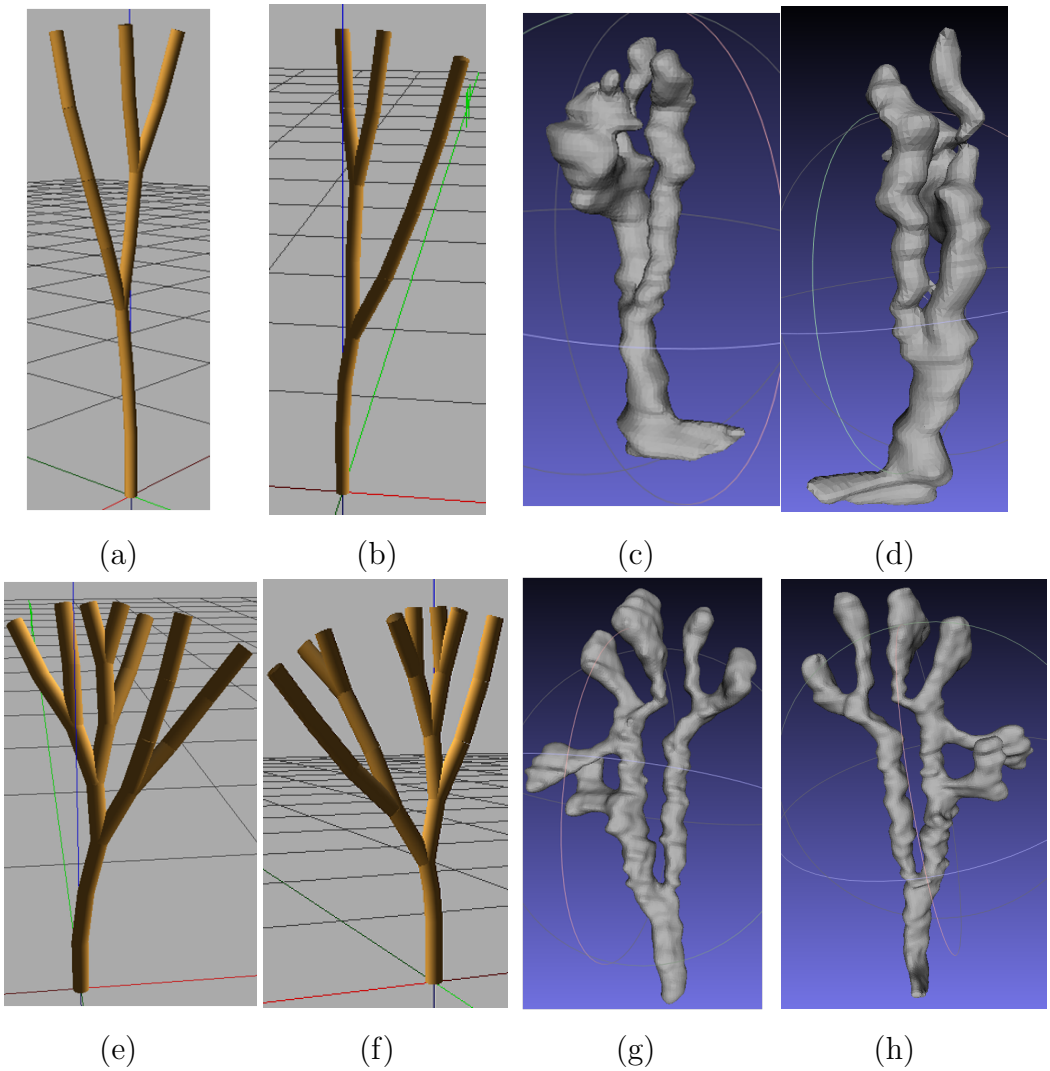

Figure 6.5. Resemblance between real surface models and L-system centerline simulation. WT centerline simulation (a) example 1 and (b) example 2; WT surface model (c) view 1 and (d) view 2; DES centerline simulation (e) example 1 and (f) example 2; DES surface model (g) view 1 and (h) view 2.

In addition, we reflect on the feasibility of ground truth of the L-system and introduce some constraints. We attempt to introduce a space constrain for the mammary gland development. Therefore, we introduce an ellipsoid as a fat pad and iterate our L-system model further to simulate the stage of puberty of the

mammary gland as shown in Figure 6.5. This is still a primitive model simulating the development of the mammary gland up to puberty stage. For a better simulation, we need extra quantified phenotype measurements to tune the model.

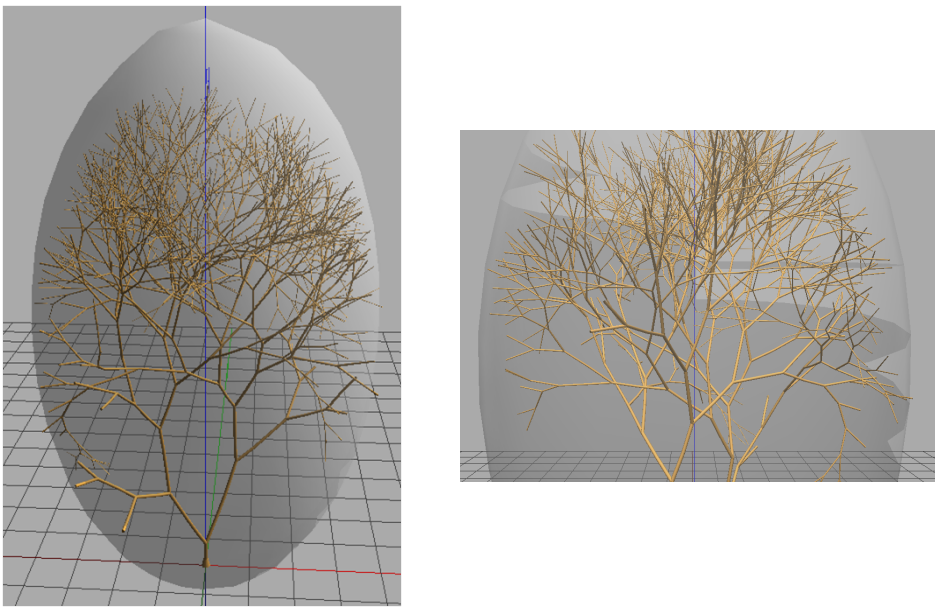

Figure 6.6. L-system simulation for the stage of puberty.

6.5 Discussion & conclusion

In this chapter, we focus on the analysis of complex 3D model with arborized structures. We study and analyze the rodent lactiferous duct under different treatment conditions. The aim is to use feature description to distinguish phenotypical changes with different treatments. We start with an optimized 3D surface model of the lactiferous duct using the method introduced in Chapter 5. We extract the centerline structure from the surface model so as to minimize the topological description. Phenotype measurements are calculated and prominent features are slected from centerline structure so as to analyse 3D models from mammary glands developed under exposure of different "potential" endocrine disruptors. We presented that we are able to differentiate the different conditions and characterize the effect of the exposures. In order to accommodate the branching structure that we analyze in a formal structure we invoke the L-system. This nature inspired formal system can help in the understanding of the branching; in

fact, we consider an L-system to represent the blue-print of the normal development of the branching duct. Our experimental results illustrate the change of the L-system under environmental conditions and the features we have derived represent the change in phenotype. At the same time the features from the various conditions represent the mutations in the L-system. Thus, this analysis of induced phenotypes helps us in bringing new inspiration to the manipulation of the L-system in which the features provide a quantifiable twist to this system. Our primary L-system model reports the potential for the simulation of mammary gland development and maturation. The L-system can provide a ground truth model from real data. Our research will be directed into this delicate interplay of nature inspired systems and nature driven models.

6.6 Acknowledgement

We wish to express our gratitude to Drs J. Lemmen and P.T. van der Saag who were involved producing the dataset for the rodent mamary gland in a range of different conditions. We thank J. Korving for taking care of the histological preparations. The imaging and reconstructions were completed using the setup of the Imaging & BioInformatics group.

Chapter 7

Conclusion and Future Work

In this thesis, different ways to represent and analyse biological models from image dataset are discussed. These image datasets can be two dimensional (x,y) or three dimensional (x,y,z; x,y,t). We have used different feature sets and feature extraction methods. We focus on finding patterns for analysis in multi-dimensions both with spacial and temporal series. The images are captured in sufficient qualities to be able to find patterns in a population. This can be a high-throughput screening but also three dimensional modeling approaches are probed. In each chapter, the ground truth is used for validation of phenotype analysis and method evaluation. In temporal two dimensions, i.e. time series, we focus on a biological study on epidermal growth factor receptor (EGFR) signalling and receptor degradation. The defect in the receptor mechanism is considered to be closely related to the breast cancer progression. We have provided a solution to analyse high-throughput image datasets on the level of protein location in Chapter 2. Moreover in Chapter 3, in a EGFR endocytosis study, we have introduced a Hierarchical classification strategy to improve the categorization of three dynamic phenotypes in the EGFR endocytosis process. In Chapter 4 we have changed our working field to spacial 3D datasets and use the extracted features for reconstruction method evaluation. In Chapter 4 we have presented error estimation for four representative 3D surface reconstruction methods by comparing analytical features derived from a surface model, thereby evaluating the quality of the surface model. In Chapter 5, we are making use of the conclusions drawn in Chapter 4 and build a system for 3D surface representation and analysis from stack of

images; basically this consists of an optimization of the geometrical model. In Chapter 6, we further use the surface representation workflow derived in Chapter 5 for complex 3D model reconstruction and analysis. In addition, we introduce the L-system as a model for ground truth construction.

7.1 Image analysis and Pattern Recognition in High-throughput Screens

The concept of high-throughput screening is used to visualize various cell structures. One HTS experiment may produce up to half million images which is a quality for which it is not possible to be analysed without a clearly formulated plan of automation. Therefore, an automated analysis solution for HTS experiments is required by combining image analysis and pattern recognition. Chapter 2 uses a 1D episode to represent the biological model. These categorized episodes are described by features extracted from 2D images and further confirmed through classification using a ground truth model. As a result, an automated system is constructed to extract phenotype measurements for each object and characterize the objects into three characteristic episodes in the EGFR endocytosis process. We illustrate that the phenotype measurements from segmented images and categorization of phenotypic episodes can be done successfully using feature selection and classification. The best trained classifier has been used to classify three EGFR phenotypic episodes. Two case studies show the capability of our solution in identifying characteristic episodes and analysing a large scale siRNA screening.

7.2 Hierarchical classification strategy for EGFR phenotype extraction

From the good results accomplished in Chapter 2, we continued to improve the phenotype identification process so as to get an even higher classification score.

We had noticed that the way to quantify the prominent features from a segmented image is a crucial step in the identification process. In the data analysis part, the classification strategy is evenly important to make full use of all measurements. Our improvements are reported in Chapter 3. We have designed a scheme by employing a hierarchical classification strategy and adding wavelet-based texture measurements to further improve the recognition of phenotypic episodes of EGFR endocytosis. The hierarchical classification strategy is very capable in dealing with complex classification problems. For the case study in Chpater 3, we construct the classification process in a hierarchical way by separating three classes classification into two steps. Meanwhile, we can select prominent features for each step. As a result, this strategy makes full use of related features and improves the performance of the classifier. The motivation for us to use the wavelet-based texture measurements is to include extra prominent features in our set of observations and to lessen the impact of fluorescent intensity variation. After integrating all merits, the phenotype identification process shows a remarkable improvement and has been successfully used to find new regulators in the EGFR endocytosis process.

7.3 Analytical evaluation of point cloud surface reconstruction methods

Feature quantification can not only be used for classifier training, but can also be used for analytical evaluation. For 3D feature analysis we are interested in surface description for geometrical models derived from images. As far as we have concluded from the literature, the straightforward way to evaluate surface reconstruction methods is by convincing through visual inspection. Analytical evaluation seems to be missing for this purpose. In Chapter 4, we utilize 3D surface descriptors including surface distance, surface area and surface curvature to evaluate four representative surface reconstruction methods from a point cloud. Meanwhile, we validate 3D model through ground truth models. To that end we have introduced three analytical shapes: the unit sphere, the ellipsoid and the

ovoid to provide the ground truth values. From the results we have concluded that Poisson reconstruction method has the most stable performance in shape preservation and noise repression. We intend to utilize the results on biological 3D models to improve the quality of surface representation; because the former representation was not considered sufficiently for analysis.

7.4 3D model representation for phenotype analysis

For a 3D stack of images, model is represented in a geometrical model. We have optimized the 3D reconstruction method based on the knowledge derived from Chapter 4. First, we have reconstructed a 3D model from the stack of 2D contour images. Subsequently, we have been able to extract important features from the surface model. In Chapter 5, we have introduced such a system for 3D representation and analysis from a stack of images. We have augmented the model by resampling using a contour interpolation method. Our workflow has been validated with real image stack data. In this manner a stack of images is successfully converted into a uniformly distributed point cloud. We have applied the conclusion derived from Chapter 4 and have utilized the Poisson reconstruction to construct the surface model from the point cloud. We have chosen different shape features to adapt to different biology studies. We have used the sphericity shape factor in a study on development of zebrafish. This feature is a relative and compact descriptor. This case study validated the capability of our 3D representation and analysis system.

7.5 Nature inspired phenotype analysis with 3D model representation

In Chapter 6, we have intentionally been dealing with a much more complex 3D shape: the developing rodent mammary gland. The mammary gland is a branched structure and we have used centerline extraction method to establish the

topology of the branch structure and calculate the corresponding measurements from this simplified topological structure. Further we have introduced a ground truth model by using the L-system formation. We construct an L-system model for mouse mammary gland by which we can simulate the different results under different conditions. In this Chapter, we have validated the robustness of the 3D representation method and have demonstrated the potential of L-system as a ground truth model where no other is available but a good formalism can provide the necessary insight. The L-system resulted to show the effect of endocrine disruption.

7.6 Conclusion and future work

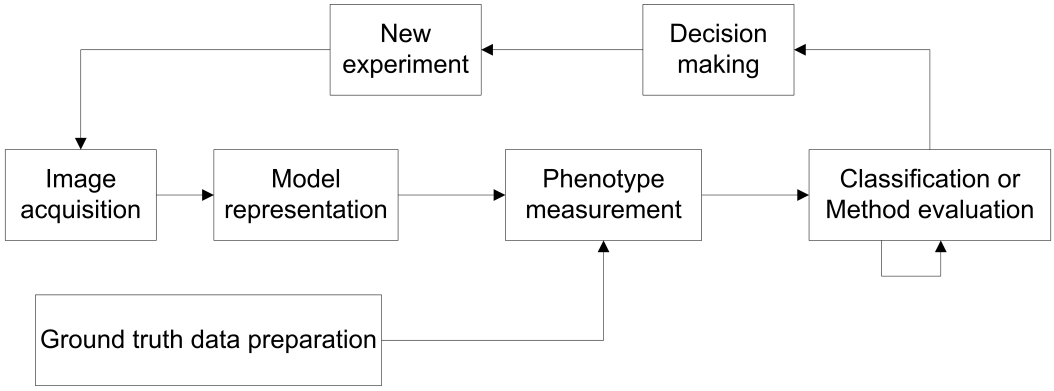

Figure 7.1. General workflow.

This thesis presents a number of studies in biological image dataset analysis both in 2D and 3D space. The general workflow is shown in Figure 7.1. In this thesis the recurring themes are pivotal to image analysis of large volumes of data. The studies are grouped on the themes of feature selection and ground truth in datasets. These studies enlighten us the general routing in coping with different datasets in N-Dimensional space and extracting related and interesting information from the original image dataset. They also have lead us to explore the specific ways for each image dataset how to pass this route. With all these experiences, we summarize the important points. First is the phenotype measurement. The measurements should meet the biological description and should be prominent to distinguish between different categories. We do not focus on the quality of

features but the quality of a few features. Therefore, the feature sets and feature extraction methods differ with different biological dataset. We should always be conscious to find the measureable and objective features during our future work. Ground truth data (training data) preparation is crucial for supervised classifier training and method evaluation. The amount of the ground truth data (training data) should be big enough and it should be relative to the complexity of the "true" function. According to our experience, for each category or each parameter, 50 ground truth samples is the lower bound for the classification validation and method evaluation. The reality is that ground truth data are always sparse. Therefore the question to set a proper proportion from limited training data should be a part of future work. 3D image stack representation and analysis system could also be improved in many aspects such as reconstruction method, contour interpolation method as well as centerline extraction method. Here we have presented a good start but this can be further elaborated in our future work.

Bibliography

C. B. Akgül, B. Sankur, Y. Yemez, and F. Schmitt. 3d model retrieval using probability density-based shape descriptors. *IEEE Trans. Pattern Anal. Mach. Intell.*, 31(6):1117–1133, June 2009. ISSN 0162-8828. doi: 10.1109/TPAMI.2009.25. URL `http://dx.doi.org/10.1109/TPAMI.2009.25`.

S. Aksoy and R. M. Haralick. Feature normalization and likelihood-based similarity measures for image retrieval. *Pattern Recognition Letters*, 22(5):563–582, April 2001. ISSN 01678655. doi: 10.1016/S0167-8655(00)00112-4.

N. Amenta, M. Bern, and M. Kamvysselis. A new voronoi-based surface reconstruction algorithm. In *Proceedings of the 25th annual conference on Computer graphics and interactive techniques*, SIGGRAPH '98, pages 415–421, New York, NY, USA, 1998. ACM. ISBN 0-89791-999-8. doi: 10.1145/280814.280947. URL `http://doi.acm.org/10.1145/280814.280947`.

N. Amenta, S. Choi, T. K. Dey, and N. Leekha. A simple algorithm for homeomorphic surface reconstruction. In *Proceedings of the sixteenth annual symposium on Computational geometry*, SCG '00, pages 213–222, New York, NY, USA, 2000. ACM. ISBN 1-58113-224-7. doi: 10.1145/336154.336207. URL `http://doi.acm.org/10.1145/336154.336207`.

N. Amenta, S. Choi, and R. K. Kolluri. The power crust. In *Proceedings of the sixth ACM symposium on Solid modeling and applications*, pages 249–266, 2001.

G. A. Ascoli. Progress and perspectives in computational neuroanatomy. *The Anatomical Record*, 257(6):195–207, 1999. ISSN 1097-0185. doi: 10.1002/(SICI)1097-0185(19991215)257:6⟨195::AID-AR5⟩3.0.CO;2-H. URL `http://dx.doi.org/10.1002/(SICI)1097-0185(19991215)257:6<195::AID-AR5>3.0.CO;2-H`.

G. A. Ascoli and J. L. Krichmar. L-neuron: A modeling tool for the efficient generation and

parsimonious description of dendritic morphology. *Neurocomputing*, 3233(0):1003 – 1011, 2000. ISSN 0925-2312.

A. J. Baddeley, H. J. G. Gundersen, and L. M. Cruz-Orive. Estimation of surface area from vertical sections. *Journal of Microscopy*, 142(3):259–276, 1986. ISSN 1365-2818. doi: 10.1111/j.1365-2818.1986.tb04282.x. URL `http://dx.doi.org/10.1111/j.1365-2818.1986.tb04282.x`.

G. Barequet, M. T. Goodrich, A. Levi-Steiner, and D. Steiner. Straight-skeleton based contour interpolation. In *Proceedings of the fourteenth annual ACM-SIAM symposium on Discrete algorithms*, SODA '03, pages 119–127, Philadelphia, PA, USA, 2003. Society for Industrial and Applied Mathematics. ISBN 0-89871-538-5. URL `http://portal.acm.org/citation.cfm?id=644108.644129`.

W. Barrett, E. Mortensen, and D. Taylor. An Image Space Algorithm for Morphological Contour Interpolation. In *In Proc. Graphics Interface*, pages 16–24, 1994.

A. K. Bera and C. M. Jarque. Efficient tests for normality, homoscedasticity and serial independence of regression residuals: Monte carlo evidence. *Economics Letters*, 7(4):313 – 318, 1981. ISSN 0165-1765. doi: 10.1016/0165-1765(81)90035-5.

J. Bernsen. Dynamic thresholding of gray-level images. In *International Conference on Pattern Recognition*, 1986.

J. D. Boissonnat. Geometric structures for three-dimensional shape representation. *ACM Trans. Graph.*, 3(4):266–286, October 1984. ISSN 0730-0301. doi: 10.1145/357346.357349. URL `http://doi.acm.org/10.1145/357346.357349`.

J. D. Boissonnat. Shape reconstruction from planar cross sections. *Comput. Vision Graph. Image Process.*, 44(1):1–29, August 1988. ISSN 0734-189X. doi: 10.1016/S0734-189X(88)80028-8. URL `http://dx.doi.org/10.1016/S0734-189X(88)80028-8`.

J. D. Boissonnat and B. Geiger. Three-dimensional reconstruction of complex shapes based on the delaunay triangulation, 1993.

P. J. Boon, N. Eminovic, A. De Vos, B. Buitendijk, E. J. Van Raaij, M. J. Den Broeder, W. J. Hage, and F.J. Verbeck. A virtual lab-notebook for multidimensional microscope images. In *Information Visualization, 2000. Proceedings. IEEE International Conference on*, pages 187–191, 2000. doi: 10.1109/IV.2000.859754.

F. Boudon, C. Pradal, T. Cokelaer, P. Prusinkiewicz, and C. Godin.

P. Bountris, E. Farantatos, and N. Apostolou. Advanced Image Analysis Tools Development for the Early Stage Bronchial Cancer Detection.

I. Braude, J. Marker, K. Museth, J. Nissanov, and D. Breen. Contour-based surface reconstruction using MPU implicit models. *GRAPHICAL MODELS*, 69:2007.

I. Braude, J. Marker, K. Museth, J. Nissanov, and D. Breen. Contour-based surface reconstruction using implicit curve fitting, and distance field filtering and interpolation. In *In Proc. International Workshop on Volume Graphics*, pages 95–102, 2006.

L. Cao and F. J. Verbeek. Evaluation of algorithms for point cloud surface reconstruction through the analysis of shape parameters. pages 82900G–82900G–10, 2012. doi: 10.1117/12.906718.

L. Cao and F. J. Verbeek. Analytical evaluation of algorithms for point cloud surface reconstruction using shape features. *Journal of Electronic Imaging*, 22(4):043008–043008, 2013. doi: 10.1117/1.JEI.22.4.043008. URL `http://dx.doi.org/10.1117/1.JEI.22.4.043008`.

L. Cao, K. Yan, L. Winkel, M. De Graauw, and F. J. Verbeek. Pattern recognition in high-content cytomics screens for target discovery: case studies in endocytosis. pages 330–342, 2011. URL `http://dl.acm.org/citation.cfm?id=2075619.2075657`.

R. Cardenes, H. Bogunovic, and A. F. Frangi. Fast 3D centerline computation for tubular structures by front collapsing and fast marching. In *Proceedings of the International Conference on Image Processing, ICIP 2010, September 26-29, Hong Kong, China*, pages 4109–4112. IEEE, 2010. ISBN 978-1-4244-7994-8. doi: http://dx.doi.org/10.1109/ICIP.2010.5651609.

J. C. Carr, R. K. Beatson, B. C. McCallum, W. R. Fright, T. J. McLennan, and T. J. Mitchell. Smooth surface reconstruction from noisy range data. In *Proceedings of the 1st international conference on Computer graphics and interactive techniques in Australasia and South East Asia*, GRAPHITE '03, pages 119—-127, New York, NY, USA, 2003. ACM. ISBN 1-58113-578-5. doi: http://doi.acm.org/10.1145/604471.604495. URL `http://doi.acm.org/10.1145/604471.604495`.

T. Chen and Z. Q. Shen. An adaptive image segmentation method using region growing. In *Computer Engineering and Technology (ICCET), 2010 2nd International Conference on*, volume 7, pages V7–78–V7–80, April 2010.

P. Cignoni. Meshlab. June 2010.

C. Collinet, M. Stter, C. R. Bradshaw, N. Samusik, J. C. Rink, D. Kenski, B. Habermann, F. Buchholz, R. Henschel, M. S. Mueller, W.E. Nagel, E. Fava, Y. Kalaidzidis, and M. Zerial. Systems survey of endocytosis by multiparametric image analysis. *Nature*, (7286):243249, 2010. doi: 10.1038/nature08779.

J. Conway and N. Sloane. Sphere packings, lattices, and groups. 1999.

C. Cortes and V. Vapnik. Support-Vector Networks. *Mach. Learn.*, 20(3):273–297, September 1995. ISSN 0885-6125. doi: 10.1023/A:1022627411411. URL `http://dx.doi.org/10.1023/A:1022627411411`.

P. Cowin and J. Wysolmerski. Molecular mechanisms guiding embryonic mammary gland development. *Cold Spring Harb Perspect Biol*, 2(6):a003251, 2010. ISSN 1943-0264. URL `http://www.biomedsearch.com/nih/Molecular-Mechanisms-Guiding-Embryonic-Mammary/20484386.html`.

N. Cristianini and J. Shawe-Taylor. In *An introduction to support Vector Machines: and other kernel-based learning methods*. Cambridge University Press, New York, NY, USA, 2000. ISBN 0521780195.

B. Curless and M. Levoy. A volumetric method for building complex models from range images. In *Proceedings of the 23rd annual conference on Computer graphics and interactive techniques*, SIGGRAPH '96, pages 303–312, New York, NY, USA, 1996. ACM. ISBN 0-89791-746-4. doi: http://doi.acm.org/10.1145/237170.237269. URL `http://doi.acm.org/10.1145/237170.237269`.

L. Damiano, S. L. Dévédec, P. D. Stefano, D. Repetto, R. Lalai, H. Truong, J. L. Xiong, E. H. Danen, K. Yan, and F. J. Verbeek. p140cap suppresses the invasive properties of highly metastatic mtln3-egfr cells via impaired cortactin phosphorylation. *Oncogene*, (5):624633, 2011. doi: 10.1038/onc.2011.257.

M. N. Davies, A. Secker, A. A. Freitas, M. Mendao, J. Timmis, and D. R. Flower. On the hierarchical classification of g protein-coupled receptors. *Bioinformatics (Oxford, England)*, 23(23):3113–8, December 2007. ISSN 1367-4811. doi: 10.1093/bioinformatics/btm506.

M. de Graauw, L. Cao, L. Winkel, M. H. A. M. van Miltenburg, S. E. Le Dévédec, M. Klop, K. Yan, C. Pont, V. M. Rogkoti, and A. Tijsma. Annexin a2 depletion delays egfr endo-

cytic trafficking via cofilin activation and enhances egfr signaling and metastasis formation. *Oncogene*, (20):26102619, 2013. doi: 10.1038/onc.2013.219.

L. Devroye, L. Györfi, and G. Lugosi. *A Probabilistic Theory of Pattern Recognition*, volume 31 of *Stochastic Modelling and Applied Probability*. Springer, corrected edition, April 1996. ISBN 0387946187.

T. K. Dey and S. Goswami. Tight cocone: a water-tight surface reconstructor. In *Proceedings of the eighth ACM symposium on Solid modeling and applications*, SM '03, pages 127–134, New York, NY, USA, 2003. ACM. ISBN 1-58113-706-0. doi: http://doi.acm.org/10.1145/781606.781627. URL `http://doi.acm.org/10.1145/781606.781627`.

T. K. Dey and S. Goswami. Provable surface reconstruction from noisy samples. In *Proceedings of the twentieth annual symposium on Computational geometry*, SCG '04, pages 330–339, New York, NY, USA, 2004. ACM. ISBN 1-58113-885-7. doi: http://doi.acm.org/10.1145/997817.997867. URL `http://doi.acm.org/10.1145/997817.997867`.

T. K. Dey and J. Sun. Defining and computing curve-skeletons with medial geodesic function. In *Proceedings of the Fourth Eurographics Symposium on Geometry Processing*, SGP '06, pages 143–152, Aire-la-Ville, Switzerland, Switzerland, 2006. Eurographics Association. ISBN 3-905673-36-3. URL `http://dl.acm.org/citation.cfm?id=1281957.1281975`.

T. K. Dey, J. Giesen, and J. Hudson. Delaunay based shape reconstruction from large data. In *Proceedings of the IEEE 2001 symposium on parallel and large-data visualization and graphics*, pages 19–27, 2001.

J. R. Ding, A. Bashashati, A. Roth, A. Oloumi, K. Tse, T. Zeng, G. Haffari, M. Hirst, M. A. Marra, A. Condon, S. Aparicio, and S. P. Shah. Feature based classifiers for somatic mutation detection in tumour-normal paired sequencing data. *Bioinformatics*, 2011. doi: 10.1093/bioinformatics/btr629.

R.P.W. Duin, P. Juszczak, P. Paclik, E. Pekalska, D. de Ridder, D.M.J. Tax, and S. Verzakov. Pr-tools4.1, a matlab toolbox for pattern recognition. 2007.

D. Eberly. Distance from a point to an ellipsoid. October 2011.

A. B. Ekoule, F. C. Peyrin, and C. L. Odet. A triangulation algorithm from arbitrary shaped multiple planar contours. *ACM Trans. Graph.*, 10(2):182–199, April 1991. ISSN 0730-0301. doi: http://doi.acm.org/10.1145/108360.108363. URL `http://doi.acm.org/10.`

1145/108360.108363.

F. N. Fritsch and R. E. Carlson. Monotone Piecewise Cubic Interpolation. *SIAM Journal on Numerical Analysis*, 17(2):238–246, 1980. URL http://scitation.aip.org/getabs/servlet/GetabsServlet?prog=normal&id=SJNAAM000017000002000238000001&idtype=cvips&gifs=yes.

K. Fukunaga. *Introduction to Statistical Pattern Recognition, Second Edition (Computer Science & Scientific Computing)*. Academic Press, 2 edition, October 1990. ISBN 0122698517.

T. Galvez, M. Teruel, W. Heo, J. Jones, M. Kim, J. Liou, J. Myers, and T. Meyer. sirna screen of the human signaling proteome identifies the ptdins(3,4,5)p3-mtor signaling pathway as a primary regulator of transferrin uptake. *Genome Biology*, 8(7):R142, 2007. ISSN 1465-6906. doi: 10.1186/gb-2007-8-7-r142.

S. Ganapathy and T. G. Dennehy. A new general triangulation method for planar contours. In *Proceedings of the 9th annual conference on Computer graphics and interactive techniques*, SIGGRAPH '82, pages 69–75, New York, NY, USA, 1982. ACM. ISBN 0-89791-076-1. doi: http://doi.acm.org/10.1145/800064.801264. URL http://doi.acm.org/10.1145/800064.801264.

N. Geldner and G. Jürgens. Endocytosis in signalling and development. *Current Opinion in Plant Biology*, 9(6):589–594, 2006. ISSN 1369-5266. doi: 10.1016/j.pbi.2006.09.011. URL http://www.sciencedirect.com/science/article/pii/S136952660600152X.

R. N. Ghosh, R. DeBiasio, C. C. Hudson, E. R. Ramer, C. L. Cowan, and R. H. Oakley. Quantitative cell-based high-content screening for vasopressin receptor agonists using transfluor technology. *Journal of biomolecular screening : the official journal of the Society for Biomolecular Screening*, 10(5):476–84, August 2005. ISSN 1087-0571. doi: 10.1177/1087057105274896.

S. Goldoni, R. A. Iozzo, P. Kay, S. Campbell, A. McQuillan, C. Agnew, J. X. Zhu, D. R. Keene, Reed C. C., and R. V. Iozzo. A soluble ectodomain of lrig1 inhibits cancer cell growth by attenuating basal and ligand-dependent egfr activity. *Oncogene*, 26(3):368381, 2006.

R. C. Gonzalez and R. E. Woods. *Digital Image Processing*. Addison-Wesley Longman Publishing Co., Inc., Boston, MA, USA, 2nd edition, 2001. ISBN 0201180758.

A. Gouaillard, K. Mosaliganti, A. Gelas, L. Souhait, N. Obholzer, and S. Megason. Streaming

level set algorithm for 3d segmentation of confocal microscopy images. In *Engineering in Medicine and Biology Society, 2009. EMBC 2009. Annual International Conference of the IEEE*, pages 3621–3624, Sept 2009. doi: 10.1109/IEMBS.2009.5333522.

J. B. S. Haldane. The Precision of Observed Values of Small Frequencies. *Biometrika*, 35(3/4): pp. 297–300, 1948. ISSN 00063444. URL `http://www.jstor.org/stable/2332350`.

A. O. Hatch, S. Kajarekar, and A. Stolcke. Within-class Covariance Normalization for SVM-based Speaker Recognition. page 14711474, 2006.

Y. He and H. Qin. Surface reconstruction with triangular b-splines. In *Proceedings of the Geometric Modeling and Processing 2004*, GMP '04, pages 279–287, Washington, DC, USA, 2004. IEEE Computer Society. ISBN 0-7695-2078-2. URL `http://dl.acm.org/citation.cfm?id=977398.977793`.

A. Henderson. *The {ParaView} Guide: A Parallel Visualization Application*. Kitware, November 2004.

G. T. Herman, J. S. Zheng, and C. A. Bucholtz. Shape-Based Interpolation. *IEEE Comput. Graph. Appl.*, 12(3):69–79, May 1992. ISSN 0272-1716. doi: 10.1109/38.135915. URL `http://dx.doi.org/10.1109/38.135915`.

H. Hoppe, T. DeRose, T. Duchamp, J. McDonald, and W. Stuetzle. Surface reconstruction from unorganized points. *SIGGRAPH Comput. Graph.*, 26(2):71–78, 1992. ISSN 0097-8930. doi: http://doi.acm.org/10.1145/142920.134011. URL `http://doi.acm.org/10.1145/142920.134011`.

C. W. Hsu, C. C. Chang, and C.J. Lin. A practical guide to support vector classification. 1(1): 1–16, 2010.

M. K. Hu. Visual pattern recognition by moment invariants. *Information Theory, IRE Transactions on*, 8(2):179–187, 1962. ISSN 0096-1000. doi: 10.1109/TIT.1962.1057692.

S. M. Hu and J. Wallner. A second order algorithm for orthogonal projection onto curves and surfaces. *Computer Aided Geometric Design*, 22(3):251 – 260, 2005. ISSN 0167-8396. doi: 10.1016/j.cagd.2004.12.001.

P. A. Jacobsen, D. Becker, D. P. Govier, S. G. Krantz, and A. Kane. Ellipsoid analysis of calvarial shape., September 2009. ISSN 1055-6656.

A. K. Jain, R. P. W. Duin, and J. C. Mao. Statistical pattern recognition: A review. *IEEE*

TRANSACTIONS ON PATTERN ANALYSIS AND MACHINE INTELLIGENCE, 22(1): 4–37, 2000.

H. Jelinek, A. Karperien, D. Cornforth, R. M. Cesar Junior, and Leandro J. J. G. Micromod - an l-systems approach to neuron modelling. In *National University*, pages 156–163, 2002.

H. F. Jelinek, R. M. Cesar, J. J. G. Leandro, and I. Spence. Automated morphometric analysis of the cat retinal alpha/y, beta/x and delta ganglion cells using wavelet statistical moment and clustering algorithms. *J Integr Neurosci*, 3 (4):415–32, 2004. ISSN 0219-6352. URL `http://www.biomedsearch.com/nih/Automated-morphometric-analysis-cat-retinal/15657977.html`.

X. Jiang, F. Huang, A. Marusyk, and A. Sorkin. Grb2 regulates internalization of egf receptors through clathrin-coated pits. 3(14):858–870, 2003.

W. Johannsen. The genotype conception of heredity. *The American Naturalist*, 45(531):pp. 129–159, 1911. ISSN 00030147. URL `http://www.jstor.org/stable/2455747`.

M. W. Jones and M. Chen. A New Approach to the Construction of Surfaces from Contour Data. *Comput. Graph. Forum*, 13(3):75–84, 1994.

D.l Kaba, C. Wang, Y. M. Li, A. Salazar-Gonzalez, X. H. Liu, and A. Serag. Retinal blood vessels extraction using probabilistic modelling. *Health Information Science and Systems*, 2 (1):2, 2014. ISSN 2047-2501. doi: 10.1186/2047-2501-2-2. URL `http://www.hissjournal.com/content/2/1/2`.

P. Kalman, T. Juerg, A. H. Eric, and S. Milan. Quantitative analysis of pulmonary airway tree structures. *Computers in Biology and Medicine*, 36(9):974–996, 2006.

D. G. Kang, D. C. Suh, and J. B. Ra. Three-dimensional blood vessel quantification via centerline deformation. *Medical Imaging, IEEE Transactions on*, 28(3):405–414, March 2009. ISSN 0278-0062. doi: 10.1109/TMI.2008.2004651.

T. Kanungo, D. M. Mount, N. S. Netanyahu, C. D. Piatko, R. Silverman, and A. Y. Wu. An efficient k-means clustering algorithm: Analysis and implementation. *IEEE Transactions on Pattern Analysis and Machine Intelligence*, 24:881–892, 2002.

M. Kass, A. Witkin, and D. Terzopoulos. Snakes: Active contour models. *International Journal of Computer Vision*, 1(4):321–331, 1988. ISSN 0920-5691. doi: 10.1007/BF00133570. URL `http://dx.doi.org/10.1007/BF00133570`.

M. Kazhdan. Reconstruction of solid models from oriented point sets. In *Proceedings of the third Eurographics symposium on Geometry processing*, SGP '05, Aire-la-Ville, Switzerland, Switzerland, 2005. Eurographics Association. ISBN 3-905673-24-X. URL `http://dl.acm.org/citation.cfm?id=1281920.1281931`.

M. Kazhdan, M. Bolitho, and H. Hoppe. Poisson surface reconstruction. In *Proceedings of the fourth Eurographics symposium on Geometry processing*, SGP '06, pages 61–70, Aire-la-Ville, Switzerland, Switzerland, 2006a. Eurographics Association. ISBN 3-905673-36-3. URL `http://portal.acm.org/citation.cfm?id=1281957.1281965`.

M. Kazhdan, M. Bolitho, and H. Hoppe. Poisson surface reconstruction. In *SGP '06: Proceedings of the fourth Eurographics symposium on Geometry processing*, pages 61–70, Aire-la-Ville, Switzerland, Switzerland, 2006b. Eurographics Association. ISBN 30905673-36-3. URL `http://portal.acm.org/citation.cfm?id=1281957.1281965`.

E. Keppel. Approximating complex surfaces by triangulation of contour lines. *IBM J. Res. Dev.*, 19(1):2–11, January 1975. ISSN 0018-8646. doi: 10.1147/rd.191.0002. URL `http://dx.doi.org/10.1147/rd.191.0002`.

M. Kirchner, W. Timm, F. Peying, P. Wangemann, and H. Steen. Non-linear classification for on-the-fly fractional mass filtering and targeted precursor fragmentation in mass spectrometry experiments. *Bioinformatics*, 26(6):791 – 797, 2010. ISSN 13674803.

R. Klein, A. Schilling, and W. Straer. Reconstruction and simplification of surfaces from contours. *Graphical Models*, 62(6):429 – 443, 2000. ISSN 1524-0703. doi: 10.1006/gmod.2000.0530.

R. Kolluri, J. R. Shewchuk, and J. F. O'Brien. Spectral surface reconstruction from noisy point clouds. In *Proceedings of the 2004 Eurographics/ACM SIGGRAPH symposium on Geometry processing*, SGP '04, pages 11–21, New York, NY, USA, 2004. ACM. ISBN 3-905673-13-4. doi: http://doi.acm.org/10.1145/1057432.1057434. URL `http://doi.acm.org/10.1145/1057432.1057434`.

S. Kumar, J. Ghosh, and M. M. Crawford. Hierarchical Fusion of Multiple Classifiers for Hyperspectral Data Analysis. *Pattern Analysis & Applications*, 5(2):210–220, 2002. doi: 10.1007/s100440200019. URL `http://dx.doi.org/10.1007/s100440200019`.

A. H. Land and A. G. Doig. An Automatic Method for Solving Discrete Programming Problems.

Econometrica, 28:497–520, 1960a.

A. H. Land and A. G. Doig. An Automatic Method of Solving Discrete Programming Problems. *Econometrica*, 28(3):497–520, 1960b.

S. E. Le Dévédec, K. Yan, H. Bont, V. Ghotra, H. Truong, E. H. Danen, F. J. Verbeek, and B. van de Water. Systems microscopy approaches to understand cancer cell migration and metastasis. *Cellular and Molecular Life Sciences*, 67(19):3219–3240, 2010. ISSN 1420-682X. doi: 10.1007/s00018-010-0419-2.

P. C. Lee, C. C. Chuang, A. S. Chiang, and Y. T. Ching. High-throughput computer method for 3d neuronal structure reconstruction from the image stack of the drosophila brain and its applications. *PLoS Computational Biology*, 8(9), 2012.

T. C. Lee, R. L. Kashyap, and C. N. Chu. Building Skeleton Models via 3-D Medial Surface Axis Thinning Algorithms. *CVGIP: Graphical Models and Image Processing*, 56(6):462–478, 1994. ISSN 1049-9652. doi: 10.1006/cgip.1994.1042. URL `http://www.sciencedirect.com/science/article/pii/S104996528471042X`.

A. Lehmussola, P. Ruusuvuori, and O. Yli-Harja. Evaluating the performance of microarray segmentation algorithms. *Bioinformatics*, 22(23):2910–2917, 2006.

D. Leonard, A. Hayakawa, D. Lawe, D. Lambright, K. D. Bellve, C. Standley, L. M. Lifshitz, K. E. Fogarty, and S. Corvera. Sorting of egf and transferrin at the plasma membrane and by cargo-specific signaling to eea1-enriched endosomes. *Journal of cell science*, 121(Pt 20): 3445–58, October 2008. ISSN 0021-9533. doi: 10.1242/jcs.031484.

C. K. Leung and F. K. Lam. Image segmentation using maximum entropy method. In *Speech, Image Processing and Neural Networks, 1994. Proceedings, ISSIPNN '94., 1994 International Symposium on*, pages 29–32 vol.1, Apr 1994. doi: 10.1109/SIPNN.1994.344973.

D. Levin. Algorithms for approximation. chapter Multidimen, pages 421–431. Clarendon Press, New York, NY, USA, 1987. ISBN 0-19-853612-7. URL `http://dl.acm.org/citation.cfm?id=48424.48448`.

H. Li, C. Y. Ung, X. H. Ma, B. W. Li, B. C. Low, Z. W. Cao, and Y. Z. Chen. Simulation of crosstalk between small gtpase rhoa and egfr-erk signaling pathway via mekk1. *Bioinformatics*, 25(3):358–364, February 2009. ISSN 1367-4803. doi: 10.1093/bioinformatics/btn635. URL `http://dx.doi.org/10.1093/bioinformatics/btn635`.

H. W. Lilliefors. On the Kolmogorov-Smirnov test for the exponential distribution with mean unknown. *Journal of the American Statistical Association*, 64(325):387–389, 1969.

J. Lindblad. Surface area estimation of digitized 3d objects using weighted local configurations. *Image Vision Comput.*, 23(2):111–122, February 2005. ISSN 0262-8856. doi: 10.1016/j.imavis.2004.06.012. URL `http://dx.doi.org/10.1016/j.imavis.2004.06.012`.

A. Lindenmayer. Mathematical models for cellular interactions in development i. filaments with one-sided inputs. *Journal of Theoretical Biology*, 18(3):280 – 299, 1968. ISSN 0022-5193.

F. H. Long, J. L. Zhou, and H. C. Peng. Visualization and analysis of 3D microscopic images. *PLoS computational biology*, 8(6):e1002519, January 2012. ISSN 1553-7358. doi: 10.1371/journal.pcbi.1002519. URL `http://www.pubmedcentral.nih.gov/articlerender.fcgi?artid=3375219&tool=pmcentrez&rendertype=abstract`.

E. Magid, O. Soldea, and E. Rivlin. A comparison of Gaussian and mean curvature estimation methods on triangular meshes of range image data. *Computer Vision and Image Understanding*, 107(3):139–159, September 2007. ISSN 10773142. doi: 10.1016/j.cviu.2006.09.007.

P. C. Mahalanobis. On the generalised distance in statistics. In *Proceedings National Institute of Science, India*, volume 2, pages 49–55, April 1936a. URL `http://ir.isical.ac.in/dspace/handle/1/1268`.

P. C. Mahalanobis. On the generalised distance in statistics. *Proceedings of the National Institute of Sciences of India*, 2:49–55, 1936b.

R. Maini and H. Aggarwal. A comprehensive review of image enhancement techniques. March 2010. URL `http://arxiv.org/abs/1003.4053`.

I. Manakos, T. Schneider, and U. Ammer. A comparison between the isodata and the recognition classification methods on basis of field data. *Poster at the XIXth ISPRS Congr.*, 2000.

K. R. Mandrup, H. K. L. Johansson, J. Boberg, A. S. Pedersen, M. S. Mortensen, J. S. Jϕrgensen, A. M. Vinggaard, and U. Hass. Mixtures of environmentally relevant endocrine disrupting chemicals affect mammary gland development in female and male rats. *Reproductive Toxicology*, 2014. ISSN 0890-6238.

F. J. Massey. The Kolmogorov-Smirnov test for goodness of fit. *Journal of the American Statistical Association*, 46(253):68–78, 1951a.

F. J. Massey. The {K}olmogorov-{S}mirnov Test for Goodness of Fit. *Journal of the Amer-*

ican Statistical Association, 46(253):68–78, 1951b. URL http://www.jstor.org/stable/2280095.

A. Materka. Discrete wavelet trnasform derived features for digital image texture analysis. (September):163–168, 2001.

B. Mederos, N. Amenta, L. Velho, and L. H. de Figueiredo. Surface reconstruction from noisy point clouds. In *Proceedings of the third Eurographics symposium on Geometry processing*, Aire-la-Ville, Switzerland, Switzerland, 2005. Eurographics Association. ISBN 3-905673-24-X. URL http://portal.acm.org/citation.cfm?id=1281920.1281929.

T. Mitchell. McGraw-Hill Education (ISE Editions), 1st edition, October 1997. ISBN 0071154671.

T. Mitchell. Generative and discriminative classifiers: Naive bayes and logistic regression. 2005.

J. C. Mullikin and P. W. Verbeek. Surface area estimation of digitized planes. *Bioimaging*, 1(1): 6–16, 1993. ISSN 1361-6374. doi: 10.1002/1361-6374(199303)1:1⟨6::AID-BIO3⟩3.0.CO;2-3. URL http://dx.doi.org/10.1002/1361-6374(199303)1:1<6::AID-BIO3>3.0.CO;2-3.

L. Muniz Feliciano, J. Van Grol, J. A. C. Portillo, L. Liew, B. Liu, C. R. Carlin, V. B. Carruthers, S. Matthews, and C. S. Subauste. Toxoplasma gondii-induced activation of egfr prevents autophagy protein-mediated killing of the parasite. *PLoS Pathog*, 9(12):e1003809, 12 2013.

A. H. Natalie, M. Glen, and W. R. Edwin. A new method for imaging and 3d reconstruction of mammalian cochlea by fluorescent confocal microscopy. *Brain Research*, 1000(12):200 – 210, 2004. ISSN 0006-8993. Brain Research Volume 1000.

S. Naz, H. Majeed, and H. Irshad. Image segmentation using fuzzy clustering: A survey. In *Emerging Technologies (ICET), 2010 6th International Conference on*, pages 181–186, Oct 2010.

A. F. Neuwald, C. J. Lanczycki, and A. Marchler-Bauer. Automated hierarchical classification of protein domain subfamilies based on functionally-divergent residue signatures. In *BMC bioinformatics*, volume 13, page 144. June 2012. ISBN 1471210513144. doi: 10.1186/1471-2105-13-144.

A. Ng, K. K. Brock, M. B. Sharpe, J. L. Moseley, T. Craig, and D. C. Hodgson. Individualized 3D reconstruction of normal tissue dose for patients with long-term follow-up: a step toward

understanding dose risk for late toxicity. *International journal of radiation oncology, biology, physics*, 84(4):e557–63, November 2012. ISSN 1879-355X. doi: 10.1016/j.ijrobp.2012.06.026. URL `http://www.ncbi.nlm.nih.gov/pubmed/22929861`.

W. Niblack. *An Introduction to Digital Image Processing*. Strandberg Publishing Company, Birkeroed, Denmark, Denmark, 1985. ISBN 87-872-0055-4.

Y. Nishimura, K. Yoshioka, O. Bernard, B. Bereczky, and K. Itoh. A role of LIM kinase 1/cofilin pathway in regulating endocytic trafficking of EGF receptor in human breast cancer cells. *Histochemistry and cell biology*, 126(5):627–38, November 2006. ISSN 0948-6143. doi: 10.1007/s00418-006-0198-x.

G. Nmeth, P. Kardos, and K. Palgyi. Topology preserving 3d thinning algorithms using four and eight subfields. 6111:316–325, 2010. doi: 10.1007/978-3-642-13772-3_32. URL `http://dx.doi.org/10.1007/978-3-642-13772-3_32`.

Y. Ohtake, A. Belyaev, M. Alexa, G. Turk, and H. P. Seidel. Multi-level partition of unity implicits. *ACM Trans. Graph.*, 22(3):463–470, 2003. ISSN 0730-0301. doi: http://doi.acm.org/10.1145/882262.882293. URL `http://doi.acm.org/10.1145/882262.882293`.

Oleg Okun. Feature normalization and selection for protein fold recognition. *Proc. of the 11th Finnish Artificial Intelligence Conference*, pages 207–221, 2004.

N. Otsu. A Threshold Selection Method from Gray-level Histograms. *IEEE Transactions on Systems, Man and Cybernetics*, 9(1):62–66, January 1979. ISSN 0018-9472. doi: 10.1109/tsmc.1979.4310076. URL `http://dx.doi.org/10.1109/tsmc.1979.4310076`.

S. Paulus, J. Dupuis, A. K. Mahlein, and H. Kuhlmann. Surface feature based classification of plant organs from 3d laserscanned point clouds for plant phenotyping. *BMC Bioinformatics*, 14(1):238, 2013. ISSN 1471-2105. doi: 10.1186/1471-2105-14-238. URL `http://www.biomedcentral.com/1471-2105/14/238`.

L. Pelkmans, E. Fava, H. Grabner, M. Hannus, B. Habermann, E. Krausz, and M. Zerial. Genome-wide analysis of human kinases in clathrin- and caveolae/raft-mediated endocytosis. *Nature*, 436(7047):78–86, July 2005. ISSN 0028-0836. doi: 10.1038/nature03571. URL `http://dx.doi.org/10.1038/nature03571`.

R. Pfeifle and H. P. Seidel. Fitting triangular b-splines to functional scattered data. *Computer Graphics Forum*, 15(1):15–23, 1996. ISSN 1467-8659. doi: 10.1111/1467-8659.1510015. URL

http://dx.doi.org/10.1111/1467-8659.1510015.

M. Piccinelli, A. Veneziani, D. A. Steinman, A. Remuzzi, and L. Antiga. A Framework for Geometric Analysis of Vascular Structures: Application to Cerebral Aneurysms. *IEEE Trans. Med. Imaging*, 28(8):1141–1155, 2009. doi: http://dx.doi.org/10.1109/TMI.2009.2021652.

H. Pottmann and S. Leopoldseder. A concept for parametric surface fitting which avoids the parametrization problem. *Computer Aided Geometric Design*, 20(6):343 – 362, 2003. ISSN 0167-8396. doi: 10.1016/S0167-8396(03)00078-5.

A. Pressley. *Elementary differential geometry.* Springer, London; New York, 2010. ISBN 9781848828902 184882890X.

P. Prusinkiewicz and A. Lindenmayer. *The Algorithmic Beauty of Plants.* Springer-Verlag New York, Inc., New York, NY, USA, 1990. ISBN 0-387-97297-8.

Y. Qin, G. Stokman, K. Yan, S. Ramaiahgari, F. J. Verbeek, M. de Graauw, B. van de Water, and L. S. Price. camp signalling protects proximal tubular epithelial cells from cisplatin-induced apoptosis via activation of epac. *British Journal of Pharmacology*, 165(4b):1137–1150, 2012a. ISSN 1476-5381. doi: 10.1111/j.1476-5381.2011.01594.x. URL http://dx.doi.org/10.1111/j.1476-5381.2011.01594.x.

Y. Qin, G. Stokman, K. Yan, S. Ramaiahgari, F. J. Verbeek, M. de Graauw, B. van de Water, and L. S. Price. camp signalling protects proximal tubular epithelial cells from cisplatin-induced apoptosis via activation of epac. *British journal of pharmacology*, 165(4b):1137–50, February 2012b. ISSN 1476-5381. doi: 10.1111/j.1476-5381.2011.01594.x.

L. Qu, F. H. Long, X. Liu, S. K. Kim, E. W. Myers, and H. C. Peng. Simultaneous recognition and segmentation of cells: application in c.elegans. *Bioinformatics*, 27(20):2895–2902, 2011.

Y. G. Qu, T. T. Wong, and P. A. Heng. Image segmentation using the level set method. In *Deformable Models*, Topics in Biomedical Engineering. International Book Series, pages 95–122. Springer New York, 2007. ISBN 978-0-387-31204-0. doi: 10.1007/978-0-387-68343-0_4. URL http://dx.doi.org/10.1007/978-0-387-68343-0_4.

J. Z. Rappoport and S. M. Simon. Endocytic trafficking of activated egfr is ap-2 dependent and occurs through preformed clathrin spots. *Journal of Cell Science*, 122(9):1301–305, 2009.

A. Ray, K. Shukla, L. Aggarwal, N. Sharma, S. Pradhan, and S. Sharma. Segmentation and classification of medical images using texture-primitive features: Application of bam-type

artificial neural network. *Journal of Medical Physics*, 33(3):119–126, 2008. doi: 10.4103/0971-6203.42763.

K. Roepstorff, L. Grovdal, M. Grandal, M. Lerdrup, and B. van Deurs. Endocytic downregulation of erbb receptors: mechanisms and relevance in cancer. *Histochemistry and cell biology*, 129(5):563–78, May 2008. ISSN 0948-6143. doi: 10.1007/s00418-008-0401-3.

G. Rozenberg and A. Salomaa. *Mathematical Theory of L Systems.* Academic Press, Inc., Orlando, FL, USA, 1980. ISBN 0125971400.

G. Rozenberg and A. Salomaa, editors. *The book of L.* Springer-Verlag New York, Inc., New York, NY, USA, 1986. ISBN 0-387-16022-1.

O. Rubel, G. H. Weber, M. Y. Huang, E. W. Bethel, M. D. Biggin, C. C. Fowlkes, C. L. Luengo Hendriks, S. V. E. Keranen, M. B. Eisen, D. W. Knowles, J. Malik, H. Hagen, and B. Hamann. Integrating data clustering and visualization for the analysis of 3D gene expression data. *IEEE/ACM transactions on computational biology and bioinformatics / IEEE, ACM*, 7(1):64–79, 2010. ISSN 1557-9964. doi: 10.1109/TCBB.2008.49. URL `http://www.ncbi.nlm.nih.gov/pubmed/20150669`.

P. T. Sander and S. W. Zucker. Inferring Surface Trace and Differential Structure from 3-D Images. *IEEE Trans. Pattern Anal. Mach. Intell.*, 12(9):833–854, September 1990. ISSN 0162-8828. doi: http://dx.doi.org/10.1109/34.57680. URL `http://dx.doi.org/10.1109/34.57680`.

P. SangitaB and S. R. Deshmukh. Use of Support Vector Machine, decision tree and Naive Bayesian techniques for wind speed classification. *Power and Energy Systems (ICPS), 2011 International Conference*, pages 1–8, 2011. ISSN 00063444. URL `http://www.jstor.org/stable/2332350`.

J. Serra. *Image Analysis and Mathematical Morphology.* Academic Press, Inc., Orlando, FL, USA, 1983. ISBN 0126372403.

A. Shadvar and A. Erfanian. Mutual information-based Fisher discriminant analysis for feature extraction and recognition with applications to medical diagnosis. *Conference proceedings : ... Annual International Conference of the IEEE Engineering in Medicine and Biology Society. IEEE Engineering in Medicine and Biology Society. Conference*, 2010:5811–4, January 2010. ISSN 1557-170X. doi: 10.1109/IEMBS.2010.5627461.

J. Sharpe, U. Ahlgren, P. Perry, B. Hill, A. Ross, J. Hecksher Srensen, R. Baldock, and D. Davidson. Optical projection tomography as a tool for 3d microscopy and gene expression studies. *Science*, 296(5567):541–545, 2002. doi: 10.1126/science.1068206.

C. N. Silla and A. A. Freitas. A survey of hierarchical classification across different application domains. *Data Min. Knowl. Discov.*, 22(1-2):31–72, 2011. ISSN 1384-5810. doi: 10.1007/s10618-010-0175-9. URL `http://dx.doi.org/10.1007/s10618-010-0175-9`.

S. D. Solvenus and N. Yamamoto. 3d displays of egg and apple. January 2011.

P. Somol, P. Pudil, and J. Kittler. Fast branch amp; bound algorithms for optimal feature selection. *Pattern Analysis and Machine Intelligence, IEEE Transactions on*, 26(7):900–912, July 2004. ISSN 0162-8828. doi: 10.1109/TPAMI.2004.28.

Y. Song, W. D. Cai, H. Huang, Y. Wang, D. Feng, and M. Chen. Region-based progressive localization of cell nuclei in microscopic images with data adaptive modeling. *BMC Bioinformatics*, 14(1):173, 2013. ISSN 1471-2105. doi: 10.1186/1471-2105-14-173. URL `http://www.biomedcentral.com/1471-2105/14/173`.

Y. W. Sun, D. M. Guo, Z. Y. Jia, and W. J. Liu. B-spline surface reconstruction and direct slicing from point clouds. *The International Journal of Advanced Manufacturing Technology*, 27(9-10):918–924, 2006. ISSN 0268-3768. doi: 10.1007/s00170-004-2281-6. URL `http://dx.doi.org/10.1007/s00170-004-2281-6`.

P. J. Tadrous. Subcellular microanatomy by 3d deconvolution brightfield microscopy: Method and analysis using human chromatin in the interphase nucleus. *Anat Res Int*, 2012:848707, 2012. ISSN 2090-2751.

A. Takeuchi, M. Shneier, T. H. Hong, T. Chang, C. Scrapper, and G. S. Cheok. Ground truth and benchmarks for performance evaluation, 2003.

G. Tarcic, S. K. Boguslavsky, J. Wakim, T. Kiuchi, A. Liu, F. Reinitz, D. Nathanson, T. Takahashi, P. S. Mischel, T. Ng, and Y. Yarden. An unbiased screen identifies dep-1 tumor suppressor as a phosphatase controlling egfr endocytosis. *Current Biology*, 19(21):1788–1798, 2009. doi: 10.1016/j.cub.2009.09.048.An.

A. Telea and A. Vilanova. A robust level-set algorithm for centerline extraction. In *Joint EUROGRAPHICS-IEEE TCVG Symposium on visualization*, 2003.

S. Tripathi, K. Kumar, B. K. Singh, and R. P. Singh. Image segmentation : A review. 1(4):

838–843, 2012.

N. N. Tsiaparas, S. Golemati, I. Andreadis, J. Stoitsis, I. Valavanis, and K. S. Nikita. Assessment of carotid atherosclerosis from b-mode ultrasound images using directional multiscale texture features. *Measurement Science and Technology*, 23(11):114004, 2012.

C. Y. Ung, H. Li, X. H. Ma, J. Jia, B. W. Li, B. C. Low, and Y. Z. Chen. Simulation of the regulation of egfr endocytosis and egfr-erk signaling by endophilin-mediated rhoa-egfr crosstalk. *FEBS Letters*, 582(18):2283–2290, 2011.

R. Van Uitert and I. Bitter. Subvoxel precise skeletons of volumetric data based on fast marching methods. *Medical Physics*, 34(2):627–638, 2007. doi: 10.1118/1.2409238. URL `http://link.aip.org/link/?MPH/34/627/1`.

Andrea Vedaldi, Haibin Ling, and Stefano Soatto. Knowing a good feature when you see it: Ground truth and methodology to evaluate local features for recognition. In R. Cipolla, S. Battiato, and G. M. Farinella, editors, *Computer Vision*, volume 285 of *Studies in Computational Intelligence*, pages 27–49. Springer Berlin Heidelberg, 2010. ISBN 978-3-642-12847-9. doi: 10.1007/978-3-642-12848-6_2.

F. J. Verbeek. Deformation correction using euclidean contour distance maps. In *Pattern Recognition, 1992. Vol.III. Conference C: Image, Speech and Signal Analysis, Proceedings., 11th IAPR International Conference on*, pages 347–351, Aug 1992.

F. J. Verbeek. Theory & practice of 3d reconstructions from serial sections. In *In Image Processing, A Practical Approach*, pages 153–195. Oxford: Oxford University Press, 1999a.

F. J. Verbeek. Theory and practice of 3d-reconstructions from serial sections. *Image Processing, A Practical Approach*, pages 153–195, 1999b.

F. J. Verbeek and P. J. Boon. High-resolution 3d reconstruction from serial sections: microscope instrumentation, software design, and its implementations, 2002.

F. J. Verbeek and D. P. Huijsmans. A graphical database for 3d reconstruction supporting (4) different geometrical representations. 465:117–144, 1998. doi: 10.1007/978-1-4615-5553-7_5.

F. J. Verbeek, M. M. de Groot, D. P. Huijsmans, W. H. Lamers, and I. T. Young. 3d base: A geometrical data base system for the analysis and visualisation of 3d-shapes obtained from parallel serial sections including three different geometrical representations. *Computerized Medical Imaging and Graphics*, 17(3):151–163, 1993. ISSN 0895-6111. Confocal Microscopy.

F. J. Verbeek, D. P. Huijsmans, R. J. A. M. Baeten, N. J. C. Schoutsen, and W. H. Lamers. Design and implementation of a database and program for 3d reconstruction from serial sections: A data-driven approach. *Microscopy Research and Technique*, 30(6):496–512, 1995. ISSN 1097-0029. doi: 10.1002/jemt.1070300607. URL `http://dx.doi.org/10.1002/jemt.1070300607`.

F. J. Verbeek, M. J. den Broeder, P. J. Boon, B. Buitendijk, E. Doerry, E. J. van Raaij, and D. Zivkovic. Standard 3d digital atlas of zebrafish embryonic development for projection of experimental data, 1999a. URL `http://dx.doi.org/10.1117/12.373465`.

F. J. Verbeek, K. A. Lawson, and J. B. Bard. Developmental bioinformatics: linking genetic data to virtual embryos. *The International journal of developmental biology*, 43(7):761–771, 1999b. ISSN 0214-6282.

L. Vincent and P. Soille. Watersheds in digital spaces: an efficient algorithm based on immersion simulations. *Pattern Analysis and Machine Intelligence, IEEE Transactions on*, 13(6):583–598, Jun 1991. ISSN 0162-8828. doi: 10.1109/34.87344.

H. Wadell. Volume, shape, and roundness of quartz particles. *The Journal of Geology*, 43(3): 250–280, 1935.

A. R. Webb and K. D. Copsey. *Ensemble Methods*. John Wiley and Sons, Ltd, 2011. ISBN 9781119952954. doi: 10.1002/9781119952954.ch8.

N. Wiener. *Extrapolation, Interpolation, and Smoothing of Stationary Time Series*. The MIT Press, 1964. ISBN 0262730057.

B. Willis, J. N. Turner, D. N. Collins, B. Roysam, and T. J. Holmes. Developments in three-dimensional stereo brightfield microscopy. *Microscopy Research and Technique*, 24(5):437–451, 1993. ISSN 1097-0029. doi: 10.1002/jemt.1070240509. URL `http://dx.doi.org/10.1002/jemt.1070240509`.

I. H. Witten and E. Frank. *Data Mining: Practical Machine Learning Tools and Techniques, Second Edition (Morgan Kaufmann Series in Data Management Systems)*. Morgan Kaufmann Publishers Inc., San Francisco, CA, USA, 2005. ISBN 0120884070.

W. J. Xie, R. P. Thompson, and R. Perucchio. A topology-preserving parallel 3D thinning algorithm for extracting the curve skeleton. *Pattern Recognition*, 36(7):1529–1544, 2003. ISSN 0031-3203. doi: 10.1016/S0031-3203(02)00348-5. URL `http://www.sciencedirect.`

com/science/article/pii/S0031320302003485.

K. Yan and F. J. Verbeek. Segmentation for high-throughput image analysis: Watershed masked clustering. In *ISoLA (2)*, volume 7610 of *Lecture Notes in Computer Science*, pages 25–41. Springer, 2012a.

K. Yan and F. J. Verbeek. Segmentation for high-throughput image analysis: Watershed masked clustering. *Leveraging Applications of Formal Methods, Verification and Validation. Applications and Case Studies*, 7610:25–41, 2012b. doi: 10.1007/978-3-642-34032-1_4.

K Yan, S. Le Dévédec, B. van de Water, and F. J. Verbeek. Cell tracking and data analysis of in vitro tumour cells from time-lapse image sequences. In Alpesh Ranchordas and Helder Arajo, editors, *VISAPP 2009 - Proceedings of the Fourth International Conference on Computer Vision Theory and Applications, Lisboa, Portugal, February 5-8, 2009 - Volume 1*, pages 281–286. INSTICC Press, 2009a. ISBN 978-989-8111-69-2.

K. Yan, F. J. Verbeek, S. E. Le Dévédec, and B. van de Water. Cell tracking and data analysis of in vitro tumour cells from time-lapse image sequences. pages 281–286, 2009b.

A. G. Youness and A. M. Hamid. Adaptive linear discriminant analysis for online feature extraction. *Machine Vision and Applications*, 24(4):777–794, 2013. ISSN 0932-8092. doi: 10.1007/s00138-012-0439-z. URL http://dx.doi.org/10.1007/s00138-012-0439-z.

C. Zhang and T. H. Chen. Efficient feature extraction for 2d/3d objects in mesh representation. In *in Mesh Representation, ICIP 2001*, volume 3, pages 935–938, 2001.

G. P. Zhang. Neural networks for classification: a survey. *IEEE Transactions on Systems, Man and Cybernetics, Part C (Applications and Reviews)*, 30(4):451–462, November 2000. ISSN 10946977. doi: 10.1109/5326.897072.

Y. Zhang, Y. Sun, and J. R. Cole. A sensitive and accurate protein domain classification tool (salt) for short reads. *Bioinformatics*, 29(17):2103–2111, 2013.

T. Zhao, J. Xie, F. Amat, N. Clack, P. Ahammad, H. C. Peng, F. H. Long, and E. Myers. Automated reconstruction of neuronal morphology based on local geometrical and global structural models. *Neuroinformatics*, 9(2-3):247–261, 2011. ISSN 1539-2791. doi: 10.1007/s12021-011-9120-3. URL http://dx.doi.org/10.1007/s12021-011-9120-3.

J. Ziegel and M. Kiderlen. Estimation of surface area and surface area measure of three-dimensional sets from digitizations. *Image Vision Comput.*, 28(1):64–77, 2010. ISSN 0262-

8856. doi: 10.1016/j.imavis.2009.04.013. URL http://dx.doi.org/10.1016/j.imavis.2009.04.013.

Summary

Bioinformatics is an interdisciplinary field in which knowledge is derived through computational analysis of biological data. These biological data is acquired from a range of sources, such as genetic data, patient statistics and scientific literature. The goal of the research presented in this thesis is to develop methods for the analysis of microscopy images and extract useful knowledge from these images for biology. This thesis particularly focuses on the analysis of differences in the phenotype of biological specimens visualized in both 2D and 3D images and captured with different microscopes. Our results intend to support biology in analysing pathways and to generate a better representation of biological models for such phenotype analysis.

Chapter 2 focuses on the understanding of pathway development of epidermal growth factor receptor (EGFR) endocytosis. A model representation is provided so that a solution can be elaborated analysing the high-content cytomics screening for target discovery. The system can automatically extract the interesting objects (proteins) for the phenotype measurement and use pattern recognition methods to characterize the objects into characteristic developmental episodes of EGFR endocytosis.

Chapter 3 further elaborates on EGFR endocytosis research. In order to improve the phenotype identification process we devised and applied a hierarchical classification strategy. In addition, we introduced the wavelet-based texture measurements to generate extra prominent features for the classification. With these two refinements, the phenotype identification process significantly improved and can be employed for the discovery of regulators of the EGFR endocytosis process. In support of advanced representation of models that are derived from 3D images,

in Chapter 4 we introduce an analytical evaluation for the point based 3D surface reconstruction methods. In our study we used three analytical shapes, i.e. the sphere, the ellipsoid and the oval, so that a ground truth measurement is available. We studied these three shapes with the same volume size under different levels of noise and we evaluated three major surface descriptors: surface area, surface distance and curvature. The results revealed that within from the point cloud reconstruction methods, the Poisson reconstruction method performs best in surface preservation and noise suppression.

In Chapter 5 we have used the conclusions of Chapter 4 and further extend a system for 3D model representation and analysis from a stack of images. We developed a contour interpolation strategy to convert a 3D contour model to a uniformly distributed 3D point cloud. With this point cloud, subsequently, the Poisson reconstruction method is used to reconstruct an accurate surface model. Our representation is tested with two typical 3D models; in a study of zebrafish development using the proper 3D shape descriptors we have verified that the preprocessing and 3D representation works.

In Chapter 6 we have used more complex 3D models to investigate if these can be successfully analysed. The mammary gland in new-born mouse is a branched structure and this requires different strategies for analysis. Therefore we have employed centerline of the optimized 3D model in order to extract a good representation of the topological information. Features from the topology are used to analyse 3D models from mammary glands that developed under exposure of different potential endocrine disruptors. We presented that we are able to differentiate the different conditions and characterize the effect of the exposures. In addition, we modelled the branched structure using an L-system so as to obtain further evidence of the correct characterization of the different conditions using our measurement system.

In our studies, we have intended to find multiple ways to deal with image datasets in both 2D and 3D space. These image datasets are from high-throughput screening or from image stacks. All of the datasets have a relatively large volume. How to extract meaningful and crucial information from large quantities of biological images has been the major question that we intended to address. We have applied different methods for the extraction of objects of interest from the im-

ages; we have used different shape descriptors to analyze the objects and we have utilized a range of pattern recognition strategies to categorize patterns that we suspected in the data. We have used these techniques in support of the further understanding of biology, i.e. pathways and development. Our work contributes to the field of bioinformatics, has shown to be meaningful and will show to be sustainable.

Samenvatting

Bioinformatica is een interdisciplinair onderzoeksveld dat zich richt op het afleiden van kennis door computationele analyse van data verkregen experimenten uit de levenswetenschappen. Deze biologische data kunnen komen van een reeks van verschillende bronnen, zoals bijvoorbeeld genetische sequenties, statistische patient gegevens en wetenschappelijke literatuur. Het doel van het onderzoek dat wordt beschreven in dit proefschrift is om methoden te ontwikkelen voor de analyse van microscoopbeelden en het verkrijgen van, voor de biologie, bruikbare kennis uit deze analyses. Dit proefschrift richt zich in het bijzonder op de analyse van verschillen in phenotype binnen biologische experimenten zoals deze worden gevisualiseerd in zowel 2D als 3D beelden die zijn verkregen met verschillende microscopen. Onze resultaten beogen biologie te ondersteunen met het analyseren van pathways and het maken van betere representaties van biologische modellen voor het analyseren van phenotypes.

In Hoofdstuk 2 van dit proefschrift ligt de nadruk op het begrijpen van pathways voor de rol van de Epidermale Groei Factor Receptor (EGFR) in het proces van endocytose. Een model representatie is gemaakt waarmee een oplossing kan worden uitgewerkt voor de analyse van high-content cytomics screens waardoor nieuwe componenten kunnen worden gedentificeerd voor het ontwikkelen van therapie tegen kankercellen. Het meetsysteem kan automatisch de objecten (eiwitten) herkennen en deze karakteriseren in de verschillende ontwikkelingsfasen van EGFR endocytose.

In Hoofdstuk 3 wordt het onderzoek het meten van EGFR endocytose verder uitgewerkt. Teneinde de het identificeren van het phenotype verder te verbeteren hebben we een hierarchische classificatie strategy ontworpen en gemplementeerd.

Daarenboven, hebben we z.g. wavelet textuur metingen gentroduceerd zodat we nog betere kenmerken hebben voor de classificatie in de model representatie van karakteristieke episodes. Deze twee toevoeginen leveren een significate verbetering aan het meetsysteem en kunnen worden gebruikt voor de ontdekking van regulatoire componenten in het proces van EGFR endocytose.
Voor geavanceerde representatie van modellen die worden verkregen uit 3D beelden introduceren we in Hoofdstuk 4 we een analytische evaluatie voor de reconstructie van een 3D oppervlak uit 3D puntenwolken. In onze studie maken we gebruik van drie vormen waarvan ook een pure analytische beschrijving beschikbaar is, i.e. de bol, de ellipsoide en de ovoide, waardoor een goede referentie waarde ten opzichte van onze meting beschikbaar is. We hebben deze drie vormen in dezelfde volumegrootte maar door toevoeging van verschillende ruis-niveaus, bestudeerd en daarbij gevalueerd met veschillende kenmerkende maten zoals oppervlak, afstand tot oppervlak en curvatuur. De resultaten laten zien dat uit de verschillende methoden voor 3D reconstructie uit puntenworken, de Poisson reconstructie methode het best presteert in termen van oppervlakte-integriteit en het gevoeligeid vooor ruis.
In Hoofdstuk 5 hebben we de conclusies uit Hoofdstuk 4 gebruikt om een systeem voor het representeren van 3D modellen en analyse uit 3D beelden verder uit te breiden. We hebben een strategie ontwikkeld om contouren te interpoleren om zo uit een 3D contour model een uniform gedistribueerde 3D puntenwolk te converteren. Op deze puntenwolk wordt vervolgens de 3D Poisson reconstructie methode toegepast om zo een accuraat 3D oppervlakte model te genereren. Onze representatie is getest me twee typische toepassingen in 3D modelleren; voor een studie in zebravis ontwikkeling met de juiste vormbeschrijving hebben we kunnen verifiren dat het systeem representatie optimalisatie en meting goed werkt.
In Hoofdstuk 6 maken we gebruik van complexere modellen om te onderzoeken of ook dergelijke modellen met ons systeem (uit hoofdstuk 4&5) succesvol kunnen worden geanalyseerd. De borstklier van de pas-geboren muis is een vertakte structuur en dit vereist een speciale aanpak voor analyse. We hebben daartoe gebruik gemaakt van de middellijn van deze 3D structuur om een goede representatie van de topologische informatie te kunnen verkrijgen. Kenmerken van de topologie worden gebruikt om 3D modellen van de borstklier te analyseren die in de ontwikkeling zijn blootgesteld aan verschillende potentieele endocriene

verstorings-stoffen. We laten zien dat we in staat zijn de verschillende condities te onderscheiden in onze metingen en het effect van de blootstelling te karakteriseren. Daarnaast hebben we het systeem van de vertakkende structuur gemodelleerd met een zg. L-systeem teneinde verder bevestiging te krijgen van de correcte karakterisering van de verschillende condities door ons meetsysteem.
In onze studies, hebben we de intentie gehad verschillende manieren te vinden om sets van beelden zowel 2D als 3D onder handen te kunnen nemen. Deze sets van beelden zijn relatief groot van omvang. De centrale vraag was daarin hoe betekenisvolle en cruciale informatie uit deze grote hoeveelheden data gehaald kunnen worden. We hebben gebruik gemaakt van een scala van matematische vormbeschrijvingen om de beelden te analyseren en diverse patroonherkenningstechnieken om patronen die we vermoeden in de data te catagoriseren. Deze technieken hebben we gebruikt om dieper begrip in de biologie te kunnen ondersteunen, i.e. pathways en ontwikkeling. Ons werk draagt daarbij bij aan het onderzoeksveld van de bioinformatica, het heeft zijn nut reeds bewezen en zal dat blijven doen in de toekomst.

List of Publications

L. Cao, K. Yan, L. Winkel, M. de Graauw, F.J. Verbeek. Pattern Recognition in High-Content Cytomics Screens for Target Discovery: Case Studies in Endocytosis. Proceedings of Pattern Recognition in Bioinformatics 2011, Delft, LNCS Springer, pages 330-342, 2011

L. Cao, K. Yan, L. Winkel, M. de Graauw, F.J. Verbeek. Hierarchical classification strategy for Phenotype extraction from epidermal growth factor receptor endocytosis screen. Journal of BMC bioinformatics, 2013 (Submitted)

M. de Graauw, L. Cao, L Winkel, M.H. van Miltenburg, S.E. Le Dévédec, M. Klop, K. Yan, C. Pont, V.M. Rogkoti, A. Tijsma, A. Chaudhuri, R. Lalai, L. Price, F.J. Verbeek, B. van de Water. Annexin A2 depletion delays EGFR endocytic trafficking via cofilin activation and enhances EGFR signaling and metastasis formation. Oncogene. doi:10.1038/onc.2013.219. 2013

L. Cao, F.J. Verbeek. Evaluation of algorithms for point cloud surface reconstruction through the analysis of shape parameters. 3D Image Processing (3DIP) and Applications 2012, Proceedings SPIE Vol. 8290,Bellingham, 82900G, 2012

L. Cao, F.J. Verbeek. Analytical evaluation of algorithms for point cloud surface reconstruction using shape features. Journal of Electronic Imaging, 22(4), 043008, doi:10.1117/1.JEI.22.4.043008, 2013

L. Cao, F.J. Verbeek. Nature inspired phenotype analysis with 3D model

representation optimization. Proceedings of the 4th International Conference on Innovations in Bio-Inspired Computing and Applications,IBICA 2013, Ostrava, 2013

E. Larios, Y. Zhang, L. Cao, and F. J. Verbeek. CytomicsDB: A Metadata-based storage and retrieval approach for High-Throughput Screening Experiments, The 9th IAPR conference on Pattern Recognition in Bioinformatics, 2014.

Curriculum Vitae

Lu Cao was born on December 19th, 1983 in Ningbo, Zhejiang Province, China. She received her bachelor degree of Computer Science and Technology at Beijing Forestry University in 2006. In the same year, she got the test waiver admission of Graduate school at the same university and received her master degree of Computer Application Technology in 2009. She gained the scholarship from China Scholarship Council and was accepted as a PhD student supervised by Fons J. Verbeek in Imaging and Bioinformatics section, Leiden institute of Advanced Computer Science, Leiden University. Her research focuses on image analysis, pattern recognition, 3D model representation and analysis. Now, she is working in Robert Passier's group in the faculty of anatomy and embryology, LUMC as a postdoc.